INFORMATION TO USERS

This manuscript has been reproduced from the microfilm master. UMI films the text directly from the original or copy submitted. Thus, some thesis and dissertation copies are in typewriter face, while others may be from any type of computer printer.

The quality of this reproduction is dependent upon the quality of the copy submitted. Broken or indistinct print, colored or poor quality illustrations and photographs, print bleedthrough, substandard margins, and improper alignment can adversely affect reproduction.

In the unlikely event that the author did not send UMI a complete manuscript and there are missing pages, these will be noted. Also, if unauthorized copyright material had to be removed, a note will indicate the deletion.

Oversize materials (e.g., maps, drawings, charts) are reproduced by sectioning the original, beginning at the upper left-hand corner and continuing from left to right in equal sections with small overlaps.

Photographs included in the original manuscript have been reproduced xerographically in this copy. Higher quality 6" x 9" black and white photographic prints are available for any photographs or illustrations appearing in this copy for an additional charge. Contact UMI directly to order.

ProQuest Information and Learning
300 North Zeeb Road, Ann Arbor, MI 48106-1346 USA
800-521-0600

UMI®

Active tectonics in the central Tien Shan, Kyrgyz Republic

Stephen C. Thompson

A dissertation submitted in partial fulfillment of the
requirements for the degree of

Doctor of Philosophy

University of Washington

2001

Department of Earth and Space Sciences

UMI Number: 3014037

Copyright 2001 by
Thompson, Stephen C.

All rights reserved.

UMI®

UMI Microform 3014037
Copyright 2001 by Bell & Howell Information and Learning Company.
All rights reserved. This microform edition is protected against
unauthorized copying under Title 17, United States Code.

Bell & Howell Information and Learning Company
300 North Zeeb Road
P.O. Box 1346
Ann Arbor, MI 48106-1346

©-Copyright 2001

Step•hen C. Thompson

In presenting this dissertation in partial fulfillment of the requirements for the Doctoral degree at the University of Washington, I agree that the Library shall make its copies freely available for inspection. I further agree that extensive copying of the dissertation is allowable only for scholarly purposes, consistent with "fair use" as prescribed in the U.S. Copyright Law. Requests for copying or reproduction of this dissertation may be referred to Bell and Howell Information and Learning, 300 North Zeeb Road, Ann Arbor, MI 48106-1346, to whom the author has granted "the right to reproduce and sell (a) copies of the manuscript in microform and/or (b) printed copies of the manuscript made from microform."

Signature _____

Date June 8, 2001

University of Washington
Graduate School

This is to certify that I have examined this copy of a doctoral dissertation by

Stephen C. Thompson

and have found that it is complete and satisfactory in all respects,
and that any and all revisions required by the final
examining committee have been made.

Chair of Supervisory Committee:

Alan R. Gillespie

Reading Committee:

Alan R. Gillespie

Charles M. Rubin

Darrel S. Cowan

Brian F. Atwater

Date: June 8, 2001

University of Washington

Abstract

Active tectonics in the central Tien Shan, Kyrgyz Republic

Stephen C. Thompson

Chair of the Supervisory Committee:
Professor Alan R. Gillespie
Department of Earth and Space Sciences

Fault slip rates show that late Quaternary contraction is distributed across the Kyrgyz central Tien Shan, and not concentrated at its margins. Nearly every intermontane basin contains Neogene and Quaternary syntectonic strata deformed by Holocene north-south shortening on thrust and reverse faults. In a region that spans almost two-thirds of the north-south width of the central Tien Shan, slip rates on eight faults in five basins range from ~0.1 to ~3 mm/yr. Fault slip rates come from faulted and folded river terraces and from trench-wall exposures. Radiocarbon, infrared-stimulated luminescence, and thermoluminescence ages limit ages of terraces and aid in their regional correlation. A major episode of regional river incision occurred ~13.5–15.7 x 10^3 cal yr B.P., coincident with abrupt warming of global climate at the end of the last glacial period. The penultimate major river incision occurred ~141 ka, coincident with the end of the penultimate glacial period. The sum of late Quaternary rates of shortening resembles current rates of north-south shortening measured using Global Positioning System (GPS) geodesy since 1992. This similarity suggests that deformation is concentrated along major fault zones near range-basin margins. Such faults, separated by essentially rigid blocks, accommodate most of the shortening in the upper crust.

Paleoseismic data from offset river terraces and trench exposures of faults in the northern foreland and intermontane basins provide evidence ~2–4 m of displacement during earthquakes, and include a ~3.5 m displacement from the 1885 $M \approx 6.9$ Byelovoda earthquake. The range of displacement is similar to the observed surface displacement after the 1992 $M_s = 7.3$ Suusamyr earthquake. A preliminary source map of high slip-rate faults across the Kyrgyz central Tien Shan indicates that a 2–4 m event should occur every ~60–70 years. This result is generally consistent with the historical record.

Table of Contents

Page

List of Figures iv
List of Tables vii

Chapter 1: Introduction 1
1.1 Motivation 2
1.2 Tectonic and geologic setting 4
1.3 Distribution and character of late Quaternary faulting and folding 5

Chapter 2: Stratigraphy of late Quaternary river terraces 9
2.1 Lithostratigraphy 10
2.2 Regional sequence of terraces 11
2.3 Chronology 13
2.3.1 Radiocarbon ages 13
2.3.2 Luminescence ages, QII(2) terrace 15
2.4 Inferred process of terrace formation 16

Chapter 3: Methods for calculating slip rate 31
3.1 Collection of field data 32
3.2 Slip rate calculation for an offset river terrace 32
3.3 Measuring slip rate with fault-bend folding of terraces 34
3.4 Representation and calculation of uncertainties 37

Chapter 4: Late Quaternary slip rates 47
4.1 Issyk-Ata fault, Chu basin 47
4.1.1 Alamedin River site 47
4.1.2 Sokuluk River site 50
4.2 Akchop Hills and South Kochkor faults, Kochkor Basin 51
4.2.1 Akchop Hills fault 52

4.2.2 South Kochkor fault 53
4.3 Kadjerty and Central Naryn faults, Naryn basin 54
4.3.1 Kadjerty fault, Kadjerty River site 54
4.3.2 Kadjerty fault, Kurtka River site 55
4.3.3 Central Naryn fault 57
4.4 Oinak-Djar fault, At-Bashi basin 57
4.5 North and South Kyrkungey faults, Aksay basin 58
4.5.1 North Kyrkungey fault 59
4.5.2 South Kyrkungey fault 59
4.6 Summary of slip rates 60

Chapter 5: Converting slip rates to geologic shortening rates 81
5.1 Fault geometry in the upper crust of the Tien Shan 81
5.2 Method to convert slip rate to north-south shortening rate 82
5.3 Results of the shortening rate comparison 84

Chapter 6: Paleoseismic evidence for average displacement and recurrence interval of large earthquakes in the central Tien Shan 89
6.1 Introduction 89
6.2 Sokuluk fan trench site, Chu basin 90
6.2.1 Topographic profiles 90
6.2.2 Trench structure and stratigraphy 91
6.2.3 Age control 93
6.2.4 Evidence for earthquakes 94
6.2.5 Summary 95
6.3 Oinak-Djar fault, At-Bashi basin 96
6.3.1 Trench stratigraphy and radiocarbon dating 96
6.3.2 Trench structure 97
6.3.3 Evidence for earthquakes 98
6.3.4 Summary 100
6.4 Kadjerty River, Naryn basin 101

6.5 Summary of average displacement, recurrence interval, and magnitude for large earthquakes 103
6.5.1 Comparison with historical events 103
6.5.2 Estimated magnitudes of paleo-earthquakes 104
6.6 Recurrence interval of M ~6.9–7.4 earthquakes in the Central Tien Shan 105

Chapter 7: Discussion and Conclusions 122
7.1 Kinematics 122
7.1.1 Style, distribution, and geometry of active faulting 122
7.1.2 Strain partitioning in the upper crust 124
7.1.3 Coseismic deformation 125
7.2 Dynamics 126
7.2.2 Horizontal forces at the margins 126
7.2.1 Basal traction 127
7.3 Concluding remarks 127

References 128

List of Figures

Page

1.1 Map of the Tien Shan 6

1.2 Landsat mosaic of the central Tien Shan 7

1.3 Fault map of the central Tien Shan 8

2.1 Drainage network of the Kyrgyz central Tien Shan 23

2.2 Terrace stratigraphy 24, 25

2.3 Radiocarbon age calibrations for the QIII(2) terrace 26

2.4 Detrital charcoal sample locations, Kadjerty River 27

2.5 Photomosaic of the Kadjerty River QIII(2) terrace 28

2.6 Luminescence dating results 29

2.7 Formation of river terraces 30

3.1 Analysis of a faulted river terrace 41

3.2 Dip-slip calculation for a faulted river terrace 42

3.3 Deformation of unconformities in response to idealized fault-bend folding 43

3.4 Schematic illustration of fault-bend folding 44

3.5 Deformation of unconformities with a curved fault bend 45

3.6 Calculation of slip-rate uncertainties using a Monte-Carlo simulation 46

4.1 Maps of the Issyk-Ata fault, Chu basin 62

4.2 Photos of the Alamedin River terraces 63

4.3 Slip-rate evaluation of the Issyk-Ata fault at the Alamedin River 64

4.4 Profile of the QIII(2) fan across the Issyk-Ata fault near the Sokuluk River 65

4.5 Maps showing active deformation in the southern Kochkor basin 66

4.6 Nested river terraces along the west side of the Djuanarik River 67

4.7 Slip-rate determination of the Akchop Hills fault 68

4.8 Slip rate of the South Kochkor fault 69

4.9 Maps of the northern Naryn basin 70, 71

4.10 Kadjerty fault in the Kadjerty River valley 72

4.11 Kadjerty fault in the Kurtka River valley 73

4.12 Central Naryn fault near the Kadjerty River 74

4.13 Map and photo of the Oinak-Djar fault 75

4.14 Slip rate of the Oinak-Djar fault 76

4.15 Map of the eastern Aksay basin 77

4.16 Slip rate of the North Kyrkungey fault 78

4.17 Slip rate of the South Kyrkungey fault 79

4.18 Map of recently active faults and fault slip rates 80

5.1 Geologic cross-section of the southern Kochkor basin 86

5.2 Conversion from fault dip slip to horizontal shortening 87

5.3 Comparison of geologic and geodetic shortening rates 88

6.1 Major historic earthquakes in the Tien Shan 110

6.2 Topographic map along the Issyk-Ata fault near the Sokuluk River trench 111

6.3 Profiles and photo of terraces within the ephemeral drainage 112

6.4 Trench and soil-pit logs 113

6.5 Restorations of the Sokuluk site trench 114

6.6 Photos of the Oinak-Djar fault trench 115

6.7 Log of the Oinak-Djar fault trench 116

6.8 Detailed log of the west trench wall, showing fault displacements 117

6.9 Restorations of the Oinak-Djar trench 118

6.10 Air photo and map of the Kadjerty River terraces near the Kadjerty fault 119

6.11 Nested terraces progressively offset by the Kadjerty fault 120

6.12 Preliminary source map for Holocene faults in the study area 121

List of Tables

Page

2.1 Radiocarbon ages of river terraces 20, 21

2.2 Thermoluminescence and infrared-stimulated luminescence ages 22

5.1 Parameters used to calculate geologic shortening rates and results 85

6.1 Radiocarbon ages of paleoseismic trench samples 107, 108

6.2 Infrared-stimulated luminescence data for the QIII(2) Sokuluk River fan 109

Acknowledgements

This work was supported by NSF research grant EAR 96-14412 to Charles Rubin, and by student grants from the Geological Society of America, American Association of Petroleum Geologists, and the University of Washington Department of Geological Sciences. A Peter Misch Fellowship, Harry Wheeler Scholarship, and David Johnston Fellowship from the UW Department of Geological Sciences provided meaningful financial support.

Many contributed to the effort presented in this thesis. First and foremost I thank Alan Gillespie and the gang at the W.M. Keck Remote Sensing Laboratory for sharing a productive and friendly work environment. Alan has provided endless advice, encouragement, and support. Aside from Alan, I have benefited from interactions with many Geological Sciences and Geophysics faculty and graduate students. There are too many to list individually.

Most collaboration in this project has been with people outside the UW. Charlie Rubin provided this outstanding research opportunity for me; for his support and collegiality I am grateful. I appreciate time spent with him, Meghan Miller, and other faculty and students at Central Washington University. Ray Weldon has been an insightful, creative, and energetic colleague. Peter Molnar shared his insight, (almost) endless patience, and encouragement. Kanatbek Abdrakhmatov has been a perceptive and capable colleague; much of his previous work on identifying active faults and river terraces built the foundation for this study.

Many additional colleagues have aided and inspired my research. Tien Shan project members include: K. Abdrakhmatov, B. Belinsky, D. Burbank, M. Bullen, B. Hager, T. Herring, B. Meade, M. Miller, P. Molnar, S. Park, G. Pavlis, S. Roecker, C. Rubin, F. Vernon, and R. Weldon. I have benefited from exchanges with the project members during several Tien Shan working group meetings over the past four years. T. Herring and B. Hager provided GPS velocities prior to publication. J. Southon and Brian at CAMS were generous with time and energy during my visits to Lawrence Livermore National Labs to prepare radiocarbon samples. G. Berger at DRI shared insights with luminescence dating. J. Hinthorne and his students at CWU ran XRD analyses of snail shells and silt. S. Boyer helped with early attempts at cross-section balancing. There were many others.

The time spent in the Kyrgyz Republic was memorable. Kanatbek Abdrakhmatov provided many great camping spots and much appreciated humor, philosophy, and patience. Atyr Abdrakhmatov nourished us with excellent food and tolerated a group of particular Americans. The scientific station IVTAN, under the leadership of G. Schletchkov and the late Yu. A. Trapeznikov, provided excellent logistical support. I appreciated conversations and time in the field with I. Sadybakasov, A. Mikolaichuk, A. Korjenkov, V. Sankova, O. Grigina, and the late O. Chediya. Большое спасибо. I also thank K. Armstrong, M. Bullen, D. Burbank, R. Burke, K. Fengler, A. Gillespie, M. Koppes, R. Langridge, J. Lavé, K. McLean, Meghan Miller, Martin Miller, E. Sobel, C. Tozer, K. Weberling, and C. Whitehill for help in the field and for sharing an enjoyable camp.

Finally, I thank my family in Seattle for taking care of me: Keira, Jan, and Dave.

Dedication

To Keira. Я Ты Люблю.

And to my parents, for their love and encouragement.

Chapter 1

Introduction

This thesis describes late Quaternary deformation across the Tien Shan, a mountain belt in central Asia (Figure 1.1). The research, funded by the Continental Dynamics program at the National Science Foundation, is part of a multidisciplinary project that uses the central Tien Shan to learn about intracontinental deformation (Hager et al., 1996). The geological component of the project focuses on the late Cenozoic kinematics of the central portion of the belt (Figure 1.2): when and where deformation initiated, how the deformation progressed through time, how much shortening has occurred, and how geologic shortening was distributed in the late Quaternary. My thesis addresses the last question.

A major goal is to provide a snapshot in geologic time of how strain rates are partitioned across the belt. This snapshot, which spans several earthquake cycles, consists of late Quaternary slip rates on the most active faults. I estimate late Quaternary slip rates across the northern two-thirds of the central Tien Shan, within the Kyrgyz Republic (Figures 1.2 and 1.3).

A secondary focus is the paleoseismic behavior of the faults. I estimate the displacement, recurrence, and magnitude of prehistoric ground-rupturing events from three sites. The paleoseismic data provide a link between the geologic slip rates, which measure displacement over several earthquake cycles, and geodetic rates of shortening, which have measured interseismic strain since 1992 (Abdrakhmatov et al., 1996).

Together, the slip-rate and paleoseismic data provide a description of how strain is partitioned across the belt. The distribution and partitioning of strain across active faults provide a test for simulations of intra-plate mountain building as well as fundamental data for seismic hazard evaluation in the central Tien Shan.

The study of active tectonics in this thesis covers a north-south transect through the northern two-thirds of the central Tien Shan, within the borders of the Kyrgyz Republic (Figure 1.3). The

field data presented here were collected over three summers—1997, 1998, and 1999—and involved numerous collaborators who are listed individually in the Acknowledgments. Many project members shared in the collection of field data on every aspect of the geologic research. For this reason I commonly use the first person plural where referring to the collection of field data.

Because river terraces provide the best markers of late Quaternary deformation in the intermontane basins of the Tien Shan, and their ages allow deformation rates to be quantified, Chapter 2 focuses on the terrace stratigraphy in the central Tien Shan. The chapter presents the existing stratigraphic system used to correlate terraces, the radiocarbon and luminescence results that limit the timing of formation of prominent river terraces, and the inferred process of terrace formation. Chapter 3 presents methods used to measure and quantify uncertainties in slip rates. These include Monte Carlo simulations of uncertainties to allow each input variable to have a range of normal and discrete probability distributions. Chapter 4 presents evidence for late Quaternary slip rates, and Chapter 5 compares geologic slip rates with present-day geodetic shortening rates inferred from global positioning system (GPS) geodesy. In this preliminary comparison I rely on geometric conversion of slip rates to obtain geologic shortening rates. Chapter 6 presents paleoseismic evidence from three sites for the displacement and recurrence of large earthquakes. The data are combined with the results of Chapter 4 to estimate the recurrence rate of large earthquakes in the central Tien Shan. Chapter 7 provides a brief summary discussion and conclusions.

The rest of this first chapter lays out my reasons for examining geologic slip rates in the central Kyrgyz Tien Shan, and describes the tectonic setting of the belt.

1.1 Motivation

How is strain partitioned during the growth of mountain belts? Many convergent belts, particularly in plate boundary settings, have a dominant vergence and also show a unidirectional propagation of major faults (Dahlstrom, 1970; Le Fort, 1975; Mattauer, 1975; Royse et al., 1975; Bally et al., 1986; Butler, 1986). These characteristics are generally associated with simple shear on a gently dipping fault that underlies the belt (Cook et al., 1979; Mugnier et al., 1990; Nelson

and others, 1996). At first, the shortening rate across these thrust belts was believed to be localized at the frontal fault (Dahlstrom, 1970; Boyer and Elliott, 1982), and field studies show that this condition does exist in nature, at least at one prominent belt (Lavé and Avouac, 2000). Geologic (Boyer, 1992), analog (Koyi et al., 2000), and numerical (Davis et al., 1983; Dahlen, 1984; Willett, 1999) studies, however, show that strain rates not only can be concentrated at a frontal fault, but also can be distributed across the entire deforming orogen.

Other convergent mountain belts have formed far from plate boundaries. Many of these—commonly called "thick-skinned" belts—lack a dominant direction of vergence, tend to contain widely spaced, fault-bounded ranges and basins, and lack clear association with an underlying low-angle fault (Molnar and Tapponnier, 1975; Tapponnier and Molnar, 1979; Gries, 1983; Jordan and Allmendinger, 1986; Rodgers, 1987). Although Earth scientists have long recognized differences among convergent mountain belts, inferences about the partitioning of strain rate across thick-skinned belts have been based on geological and geophysical observations with mostly qualitative results. This thesis offers a quantitative measure of the partitioning of strain across one of the most active thick-skinned mountain belts on Earth.

The Tien Shan of central Asia, a product of continuing India-Eurasia plate convergence, exemplifies late Cenozoic mountain building by distributed deformation (Schulz, 1948; Sadybakasov, 1972; Makarov, 1977; Tapponnier and Molnar, 1979; Sadybakasov, 1990; Cobbold et al., 1994; Burbank et al., 1999) (Figure 1.1). Most investigations of active tectonics in the Tien Shan thus far have focused on the timing and rates of slip on thrust fault systems that bound the northern and southern margins (Avouac et al., 1993; Brown et al., 1998; Yin et al., 1998; Burchfiel et al., 1999). This thesis examines the partitioning of late Quaternary slip rates between the northern margin and the interior of the belt, using river terraces and alluvial fans as strain markers. Some of the motivating questions include: Do faults at the margins of the mountain belt accommodate more strain rate than do faults of the interior? In comparisons between geologic and geodetic rates of deformation, does slip on major faults account for all or most of the total strain-rate field?

1.2 Tectonic and geologic setting

The central and eastern Tien Shan forms an elongate deforming region between two generally stable crustal elements: the Kazakh platform to the north and the Tarim basin to the south (Figure 1.1). Though ~1000–1500 km north of the Indo-Eurasian plate boundary, the central Tien Shan presently absorbs nearly one-half of the total relative plate convergence of ~45 mm/yr (DeMets et al., 1994; Abdrakhmatov et al., 1996; Holt et al., 2000).

The central Tien Shan displays a basin-and-range topography with late Cenozoic relief caused by distributed reverse faulting and folding (Schulz, 1948; Sadybakasov, 1972; Makarov, 1977; Tapponnier and Molnar, 1979; Chediya, 1986; Sadybakasov, 1990) (Figures 1.2 and 1.3). The generally east-west trending ranges define folded and fault-bounded blocks of previously deformed Paleozoic rocks (Burtman, 1975; Knauf, 1976). Between the blocks are basins of syntectonic Cenozoic deposits. A widespread, originally sub-planar unconformity of Mesozoic and early Cenozoic age shows >5 km of structural relief across several intermontane basin margins (Makarov, 1977; Sadybakasov, 1990; Burbank et al., 1999).

Stratigraphic studies and cooling ages have been interpreted to suggest a wide variety of ages for the initiation of late Cenozoic mountain building in the Tien Shan. Continental strata low in the Tertiary section have been interpreted to date from the Oligocene (e.g., Makarov, 1977) to middle Miocene (Gould et al., 2000; Weberling et al., 2000; Bullen et al., in press). Fission tracks in detrital apatite grains indicate cooling of source rock ~14 Ma near the southern margin of the central Tien Shan (Sobel and Dumitru, 1997), and combined fission track and U-Th-He analyses from the northern margin are consistent with rapid exhumation beginning ~11 Ma (Bullen et al., in press). In the eastern Tien Shan, exhumation (and inferred relief production) occurred in early Miocene time (~20–24 Ma), as indicated by apatite and Ar/Ar cooling ages (Hendrix et al., 1994; Sobel and Dumitru, 1997; Yin et al., 1998) and stratigraphic and structural studies (Yin et al., 1998; Burchfiel et al., 1999). Burchfiel et al. (1999) argued, however, that most of the deformation where they worked occurred in late Pliocene or Quaternary time.

Geodesy and historical seismicity provide clues about the present-day deformation field across the central Tien Shan. The north-south shortening rate measured by a GPS network, ~20

mm/yr, is evenly distributed across the central Tien Shan (Abdrakhmatov et al., 1996; Dang et al., 2001). Focal mechanisms from moderate and large earthquakes show primarily thrust and reverse faulting with P-axes close to north-south, consistent with the geodetically measured maximum shortening direction and the overall direction of Indo-Eurasian plate convergence (Shirokova, 1974; Ni, 1978; Tapponnier and Molnar, 1979; Nelson et al., 1987; Ghose et al., 1998). Historical seismic-moment release across the central Tien Shan is consistent with the rate of shortening measured by GPS, although uncertainties are large, and most of this moment was released near the margins of the belt (Molnar and Ghose, 2000).

1.3 Distribution and character of late Quaternary faulting and folding

Basins in the central Tien Shan share general similarities in active fault location, length, orientation, and sense of displacement (Figure 1.3). Holocene and late Pleistocene thrust faults commonly lie within the basin interiors, kilometers or tens of kilometers from the range-basin margins, and slip at higher rates than thrust and reverse faults that mark range-basin margins. The hanging walls of faults within the basins have deformed strata from fault-related folding and shallow flat-and-ramp-style thrust faulting (Suppe, 1983). Narrow bands of hills within the basins overlie active thrust ramps. The fault geometry implies a transfer of displacement at depth from a steep crustal ramp that underlies the basin margin to a shallow fault that extends into the basin (e.g., Ikeda, 1983). This kinematic relationship is common in the Tien Shan (Avouac et al., 1993; Molnar et al., 1994; Brown et al., 1998; Burchfiel et al., 1999) and other convergent orogens (e.g., Gries, 1983; Ikeda, 1983; Yeats and Lillie, 1991; Benedetti et al., 2000). Most Holocene and late Pleistocene fault traces are discontinuous, with alternating buried and exposed fault tip lines, and many fault lengths are shorter than the basins and ranges they occupy or bound. Most faults strike east-west to east-northeast, following the ancient structural grain of Paleozoic rocks in the ranges. Although several faults show evidence for dextral or sinistral components of motion, as revealed by fault-plane striae or laterally deflected landforms (Makarov, 1977; Cobbold et al., 1994; Abdrakhmatov et al., 2001), most of the late Quaternary faults indicate dominantly dip-slip motion. The right-lateral strike-slip Talas-Ferghana fault (Burtman, 1964; Trifonov et al., 1992; Burtman et al., 1996), west of our study area, is a notable exception.

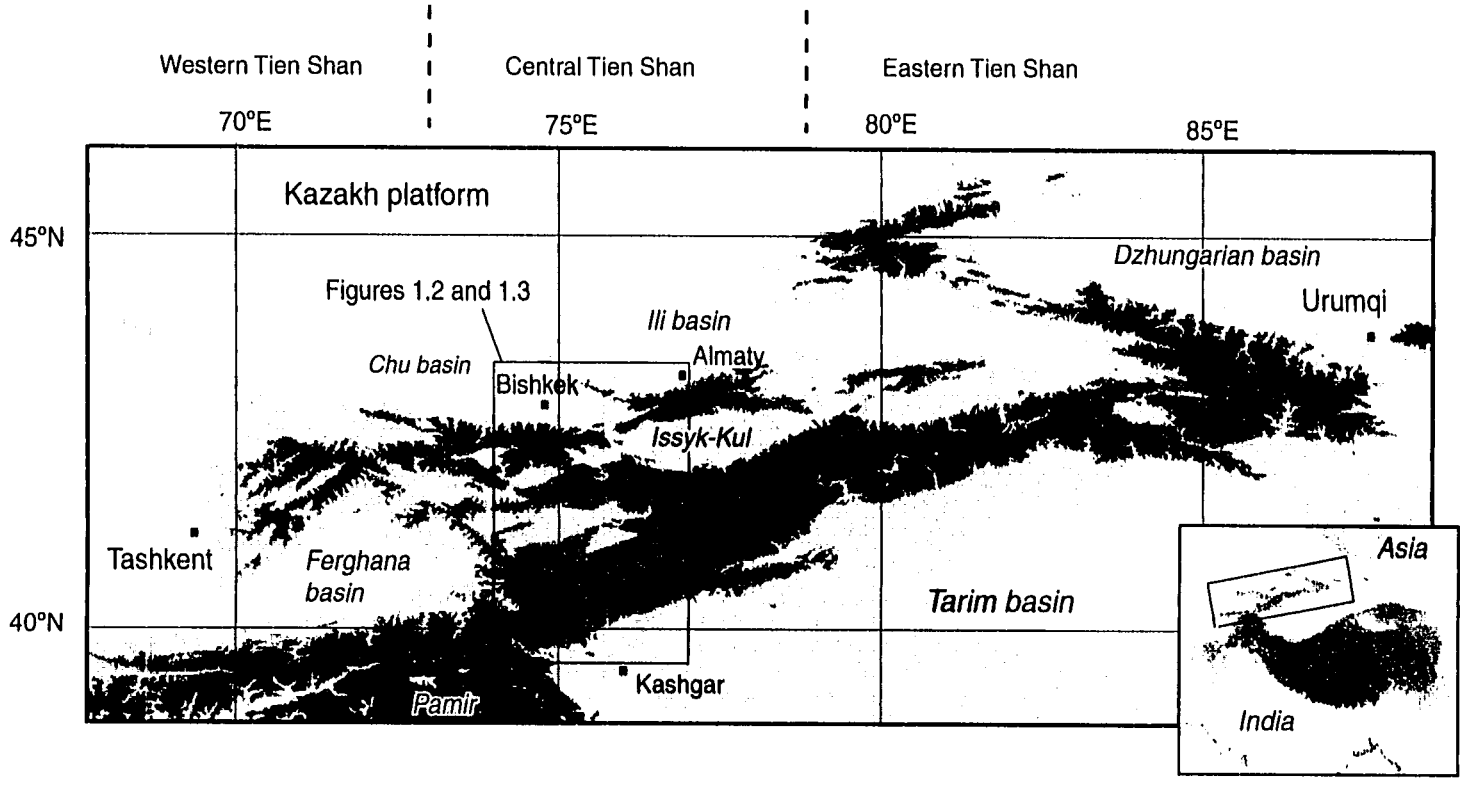

Figure 1.1: Map of the Tien Shan, with shades of grey indicating 1000, 2500, 3500, and 5500 m elevation contours. Approximate boundaries between the western, central, and eastern Tien Shan are indicated at the top of the map. Major cities and basins are labeled. Inset map shows the location of the Tien Shan in central Asia, and the box outlines the location of Figures 1.2 and 1.3.

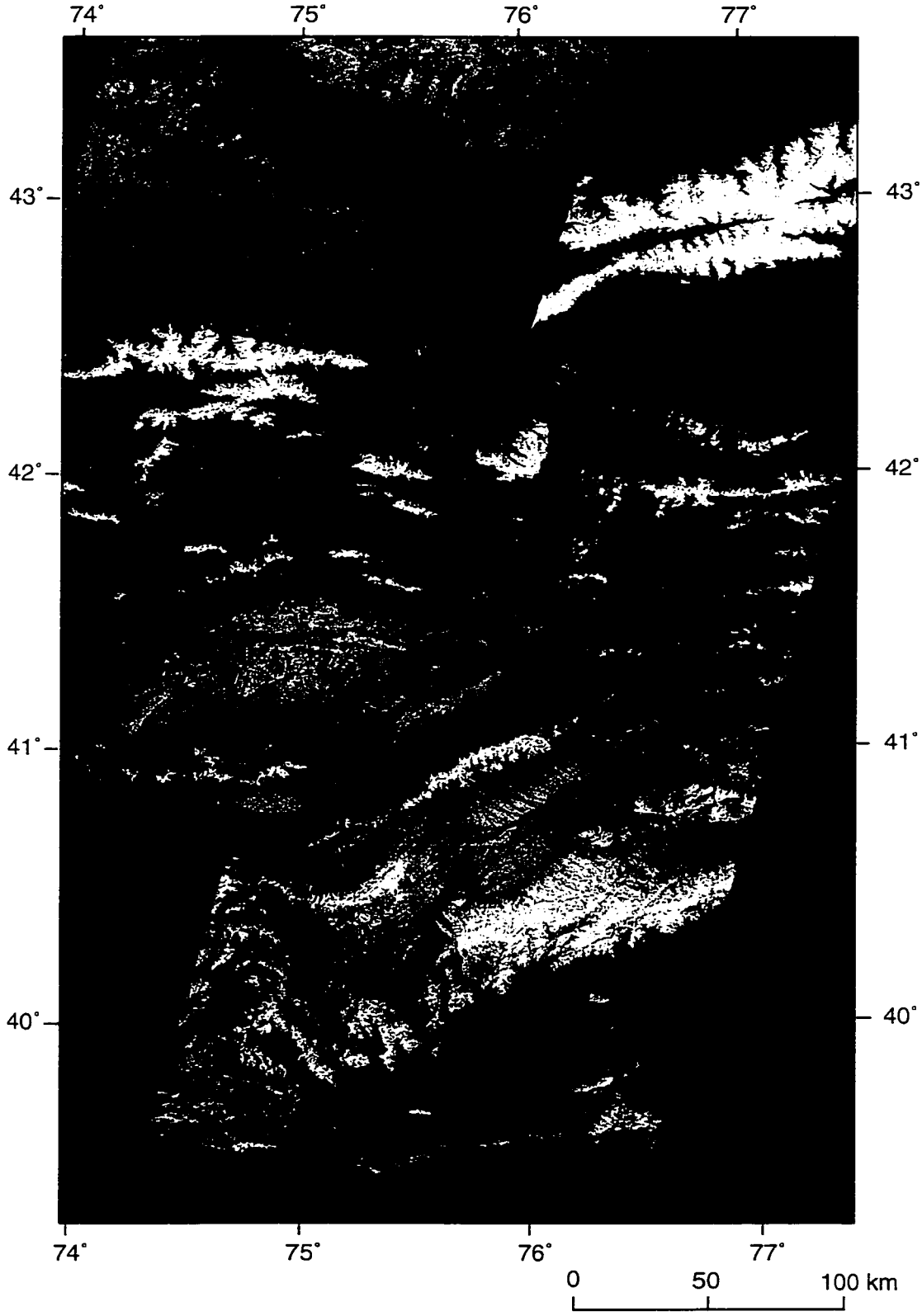

Figure 1.2: Landsat mosaic covering the central Tien Shan. Red, green, and blue are MSS bands 7, 5, and 4. Area is the same as in Figure 1.3.

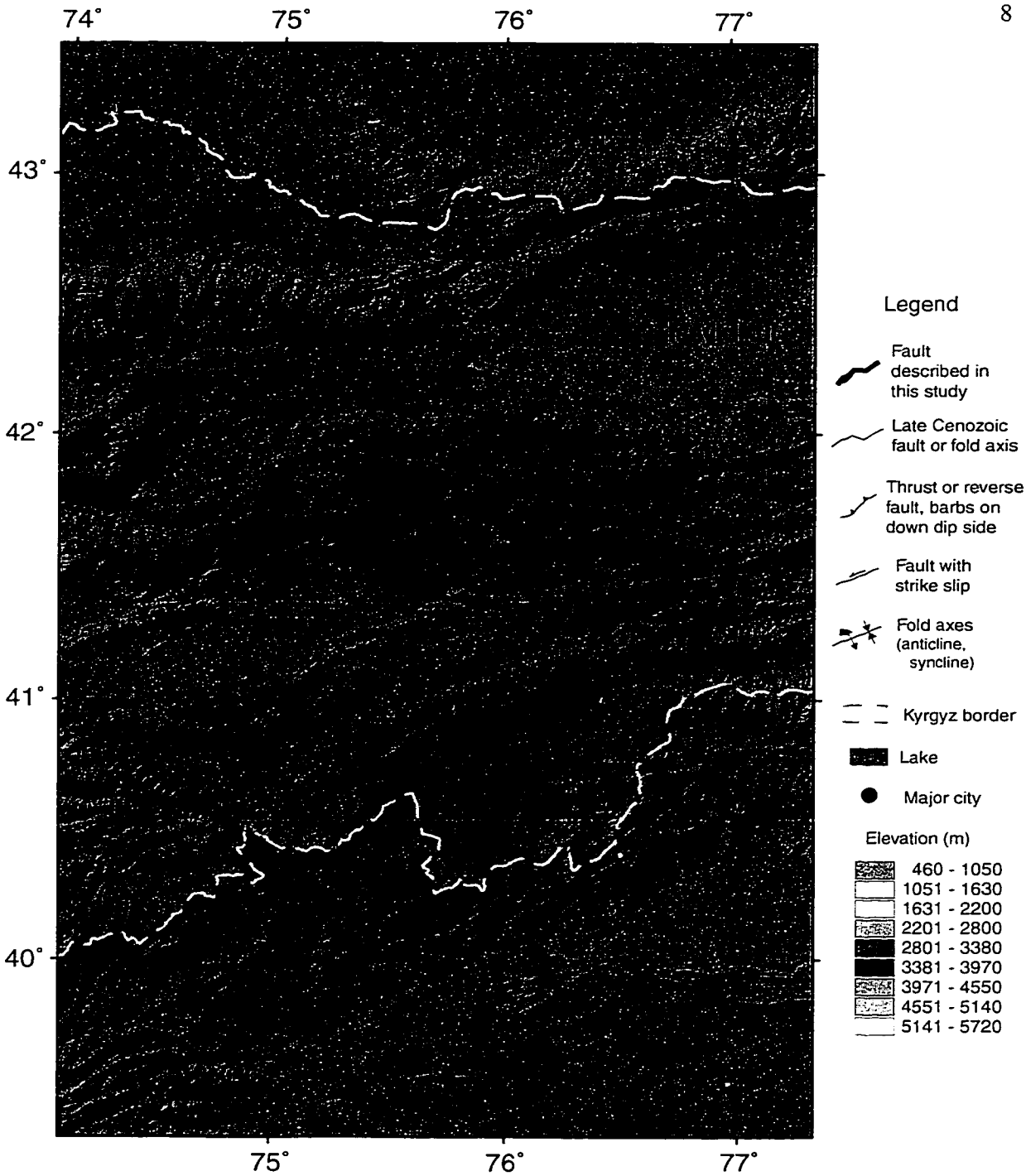

Figure 1.3: Preliminary map of active faults and folds in the central Tien Shan. Major intermontane basins and lakes, and selected ranges, are labeled. Thick lines are faults and folds for which we have determined late Quaternary slip rates. The mapped fault and fold traces are from a compilation of satellite and air photo interpretation, field observations, and unpublished data by K. Abdrakhmatov.

Chapter 2

Stratigraphy of late Quaternary river terraces

In the central Tien Shan, where crystalline ranges and sediment-filled basins strike approximately east-west, the river network comprises lower-order north- and south-flowing rivers that drain the ranges and higher-order east-west flowing rivers that drain the intermontane basins (Figure 2.1). Late Quaternary river terraces, representing ancient floodplains, occur along many of these river valleys and record the deformation of east-west trending faults and fault-related folds.

Because they have potentially datable surfaces with a readily inferred initial geometry, river terraces serve as strain markers for the study of rates and kinematics of fault deformation (Weldon and Sieh, 1985; Rockwell et al., 1988; Avouac et al., 1993; Molnar et al., 1994; Lavé and Avouac, 2000). River terraces, which represent ancient floodplains, form in response to changes in a river's sediment supply, transport capacity, or base level (Bull, 1991; Merritts et al., 1994). The lower reaches of rivers in coastal areas incise and aggrade in response to changes in sea level (e.g., Rockwell et al., 1988; Merritts et al., 1994). Rivers in continental interiors, on the other hand, lack a well known record and mechanism of base-level change. Thus, inferences about the paleohydrologic record of river aggradation and incision in continental regions may be problematic. While terrace formation is clearly related to changes in climate in many continental regions (e.g., Porter et al., 1992), precise timing of river incision and aggradation is often lacking, and is often assumed (e.g., Peltzer et al., 1989; Avouac et al., 1993).

Before terraces are used as strain markers to measure rates of tectonic deformation, it is important to test two common assumptions: that rapid river incision forms terraces, and that the river incision correlates with global climate change. For example, sediment in small river catchments draining the San Gabriel Range in southern California aggraded and incised over several thousands of years, indicating that fill terraces did not have time-synchronous surfaces (Weldon, 1986; Bull, 1991). Also, the asynchronous timing and extent of alpine glaciers

globally demonstrates that changes in global climate can result in different local manifestations and geomorphic responses (Gillespie and Molnar, 1995).

To explore the genesis of the river terraces in the intermontane Tien Shan, I discuss their stratigraphy, age, and inferred origin. Radiocarbon and luminescence ages suggest that two prominent river terrace levels formed at similar time intervals across several basins in the Kyrgyz Tien Shan. The data collected so far suggest that rivers aggraded slowly, on average, during global glacial periods, and incised rapidly during the transition between global glacial-to-interglacial periods.

2.1 Lithostratigraphy

The stratigraphic record of fluvial erosion and sedimentation on a terrace integrates past spatial and temporal variations in river sediment supply, river transport capacity, and vertical movement of the underlying bedrock. The stratigraphic elements of the terraces that lie within the Cenozoic basins of the Tien Shan consist of an eroded bedrock surface (typically carved in weakly cemented Tertiary sandstone or siltstone), a few to tens of meters of cobble to boulder gravel, and a few centimeters to several meters of silt, sand, and minor gravel. The presence, thickness, and composition of these three elements vary along and among river valleys (Figure 2.2). Thin gravel deposits commonly overlie eroded bedrock surfaces on structural highs, such as fold crests. Thick gravel commonly accumulates in structural lows, such as synclines and footwalls of faults (e.g., Molnar et al., 1994). Thus, a continuous terrace surface that crosses an active zone of faulting and folding does not conform to classic definitions of strath terraces or fill terraces, but rather varies according to local relative rates of rock uplift to gravel aggradation. The thickness and composition of the silt and sand deposits capping the terraces differ depending on distance from adjacent terrace risers or valley walls (colluvial deposition), and local history of flood overbank and loess deposition.

Reaches of modern rivers that flow through valleys with broadly preserved terraces have braided to meandering channel forms with a cobble and boulder bed. The upper reaches of most major tributary rivers lie in recently glaciated catchments or contain small cirque glaciers.

The late Quaternary stratigraphy and paleoclimate record of the Tien Shan region was developed in the major low-lying basins in Central Asia: the Chu, Ferghana, and Tajik basins (as described by K. Abdrakhmatov, personal communication, 2000, based on Grigorienko, 1961). Deposits associated with terrace fill contain pollen of grassy plants and subordinate coniferous and small-leafed trees, all suggestive of cold and dry conditions. Where pollen has been sampled between episodes of terrace aggradation (from soils or continuous depositional sequences correlated to lie between terrace fill), it contains more trees and broad-leafed plants, indicating a warmer and wetter climate (Grigina and Fortuna, 1981). The stratigraphic scheme originally developed for the low-lying basins marginal to the major mountain belts has been applied to the terrace surfaces that lie within most intermontane basins (Turbin et al., 1966; Kadirov, 1968; Chediya et al., 1976), and even has been carried to surfaces carved on bedrock in many major ranges (Chediya, 1986).

2.2 Regional sequence of terraces

Nested terraces occupy most intermontane basins in the Tien Shan, and certain major terrace levels have been identified and correlated from basin to basin based on geomorphology, Quaternary stratigraphy, pollen and other paleontology, soils, a few numerical dates, and correlation to global climate change (e.g., Grigorienko, 1970). This stratigraphic scheme, which allows preliminary correlation of terraces from basin to basin, has been used in nearly every previously published paper and field map about the Quaternary of the Tien Shan (e.g., Makarov, 1977; Abdrakhmatov, unpublished data).

The regional terrace sequence consists of four main divisions: Q_I = early Pleistocene, Q_{II} = middle Pleistocene, Q_{III} = late Pleistocene, and Q_{IV} = Holocene. Major divisions contain one to several sub-divisions, defined by a superscript, e.g., Q_{II}^2. Like the major divisions, younger subdivisions within each main division have greater numbers. For ease of formatting, I omit superscripts and subscripts in the text, replacing them by writing the subdivision number in parentheses (e.g., QII(2)). Although the exact number of terraces within each subdivision can vary locally, certain prominent terraces recur from basin to basin and drainage to drainage. From youngest to oldest, these are the QIV(1), QIII(2), QIII(1), and QII(2). The QIV terraces are typically low, inset terraces that commonly lie in an "inner gorge" set within the prominent

QIII(2) terraces (Figure 2.2). QIV terraces in the intermontane basins are typically cut or strath terraces, but can be fill terraces, especially in the larger basins. QIV terraces are commonly unpaired, although the QIV(1) in many places appears to be a paired terrace. The QIV(1) terrace is the most prominent of the post-QIII(2) terraces and is typically half the height of the QIII(2) terrace above the modern river. QIV(2) and QIV(3) terraces are less common than QIV(1) terraces, and commonly form straths within rivers deeply incised into the QIII(2) terrace, in the hanging walls of faults.

QIII terraces contain the broad, often extensive QIII(2) terrace that can be 10 to 100 m above the active stream (Figure 2.2). The terrace is paired, and can either appear as a fill terrace in fault footwalls, or as a strath in the hanging walls of active faults or in the cores of anticlines. Commonly, it is the most densely inhabited land, and is cultivated, because of its width, lack of dissection, and thick (~1–2 m), fine-grained eolian and colluvial cover. The QIII(3) terrace is not as common as the QIII(2) or QIII(1) terrace, and it appears as a narrow terrace cut into the riser of the QIII(2) terrace. It is typically less than a third the height of the QIII(2) terrace above the modern river, much higher than the QIV(1) terrace, but part of the "inner gorge" in areas of deep river incision.

The QIII(1) terrace, though the first prominent terrace above QIII(2), is neither as broad nor as extensive as the QIII(2) or older QII(2) terraces (Figure 2.3). It typically is cut into the riser of the QII(2) terrace in the hanging walls of faults or in the cores of anticlines. Gravel is commonly several meters thick above a rock-carved strath, and the terraces are covered with thick fine-grained sediment caps, mainly colluvium derived from the adjacent QII(2) terrace. Rilling and dissection of the surface are usually prominent and serve as a relative age indicator where compared with the lesser degradation of the younger QIII(2) terraces.

The QII(2) terrace is the most prominent of the QII terraces, and commonly occupies the margins of the river valley. In places it forms the drainage divide, and in others it is cut into higher hills of Tertiary strata (Figure 2.2). The QII(2) terrace is commonly a strath with a few to about ten meters of gravel, although it can be a fill terrace in structural lows such as synclines or fault footwalls. It commonly has several meters of fine-grained material overlying gravel: this

can range from thick deposits of poorly sorted colluvium, where the terraces are adjacent to valley walls, to thick accumulations of loess, particularly at the northern Chu basin. In some places the loess cover is absent or is mantled by small boulders. The geomorphic surface in places is dissected and eroded to the level of the Tertiary rock. The narrow QII(1) and QII(3) terraces, where present, are within a few to tens of meters above and below the QII(2) terrace, respectively (Figure 2.2d).

2.3 Chronology

2.3.1 Radiocarbon ages

Calibrated radiocarbon ages of charcoal samples support the correlation of the broad, paired QIII(2) terrace and immediately inset QIII(3) terrace in four drainage basis and three intermontane basins (Figure 2.3 and Table 2.1). These correlations show that river incision and terrace formation occurred widely during the global glacial-interglacial transition, which is dated to ~15 x 10^3 cal yr B.P. (Imbrie et al., 1984; Broecker et al., 1988; Fairbanks, 1989). Detrital charcoal samples collected from QIV(1) terraces indicate another period of terrace formation during the early to middle Holocene (Table 2.1).

Most detrital charcoal samples were collected from fine-grained sediments overlying the river gravel (Table 2.1). If the contact between gravel and fine-grained sediment that contains overbank deposits, eolian silt, and colluvium represents floodplain abandonment and river incision, then the first sediments deposited above the contact closely date or postdate the terrace formation (e.g., Merritts et al., 1994; Lavé and Avouac, 2000). Detrital charcoal, however, pre-dates the deposit from which it was collected because of a non-zero inherited age (a combination of an age of the plant and age of sediment reworking). This inherited age could be significant if the charcoal was stored for a long duration on a hillslope or higher terrace. In a few cases, reddish-colored soil was present near or within the sample horizon, suggesting that charcoal formed during a fire close to the sample location. For other samples, aside from after-the-fact consideration of the combined results, I simply assume that the inherited ages are small.

The calibrated age distributions of charcoal samples collected close to the QIII(2) and QIII(3) terrace gravel contacts overlap, with ~98% of the probability distribution between 13.5–15.7 x 10^3 cal yr B.P. (Figure 2.3a; Table 2.1). This result suggests that the radiocarbon ages sample the same event, even though these samples came from terraces in different drainage basins. Other factors, such as the time of incision of the QIII(2) to the QIII(3) terraces, the time of initial aggradation of fine-grained material after formation of the terraces, and the inherited age of charcoal fragments, appear small compared to the uncertainty in the age distribution. The similar ages from drainages with different-sized catchments and the dissimilar distances from major confluences (that may affect local base level) indicate that paleo-river incision occurred rapidly along the reaches we sampled.

The possible exception to the similar age of QIII(2) terrace formation comes from the Sokuluk River drainage, in the northern Chu basin (Figure 2.1). There, an infrared-stimulated luminescence age of fine-grained sediment covering a QIII(2) alluvial fan surface suggests that the fan may have been abandoned ~22 ka, or several thousand years earlier than ~13.5–15.7 x 10^3 cal yr B.P. I discuss that specific result in Chapter 4.

At the Kadjerty River in Naryn basin, three detrital charcoal samples collected from above and below the gravel-to-fine-grained sediment contact provide an opportunity to constrain the timing of local paleo-river incision and QIII(2) terrace formation (Figures 2.1, 2.3, and 2.4). Two charcoal samples (CAMS #51037 and 51038) were collected in sandy silt 10 and 30 cm above the contact between gravel and fine-grained sediments in a gully exposure ~2 km south of the fault scarp (Figure 2.4b; Table 2.1). The pooled mean radiocarbon age of the samples corresponds to 13.5–14.1 x 10^3 cal yr B.P. A charcoal sample (CAMS #51036) collected 10 cm below the upper gravel contact in an exposure across the fault scarp has an age of ~14.1–15.4 x 10^3 cal yr B.P. (Figure 2.4; Table 2.1). If the charcoal samples closely date the deposits (i.e., their inherited age is smaller than other uncertainties in their age measurement), and if the contact between the gravel and overlying sandy silt represents the incision of the paleo-river and formation of the QIII(2) terrace, stratigraphic superposition places constraints on the probability distribution of the age of the contact (Figure 2.3b) (Biasi and Weldon, 1994; Ramsey, 1998).

The calculated age distribution suggests river incision occurred between 13.6 and 15.2 x 10^3 cal yr B.P., with the most probable date of river incision around 14.1 x 10^3 cal yr B.P.

Radiocarbon ages of 47.9 ± 2.6 and 43.2 ± 3.3 x 10^3 ^{14}C yr B.P. show that the ancient floodplain of the Kadjerty River beneath the QIII(2) terrace aggraded slowly on average (Table 2.1). The samples of finely disseminated charcoal were collected about half-way up a ~60 m-thick exposure of river gravel in the footwall of the Kadjerty fault, from a lens of fine sand (Figure 2.5). The ages suggest an average gravel aggradation rate of ~1 mm/yr during the last glacial period. The >30 m of gravel below the sample site, if a constant sedimentation rate is extrapolated down, implies aggradation since at least ~60 ka to construct the QIII(2) terrace. However, it is possible that aggradation was highly episodic during the last glacial period.

2.3.2 Luminescence ages, QII(2) terrace

Silt overlying river gravel was collected for thermoluminescence (TL) and infrared-stimulated luminescence (IRSL) dating from four QII(2) terraces along three drainages in different intermontane basins (Figures 2.1 and 2.6; Table 2.2). For a TL or IRSL age to represent the time of deposition, silt grains within a sample must be sufficiently "bleached" by sunlight so as to empty heat- and light-sensitive electron traps (e.g. Aitken, 1985, 1998).

All the samples consist of silt to sandy silt from deposits 2–30 m thick that overlie fluvial gravel, and are interpreted to be a combination of flood overbank deposits, loess, and minor colluvium. For sample collection, pits were excavated at least 1 m into the fine-grained deposits at the terrace risers, close to the gravel contact (Figure 2.6). Luminescence samples were collected with two 8 oz light-tight aluminum tins spaced ~15 cm apart and at least 40 cm above the gravel contact (Figure 2.6b). Four 3 oz sample tins spaced ~30 cm above, below, and to the sides of the 8 oz tins collected extra material for determination of K, U, and Th, which affect the α, β, and γ radiation dose rates for the luminescence samples. Pedestals slightly higher and larger than the sample tins were carved into the back wall of the pit, and the sample tins were shoved over the pedestals, scraping off excess debris in the process. By this sample method only the material at the top and bottom of the tins was exposed briefly to sunlight, and this material

was removed in the laboratory prior to sample preparation. Brief notes on the analyses, performed by Glenn Berger at the Desert Research Institute, Reno, Nevada, are presented in Table 2.2. Details of the analyses are contained in a separate report (G. Berger, written communication, 2000).

Although the TL and IRSL ages of the QII(2) terraces have large uncertainties (Figure 2.6 and Table 2.2), and the samples collected from fine-grained sediments overlying river gravel represent minimum ages for the terraces, statistical tests of significance (Ward and Wilson, 1978) reject the hypothesis that the QII(2) ages come from different populations (test statistic $T = 2.51$; $\chi^2(0.05) = 7.81$) (see section 3.4 for a description of the test). To increase the precision for the slip-rate calculations based on deformed QII(2) terraces, I use the pooled mean age (140.7 ka) and standard deviation (square root of the variance of the pooled ages, 8.5 ka) of the TL/IRSL analyses. In Chapter 4 I report the mean and ~95% confidence interval as 141 ± 17 ka. This result indicates that the QII(2) terrace formed during the penultimate global glacial-to-interglacial transition, which U-Th dating and orbital tuning of Oxygen isotopes have dated to ~128–140 ka (Imbrie et al., 1984; Henderson and Slowey, 2000; Shackleton, 2000). Global mean temperature may have risen several thousand years before major changes in ice volume occurred during the penultimate glacial-to-interglacial transition (Shackleton, 2000).

2.4 Inferred process of terrace formation

Where rivers cross active faults and folds, changes in rates of rock uplift are reflected in patterns of erosion and deposition along a river profile: bedrock straths are prevalent in hanging walls and in the cores of anticlines (e.g., Figures 2.2c,d), and thick gravel fills are present in footwalls and synclines (Figures 2.2b and 2.5). The lateral variation in gravel thickness under the Kadjerty River QIII(2) terrace shows that during times of strath formation in the hanging walls of the faults, gravel accumulated over a strath on the flanks of hanging-wall anticline (Figure 2.5 and Figure 4.9c). This stratigraphic relationship, and the ~45 x 10^3 ^{14}C yr B.P. ages from within the gravel fill in the footwall of the Kadjerty fault, suggest that aggradation, on average, was slow during glacial times. Thus the strath is less likely to be of a similar age along a river that crosses an active structure than is the overlying contact between river gravel and fine-grained sediments. The recurring ~13.5–15.7 x 10^3 cal yr B.P. ages of detrital charcoal from near

the gravel–fine-grained sediment contact indicate that the rivers incised their floodplains rapidly. A rapid change from aggradation or planation to incision suggests that the terrace surfaces were originally flat.

The aggradation and incision of a river that crosses an active fault or fold depend on changes in space and time in the local rock uplift rate, the transport capacity and sediment supply of a river, and the local river baselevel (Figure 2.7). A near-equilibrium condition occurs if a river's sediment supply approximately equals transport capacity (Figures 2.7a,b). Lateral instabilities in this river system create meanders that will dissipate energy into meander channel walls and broaden a floodplain. With spatial differences in vertical crustal movement, and different positions of the river's baselevel, erosion and deposition will vary along the axis of the river valley. Excess shear stress at the base of a river will erode a strath terrace in the regions where vertical crustal movement exceeds base-level rise (Figure 2.7a,b); gravel deposition and aggradation will occur where crustal movement is less than base-level rise (Figure 2.7b).

If climatic conditions cause sediment supply to exceed the net transport capacity for the entire river, aggradation will raise the local baselevel and the river profile will rise as well (Figure 2.7c). If instead, climatic conditions cause net transport capacity to exceed sediment supply, a drop in local baselevel or adjustment to a new equilibrium elevation profile causes the river to incise into sediment or bedrock (Figure 2.7d). A change from near-stable conditions or aggradation to vertical incision causes floodplain abandonment and the formation of a paired river terrace. The rate of incision influences lateral and vertical river instabilities and hence the rate of lateral river migration, which determine a pattern of cut terraces in a newly created river valley (Figure 2.7d).

Once an incising river nears a new equilibrium elevation profile, in which vertical incision is small with respect to lateral migration, a new floodplain will begin to broaden (i.e., a return to Figures 2.7a–c). The relative heights of major terraces depend on 1) the vertical tectonic movement of an older terrace since its time of formation, and 2) the change in elevation of the river profile between the times the older terrace and the younger terrace formed. The preservation of older terraces depends in part on the amount of lateral river migration and

floodplain widening after the terrace is formed. This description is similar to explanations of preserved marine terraces (e.g., Lajoie et al., 1979) and coastal river terraces (e.g., Merritts et al., 1994), but differs in that the hydrologic balance between sediment supply and transport capacity of the regional river network, and not sea level, determines the rise and fall of baselevel.

The widespread incision of the QIII(2) terrace began ~13.5–15.7 x 10^3 cal yr B.P., similar to the ~14.7 x 10^3 cal yr B.P. date of an abrupt change in northern Hemispheric temperatures (Severinghaus and Brook, 1999), and clearly during the transition between full glacial and interglacial conditions (Broecker et al., 1988; Fairbanks, 1989). The coincidence suggests that the warming of the northern hemisphere resulted in the incision of rivers in the Tien Shan. Incision occurs when transport capacity exceeds sediment supply. Although glaciers occupied most high-elevation catchments, and warmer temperatures may have produced a greater melt-water discharge, it is probable that a sustained increase in transport capacity required more precipitation to fall across the entire drainage network. This is broadly consistent with pollen data that indicate cold and dry glacial periods and warm and wet interglacial periods in central Asia (Grigina and Fortuna, 1981), and Europe (Guiot et al., 1989).

Over many parts of southern and eastern Asia, the strength of the moisture-laden summer monsoons determines precipitation (e.g., An et al., 1991; Porter et al., 1992). The Indian and East Asian monsoons do not appear to affect the Tien Shan, however, as the Himalaya-Pamir belt and the Tibetan Plateau form a topographic barrier to precipitation. Under current conditions, the central Tien Shan derives most of its moisture from westerly storms during the spring and summer months (Atlas of Kyrgyz SSR, 1987). A change in surface temperature alone may have sufficed to change the amount of moisture carried by the westerly winds. Holding other atmospheric factors constant, a 10° C increase in air temperature at Earth's surface results in a doubling of the saturation vapor pressure (Peixoto and Oort, 1992). As saturation vapor pressure scales with the moisture capacity of an overlying atmospheric column, this translates to an approximate doubling of precipitation. A 5–10° C increase in temperature during the spring and summer months may be higher than expected for mid-latitude regions (e.g., p. 51–53, Crowley and North, 1991). Nevertheless, the zero-order effect of warming surface temperatures from glacial to interglacial conditions predicts additional precipitation over the Tien Shan. The

additional precipitation may have increased river discharge and transport capacity enough for rivers to incise their floodplains. Alternative mechanisms may involve latitudinal displacement of storm tracks during glacial periods due to the size of the Fennoscandian ice sheet or sea-ice extent in the North Atlantic (Kutzbach et al., 1993; Porter and An, 1995).

The "rapid" propagation of incision inferred from our radiocarbon ages—within a few thousand years—is much faster than the several thousand year duration of river incision along Cajon Creek in the San Gabriel Mountains of southern California (Weldon, 1986). The difference in the propagation of incision may be attributed to either the rate of sediment delivery to the river system, or to higher discharge and transport capacity of the rivers in the Tien Shan compared to Cajon Creek (Bull, 1991).

Table 2.1: Radiocarbon ages of river terraces.

Sample name	Lab code[a] (CAMS #)	River	Terrace	Height[b] (m)	material	$\delta^{13}C$[c] (per mil)	Radiocarbon age[d,e] (^{14}C yr B.P.)	Age range[f] (cal yr B.P.; 95.4%)	Area[g]
SCT/090899/8(4)	59758	Alamedin	QIII(3)	0.50	charcoal	-25	11,880 ± 40		
SCT/090899/8(5)	59760	Alamedin	QIII(3)	0.50	charcoal	-25	11,860 ± 50		
	pooled mean and standard deviation[h]			T'=0.01; $\chi^2(0.05)=3.84$			11,869[i] ± 102	14,250 - 14,230	0.007
								14,120 - 13,490	0.993
99/Koch2/e	57622	Djuanarik	QIII(2)	1.10	charcoal	-25	11,700[i] ± 50	13,960 - 13,940	0.004
								13,900 - 13,450	0.996
97TS-K-15	41961	Djuanarik	QIV(1)	0.26	shell	-6	5520 ± 50	6410 - 6270	0.873
								6250 - 6200	0.127
97TS-K-29S	41962	Djuanarik	QIV(1)	0.01	shell	-6	5730 ± 40	6630 - 6440	0.978
								6420 - 6420	0.022
97TS-K-29C	42155	Djuanarik	QIV(1)	0.01	charcoal	-25	5580 ± 60	6490 - 6280	1
97TS-K-16	42154	Djuanarik	QIV(1)	0.02	charcoal	-25	5220 ± 70	6180 - 5880	0.947
								5820 - 5760	0.053
SCT/080697/18	59761	Djuanarik	QIV(1)	0.32	charcoal	-25	4990 ± 40	5890 - 5810	0.201
								5760 - 5610	0.799
98/Krft/11	51036	Kadjerty	QIII(2)	-0.10	charcoal	-25	12,340[i] ± 40	15,430 - 14,540	0.567
								14,440 - 14,110	0.433
98/Krt/1	51037	Kadjerty	QIII(2)	0.30	charcoal	-25	11,930[i] ± 50	14,260 - 14,220	0.018
								14,110 - 13,640	0.982
98/Krt/2	51038	Kadjerty	QIII(2)	0.10	charcoal	-25	11,770[i] ± 50	14,020 - 13,490	1
98/Krft/8	51034	Kadjerty	QIII(2)	1.10	charcoal	-25	8000 ± 40	9010 - 8720	0.989
								8710 - 8700	0.011
98/Krft/23	51035	Kadjerty	QIII(2)	0.80	charcoal	-25	8330 ± 40	9470 - 9260	0.962
								9170 - 9150	0.038
98/Krft/3	51046	Kadjerty	QIII(2)	1.45	shell	0	6500 ± 50	7550 - 7540	0.018
								7500 - 7290	0.982
98/Krcf/6	51161	Kadjerty	QIII(2)	-30	charcoal	-25	47,900 ± 2600	n/a	
RJW/072798/TJ6	59759	Kadjerty	QIII(2)	-30	charcoal	-25	43,200 ± 3300	n/a	

Table 2.1: Radiocarbon ages of river terraces (continued).

Sample name	Lab code[a] (CAMS #)	River	Terrace	Height[b] (m)	material	$\delta^{13}C$[c] (per mil)	Radiocarbon age[d,e] (^{14}C yr B.P.)	Age range[f] (cal yr B.P.; 95.4%)	Area[g]
99/Kurtka/5	57606	Kurtka	QIII(3)	0.30	charcoal	-25	12160 ± 50		
99/Kurtka/10	57607	Kurtka	QIII(3)	0.30	charcoal	-25	12190 ± 80		
(0.19 mg C)	pooled mean, standard deviation[h]			T'=0.03; $\chi^2(0.05)=3.84$			12172[i] ± 80	15,380 - 14,600	0.403
								14,380 - 14,030	0.504
								13,960 - 13,830	0.092
SCT/091899/8	59757	Djergetal	QIV	0.53	char	-25	4690 ± 50	5580 - 5510	0.189
								5490 - 5310	0.811
98/Alb/1	57608	At-Bashi	QIV(1)	?	char	-25	6730 ± 50	7680 - 7550	0.822
								7540 - 7500	0.178
99/TashRabat/1	57604	Ottuk	QIV(1)	0.20	char	-25	9840 ± 50	11,330 - 11,320	0.023
								11,300 - 11,170	0.997
99/TashRabat/5	57605	Karakol	QIV(?)	0.50	shell	-8	8270 ± 50	9460 - 9120	0.964
								9110 - 9040	0.036
Estimated age of QIII(2) terrace formation by combining calibrated ages of *i*								15,740 - 13,470	0.979

[a] Samples run at Center for Accelerator Mass Spectrometry, Lawrence Livermore National Labs.

[b] Height of collected sample above or below the upper gravel contact of the terrace.

[c] $\delta^{13}C$ values are assumed according to Stuiver and Polach (1977).

[d] The quoted age is in radiocarbon years using the Libby half life of 5568 years and following the conventions of Stuiver and Polach (1977).

[e] Sample preparation backgrounds have been subtracted, based on measurements of samples of 14C-free coal and limestone. Backgrounds were scaled relative to sample size.

[f] Calibrated using CALIB v 4.3 (Stuiver and Reimer, 1993) and the calibration dataset in Stuiver et al. (1998).

[g] Relative area under the probability distribution that lies within the 95% confidence limits.

[h] Calibration of pooled radiocarbon ages described in CALIB manual. T' = test statistic; T' $<\chi^2$ if not statistically different at 95% confidence.

[i] Calibrated age distributions of these radiocarbon ages were combined to determine the age range of QIII(2) formation.

Table 2.2: Thermoluminescence and infrared-stimulated luminescence data and ages of QII(2) terraces.

Sample code Lab number [a,b]	Dose rate [c] ±1σ (Gy/ka)	Mode	Preheat [d]	Bleach [e]	Equivalent dose [g], ±1σ (Gy)	Time/Temp [h] (s)/(°C)	Age [i] ±1σ (ka)	Location	Material; thickness of deposit (m) Height above gravel (m)
SCT/090899 TIEN99-1	5.55±0.60	IRSL	160°C/2d	780/2h	943±96	1-10s	170±25	Alamedin R., Chu basin	Silt; 30 2.65
98-Koch-Q2 TIEN98-1	5.01±0.32	IRSL	150°C/2d	780/2h	679±76 [f]	1-10s		Djuanarik R., Kochkor basin	Silt; 4 0.20
		IRSL	170°C/2d	780/2h	589±81 [f]	1-50s			
		TL	160°C/2d	400/3d	644±79 [f]	330-210°C			
		TL	160°C/2d	FSL/8h	742±91	330-210°C			
			Weighted mean of f = 639±45				128±13		
SCT/091699 TIEN99-2	4.45±0.34	IRSL	160°C/2d	780/2h	667±87	1-40s	150±23	Djergetal R., Naryn basin	Sandy silt; 2.7 0.30
SCT/091899 TIEN99-3	4.51±0.26	IRSL	160°C/2d	780/2h	423±35	1-30s	93.8±9.0 [k]	Djergetal R., Naryn basin	Sandy silt; 1.7 0.30
		TL	145°C/2d	FSL/6.5h	644±57	260-390°C	143±15		

[a]Sample preparation and measurements at the Desert Research Institute, Reno, Nevada.
[b]Polymineralic, non-carbonate, detrital 4-11 μm diameter size fraction was used for all TL and IRSL measurements. Luminescence was detected at the 420±20 nm spectral region (bandpass 390-470 nm at 1% cut). Laboratory sample-preparation procedures follow Berger (1990).
[c]Effective dose rate, D_R, is derived from independent measurements of U, Th, K and water concentration. D_R is calculated with the conversion factors and equations given by Berger (1988), and includes a cosmic ray component varying from 0.03 to 0.17 with estimated average depth, from the data of Prescott and Hutton (1988).
[d]The chosen pre-readout heating and duration (days) (to empty laboratory-filled electron traps). Pre-heating was applied after bleaching.
[e]Bleaching protocol (FSL = full solar spectrum at Reno; 400 = laboratory Hg-vapor lamp with 400-750 nm passed; 780 = > 780 nm solar spectrum passed), and duration (hours or days)
[g]Weighted mean equivalent dose plus average error over time/temperature interval in the next column. A weighted-saturating-exponential regression and error model (Berger et al., 1987) was employed for all samples. For some IRSL samples, inter-aliquot scatter was minimized by short-shine normalization (to natural signals) (Ollerhead et al., 1994).
[h]The readout (LED-on) time interval or the temperature interval (if TL) for which D_E is calculated
[i]Luminescence age t = Equivalent dose / Dose rate
[k]Measurement rejected because it is significantly different from the TL measurement of the same sample, and the TL age is not significantly different from the age of sample TIEN99-2, collected from a stratigraphically similar terrace ~1.5 km away.

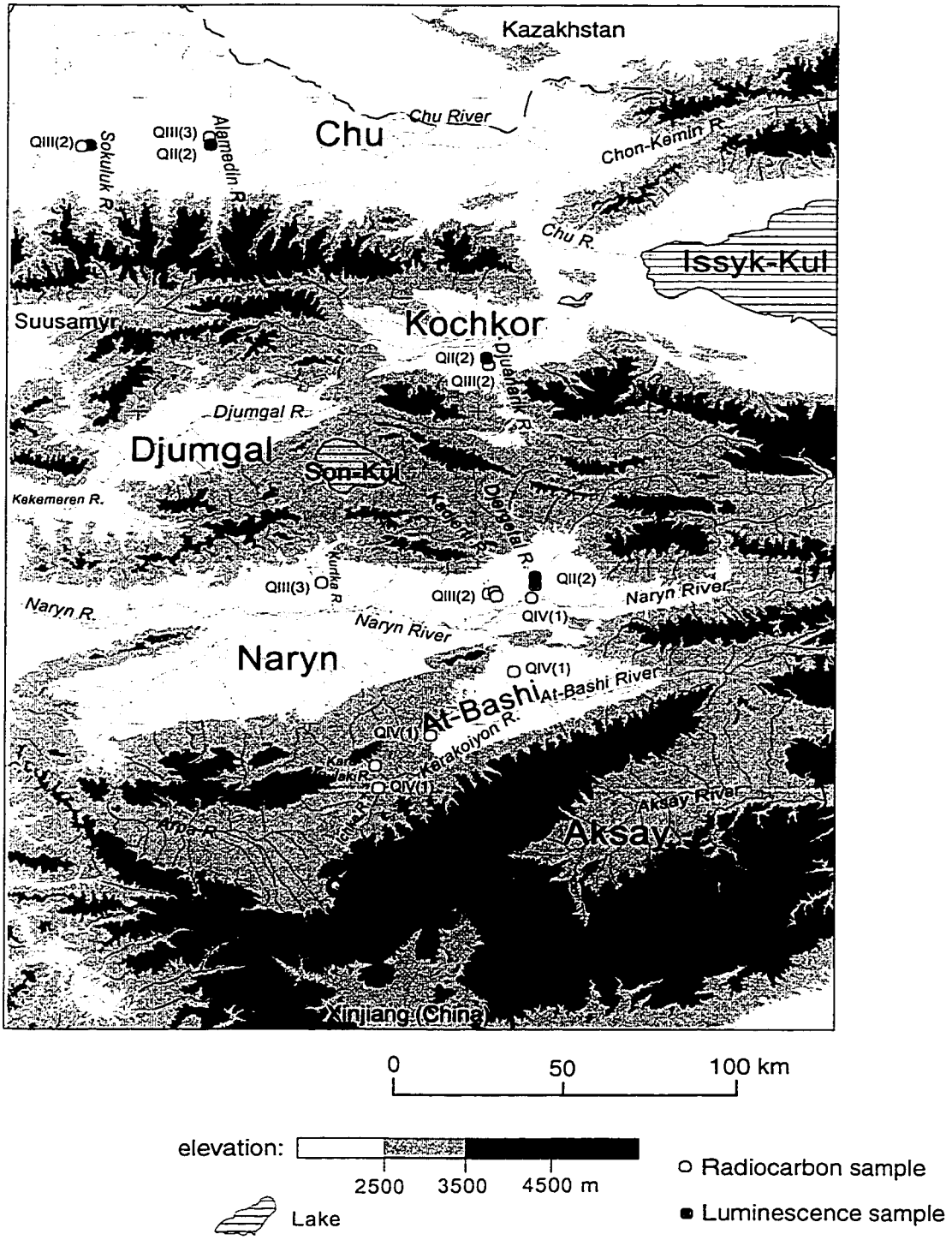

Figure 2.1: Drainage network of the central Kyrgyz Tien Shan. Basin names are in large font. Circles show locations of radiocarbon and luminescence samples that constrain the timing of river incision and terrace formation. Stratigraphic level of the terrace is indicated adjacent to the symbol. Ages are reported in Tables 2.1, 2.2, 6.1, and 6.2.

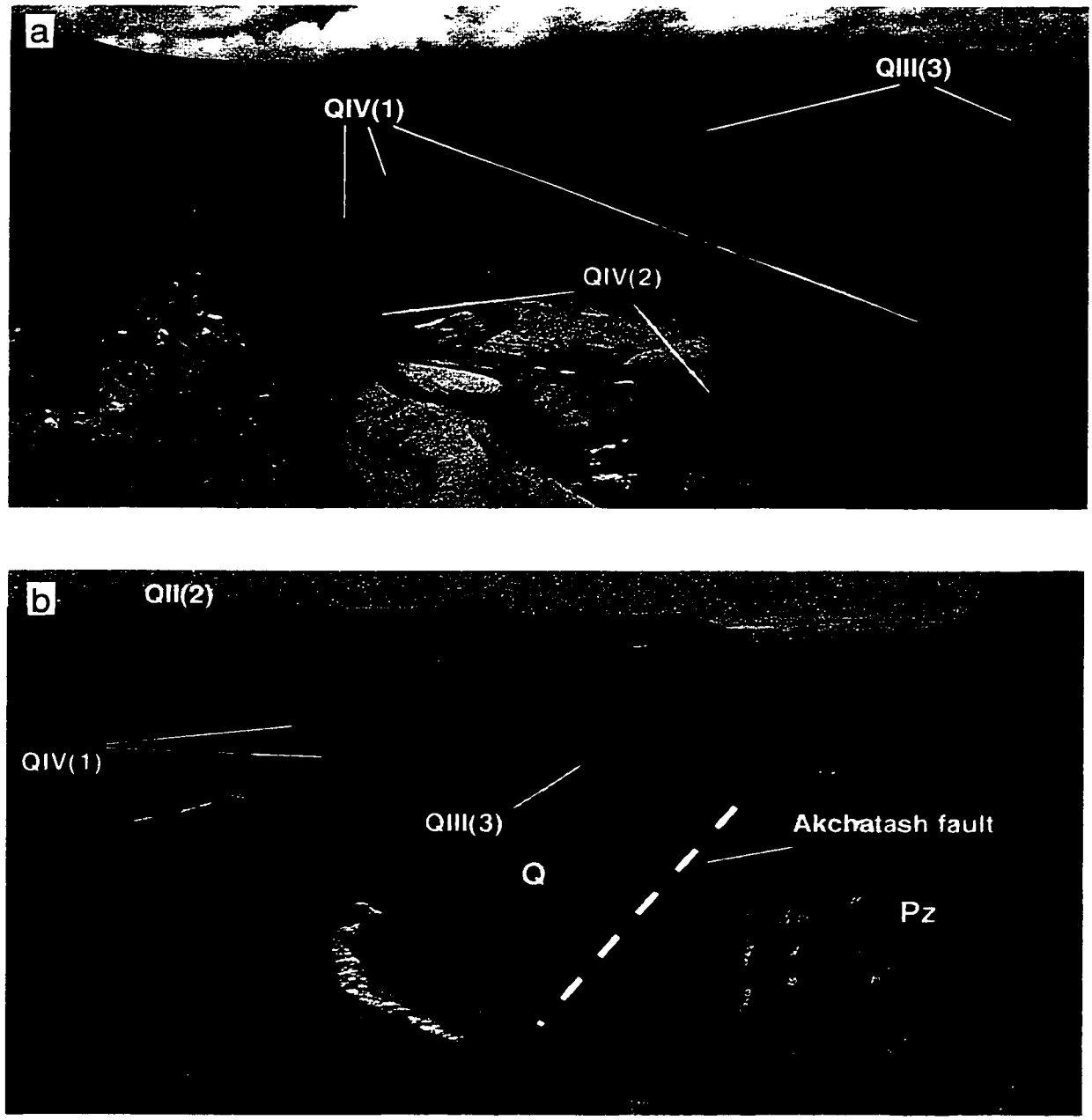

Figure 2.2: Terrace stratigraphy along the Kadjerty River, Naryn basin. (a) View north of terraces inset to the QIII(2) terrace. Note the thick gravel fill beneath the QIII(2) terrace, and the tilted Neogene strata beneath the QIV(2) terrace. Fine-grained sediment overlying gravel is visible in the left foreground. Photo by J. Lave, 1998. (b) View south from the Moldo-Too range front at the Kadjerty River terraces. Gravel fill beneath the QIII(2) terrace is greater than 100 m here. The Akchatash fault, visible on the right side of the photo, places Paleozoic limestone (Pz) on Quaternary gravel (Q) along a steeply dipping reverse fault. Photo by M. Miller, 1998.

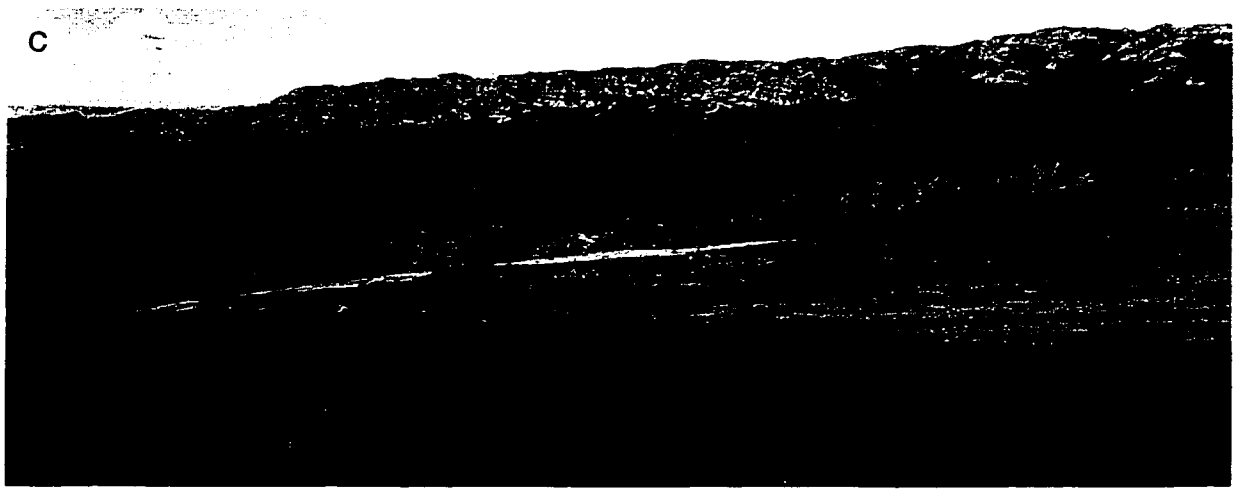

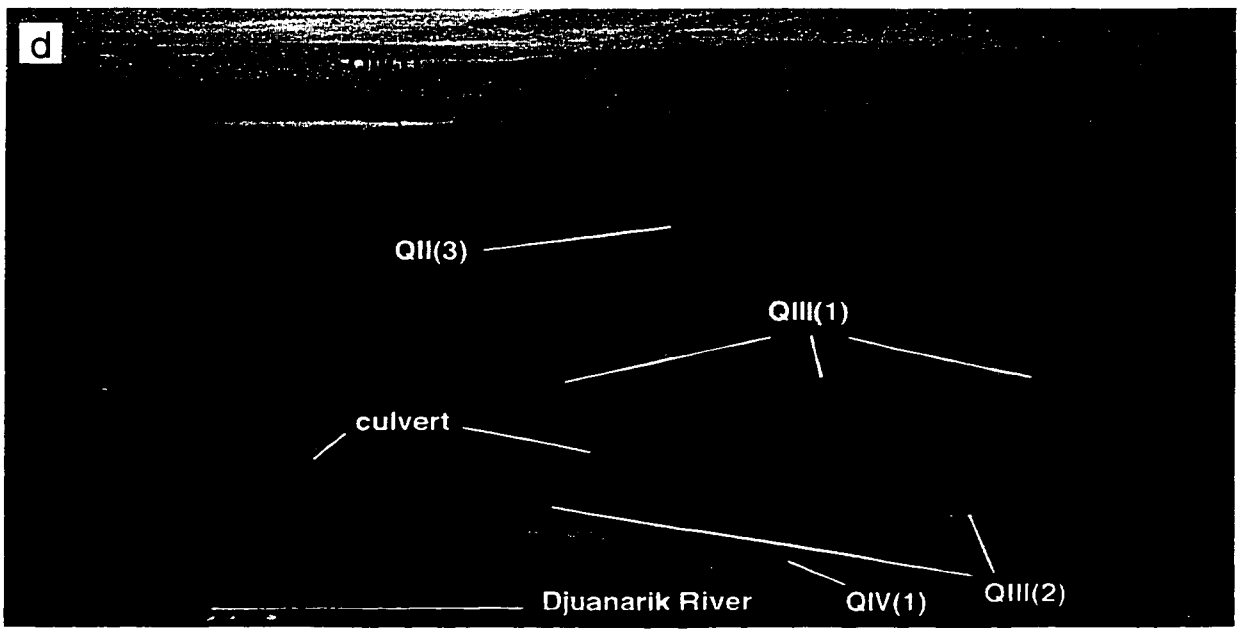

Figure 2.2 continued: (c) Broad tread of the Kadjerty River QIII(2) terrace. The sharp tonal contrast seen in the foreground indicates the limits of irrigation of the field. Note the tilted Neogene strata and ~10 m-thick gravel beneath the terrace exposed in the river bank. Arrow marks the charcoal sample site shown in Figure 2.4. (d) Southeast view of the Djuanarik River strath terraces, Kochkor basin. Tilted Neogene strata underlying the QII(2) and QII(3) terraces reveal the core of the hanging-wall anticline of the Akchop Hills fault. Gravel overlying the strath terraces is ~1-2 m thick. Note the thick colluvium overlying the QIII(1) and QIII(2) terraces that are inset to the QII terraces. Photo by M. Miller, 1997.

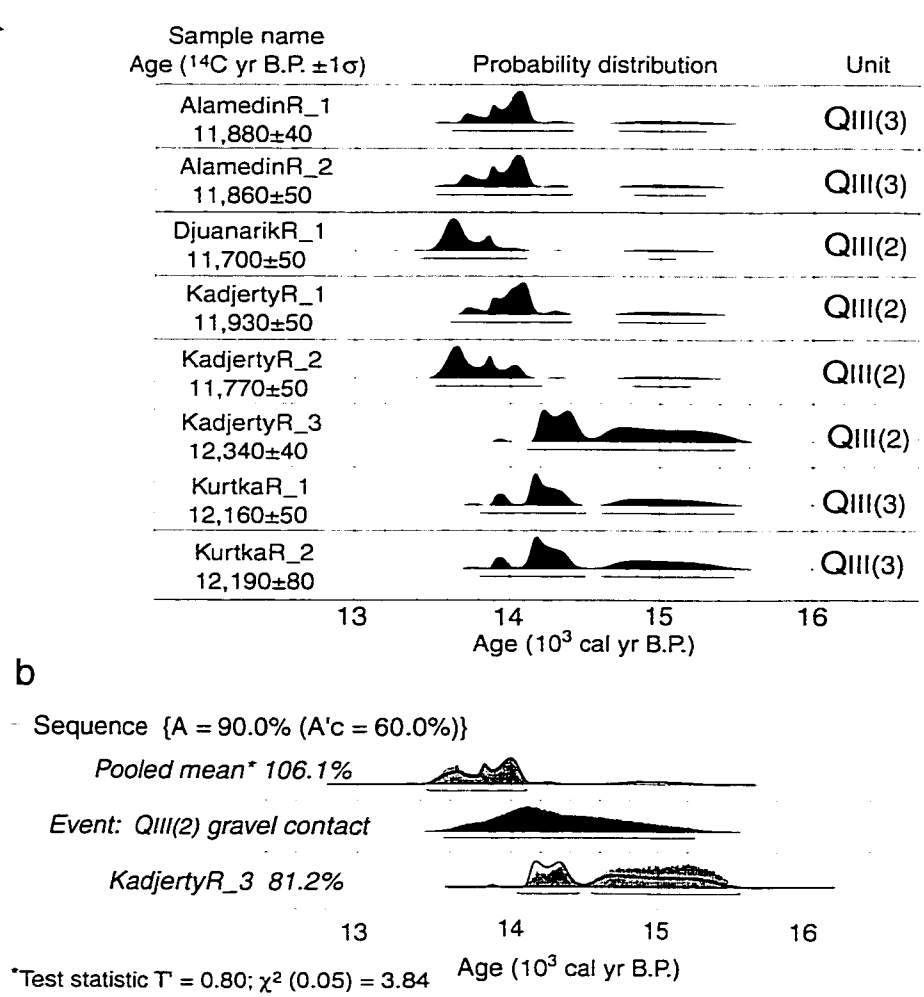

Figure 2.3: (a) Radiocarbon calibrated age probability distributions for eight detrital charcoal samples collected from the $Q_{III(2)}$ and $Q_{III(3)}$ river terraces (Table 2.1). Sample locations are shown in Figure 2.1. The similar calibrated age ranges suggest that river incision and river terrace formation occurred during a short time interval around 13.5-15.7 x 10^3 cal yr B.P. in several intermontane basins. Calibration plots generated by Oxcal v. 3.5 (Ramsay, 1998) with the calibration data from Stuiver et al. (1998): horizontal bars beneath distributions indicate 95% confidence intervals. (b) Age analysis of the $Q_{III(2)}$ terrace at the Kadjerty River, Naryn basin, using OxCal. The goal is to describe statistically the age distribution of the terrace forming "event," which is represented by the contact between coarse gravel and overlying silt and fine sand. Samples KadjertyR_1 and _2 overlie the "event" contact. The calibrated age distribution of the pooled mean radiocarbon age of these two samples is indicated by the black line (similarity test described in Ward and Wilson (1978)). Sample KadjertyR_3 underlies the "event" contact. Its calibrated age distribution is indicated by a black line. The age analysis of the "event" uses Bayesian statistical methods described in Ramsey (1998). The grey areas indicate the reweighted age distribution based on the additional constraint of stratigraphic order. The *a posteriori* age distribution of the "event" contact is determined from the reweighted distributions of the sample ages and an unconstrained *a priori* distribution of the "event." The agreement index indicates the extent to which the final (*a posteriori*) sample age distribution overlaps with the original (*a priori*) sample distribution. Index values below 60% are questionable (this level of disagreement is very similar to that for the 5% level chi-squared test). The overall agreement index A exceeds the critical agreement A'c.

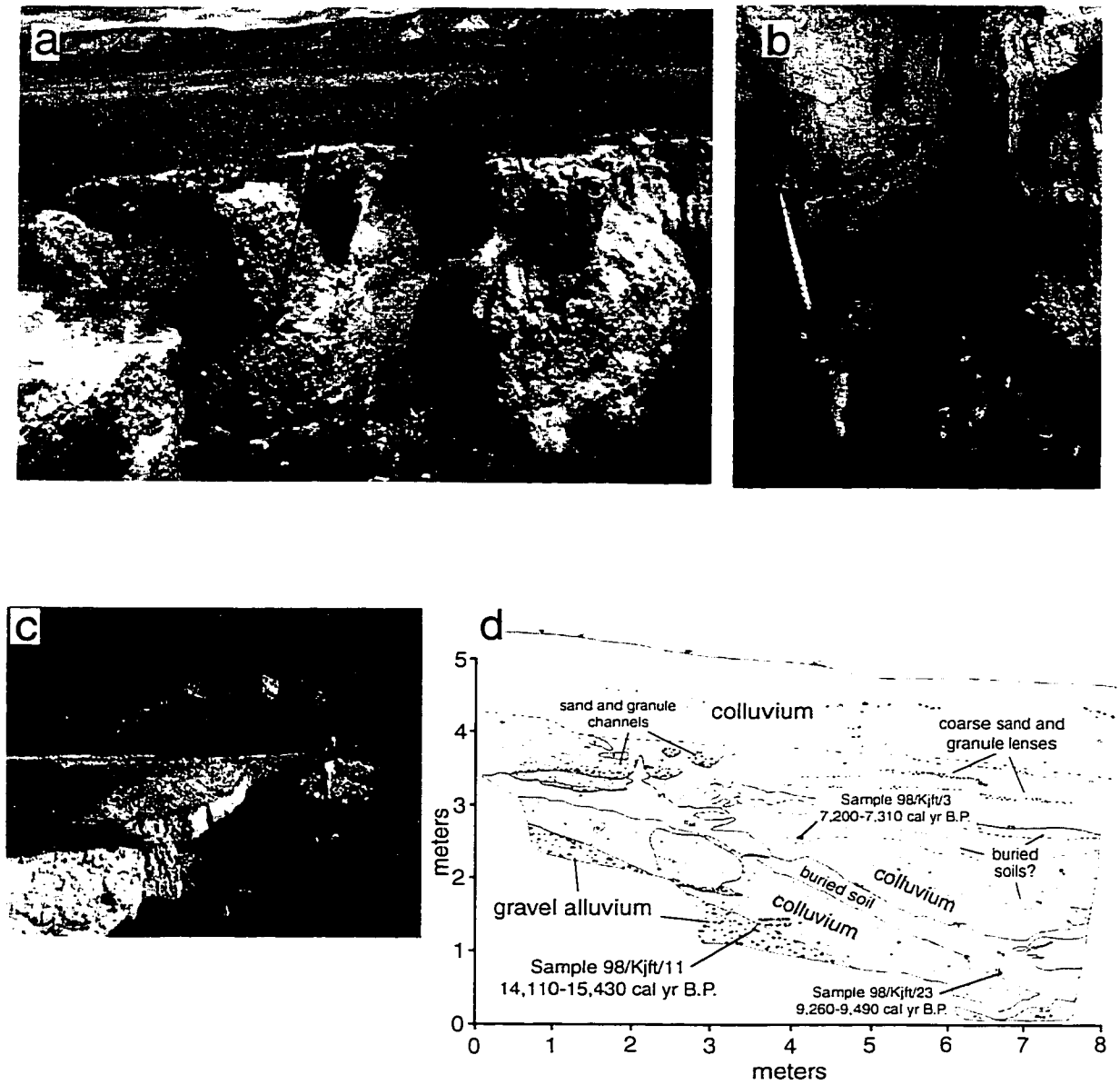

Figure 2.4: Locations of detrital charcoal samples that constrain the age of the QIII(2) terrace along the Kadjerty River in Naryn basin. (a) Northeast view of gully in the $Q_{III(2)}$ terrace between the Kadjerty and Central Naryn faults exposes fluvial gravel and overlying fine-grained sediments. The fine-grained sediments are ~2 m thick here. (b) Sample site for Kadjerty_1 and Kadjerty_2, located just to the right of (a). Handle of tool is about 30 cm long, and is resting on the gravel contact. Samples were collected 30 and 10 cm above the contact, below the lens of pea gravel next to the tool. (c) North view of gully and trench across the $Q_{III(2)}$ fault scarp near the $Q_{II(2)}$ terrace riser exposes terrace gravel and charcoal. (d) Log of east wall of trench exposing the gravel contact and location of sample 98/Kft/11.

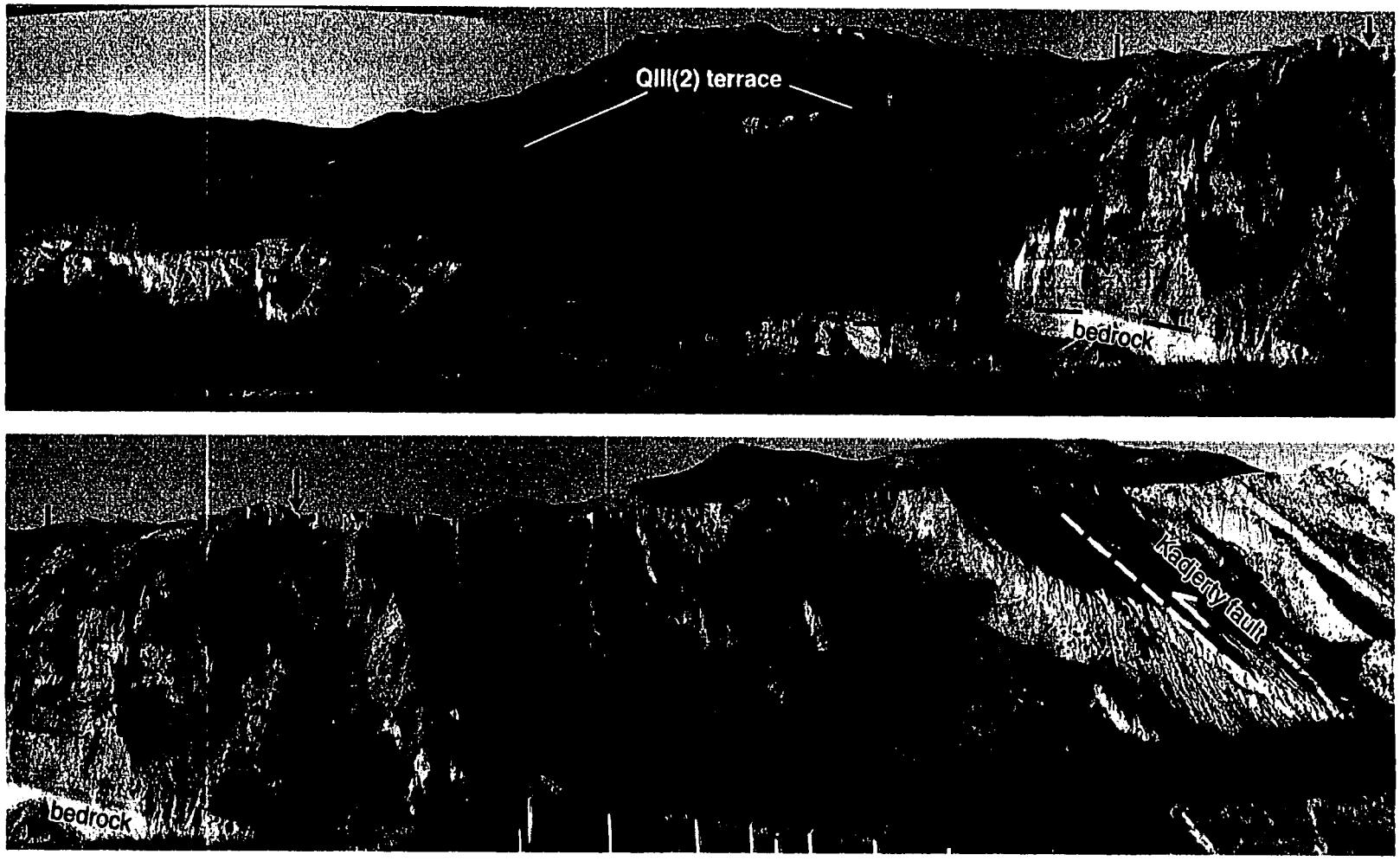

Figure 2.5: Photomosaic of the Kadjerty River QIII(2) terrace downstream of and across the Kadjerty fault, Naryn basin. View extends from south-southwest to west. Upper panel shows the thickness of the gravel overlying the Neogene bedrock strath increasing from ~10 m at the distant left side to ~60 m at the right side. Short bars mark the contact. An arrow within the thick exposed gravel at the right side of the photo marks the location of detrital charcoal samples that date to ~45 ka. Lower panel shows a continuation of the mosaic upriver to the north-dipping Kadjerty fault, which places Neogene strata over gravel. Overlap of the upper and lower panels is indicated by vertical arrows at the top of the QIII(2) terrace.

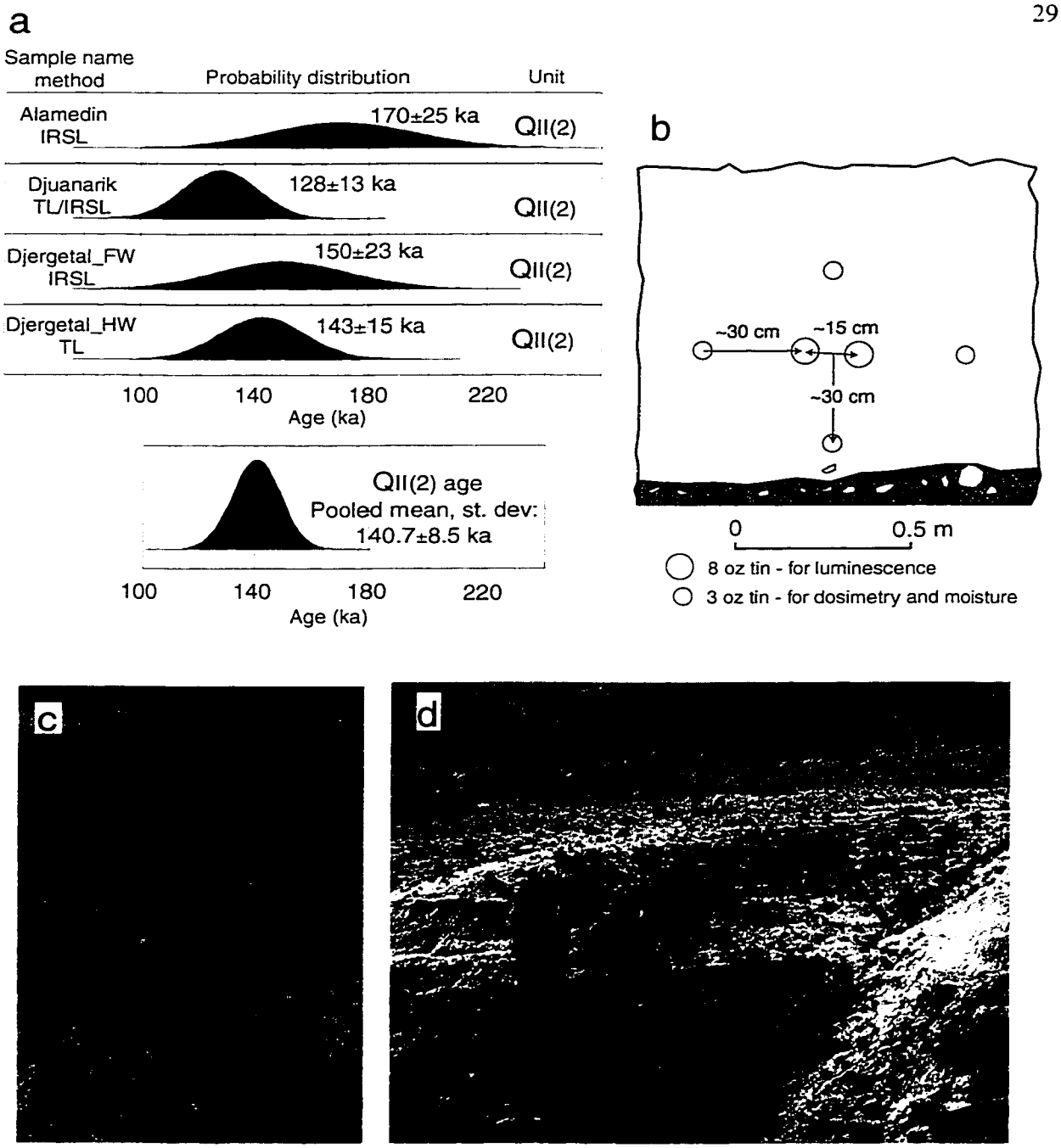

Figure 2.6: Details of luminescence dating. (a) TL and IRSL age distributions (1σ shown) of silt collected from fine-grained sediments covering $Q_{II(2)}$ terraces (Table 2.2). Sample locations are on Figure 2.1. The Djergetal River samples were collected from terrace treads correlated across a fault, and are about 5 km apart. The pooled mean age and standard distribution (square root of variance) of the four ages is shown below the individual age distributions; I use the pooled distribution for the age of the $Q_{II(2)}$ terrace in the slip-rate calculations (Chapter 4). (b) Sketch of sampling method. (c) Alamedin River (Chu basin) QII(2) terrace sample site (location shown on Figure 4.2). Sample pit was located ~2.5 m above the gravel contact. Person is next to the pit for scale. Total height of silt is about 30 m. (d) Djuanarik River (Kochkor basin) QII(2) terrace sample site. Pit was excavated close to the gravel contact. People at the top of the ~4-m-high silt cap provide a scale.

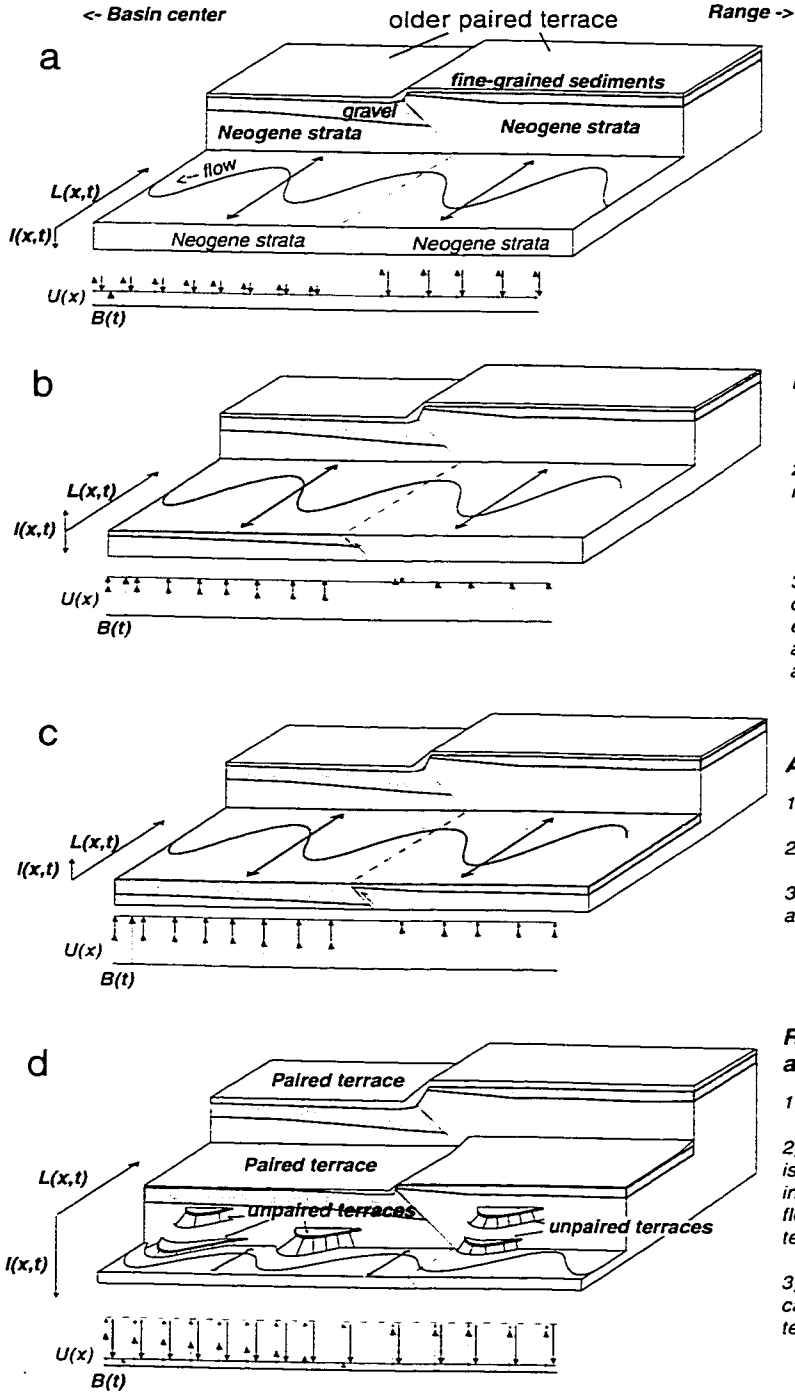

Near-equilibrium condition:

1) Sediment supply ~ transport capacity

2) Equilibrium river elevation profile with respect to a slowly changing baselevel (river incision -dI/dt ~ baselevel dB/dt < rock uplift dU/dt).

3) Lateral instabilities cause river meandering dL/dt >> vertical incision dI/dt; dissipation of energy into channel walls causes lateral cutting & strath formation.

Near-equilibrium condition II:

1) Sediment supply ~ transport capacity

2) Equilibrium river elevation profile with respect to a slowly changing baselevel.
-dI/dt < dU/dt in the hanging wall;
-dI/dt > dU/dt in the footwall.

3) Lateral instabilities cause river meandering dL/dt >> vertical incision dI/dt; dissipation of energy into channel walls causes lateral cutting and strath formation in hanging wall; lateral cutting and deposition in footwall.

Aggradation:

1) Sediment supply > transport capacity

2) Rise in baselevel dB/dt > rock uplift dU/dt

3) Aggrading channel system deposits wedge of alluvium (gravel) over broad floodplain (dI/dt > 0).

River incision and floodplain abandonment:

1) Transport capacity > sediment supply

2) Drop in baselevel dB/dt; river channel is out of equilibrium elevation profile and incises into bed. Vertical incision (dI/dt << 0) causes floodplain abandonment and forms a paired terrace.

3) Incision dI/dt ~ lateral migration dL/dt. River carves a narrow valley and creates unpaired terraces.

Figure 2.7: Inferred formation of river terraces across active faults in the intermontane basins of the Tien Shan. This sequence is modeled on the Kadjerty River in Naryn basin (Figure 2.5). I assume that these general relationships among transport capacity, sediment supply, uplift rate, U(x), and local baselevel, B(t), apply to all the terraces we have studied.

Chapter 3

Methods for calculating slip rate

Although the slip-rate equation—displacement, s, divided by time, t —appears straightforward, investigators are obligated to agonize over details encountered in each particular situation. The study of active faults in the Tien Shan is facilitated by a combination of high rates of fault-related fold deformation, extensive preservation of terraces, and often continuous exposure of deformed Neogene strata. Based on the available data, I have used some new approaches (as far as I know) to calculate fault slip rates using deformed terraces. Sections 3.2 and 3.3 illustrate methods for calculating slip rates for an offset river terrace and for terraces deforming in response to fault-bend folding. The fault-bend folding analysis presented in section 3.3 has proven useful in cases where river aggradation has buried the correlative surface in the footwall of the fault, because slip rate may be calculated based on fold growth within the hanging wall only, and does not require an assumption about changes in river elevation through time (e.g., Lavé and Avouac, 2000).

Frustrations with the subjective nature of evaluating and propagating uncertainties in field data (e.g., the commonly used "best estimate" and "estimated uncertainties") have led to a different approach that cleverly hides the unavoidable use of "expert opinion" in field work. Field measurements commonly have uncertainties that are described by a combination of normally distributed and asymmetric probability distributions. Radiocarbon age calibrations have probability functions that are complicated (Stuiver and Reimer, 1986). Section 3.4 describes a method for evaluating uncertainties though Monte-Carlo simulations that allow different probability distributions for each variable in the slip-rate equation. I use this method for calculating slip rates in Chapter 4 and for converting slip rates to north-south shortening rates in Chapter 5. Results are presented graphically with a histogram, and described in the text by the most probable value and 95% confidence limits. The histograms show that in many situations slip-rate uncertainties are highly asymmetric, indicating that structure in the uncertainty distribution may be lost if all variables and outcomes are forced to fit a gaussian distribution.

3.1 Collection of field data

Profiles of deformed river terraces, trench walls, natural exposures of faults, and radiocarbon and luminescence ages all provide data for measuring fault slip rates. We surveyed river terrace treads and fault scarps with a laser-distance theodolite (total station) and with pairs of GPS receivers set up to allow differences in position to be measured. Uncertainties in relative positions made with these instruments are less than a few decimeters and are less than the local variability in the position of the geologic contacts or geomorphic surfaces that we measured. For river terraces covered with thick or variable deposits of loess or colluvium, we surveyed the contact between fluvial gravel and overlying fine-grained deposits. This contact surpasses the strath as a strain marker because 1) the strath appears to have formed at different times along the terrace profile, particularly depending on the local vertical component of slip, and 2) the samples collected for dating constrain the age of the contact between gravel and overlying fine-grained sediments. The age of this contact approximates the onset of river incision, which results in the abandonment of the floodplain and thereby the formation of a terrace (Chapter 2). The assumption is that the terraces originated as planar surfaces over distances of several hundred meters to a few kilometers.

Geologic mapping at each site provides data to infer the fault geometry and to relate the terrace deformation to fault slip. Because most late Quaternary faults we examined lie within the well bedded Cenozoic strata of intermontane basins, mapped bedding dips and fault traces allowed us to draw preliminary cross-sections that use simplified fault-related fold geometries (Suppe, 1983; Suppe and Medwedeff, 1990) and predict subsurface fault geometry in the absence of subsurface data. The terraces that cross these active faults have been deformed less than the Cenozoic strata. Similar to growth strata (Suppe et al., 1992; Suppe et al., 1997), the terraces can be used to test the geometric and kinematic predictions of fault-related fold deformation (e.g., Lavé and Avouac, 2000; Pinter, 2001).

3.2 Slip rate calculation for an offset river terrace

Consider a fault that has cut an originally planar river terrace. The measurements are points surveyed along the terrace surface and across the fault. To calculate the amount of fault slip that

has offset the terrace, I first rotate and project all field data onto a vertical plane normal to the strike of the fault. Surveyed points from the river terrace treads define the strain markers for hanging-wall and footwall deformation. Least-squares linear regressions of these points in an x-y coordinate system give the mean and standard error of both the slope and the intercept of lines that represent the hanging wall ($y_h = m_h x + b_h$) and footwall ($y_f = m_f x + b_f$), where the tangent of the terrace dip, tan $\alpha = m$ (Figure 3.1).

Fault dip, δ, is determined by direct measurement, by surveying the position of the fault scarp across at least two nested terraces, or by estimation based on geomorphic expression (section 3.4). For parallel strain markers in the hanging wall and footwall, the vertical separation is $v = b_h - b_f$, and the dip-slip component s is

$$s = \frac{v}{\sin\delta + m\cos\delta}$$

or

$$s = \frac{v\cos\alpha}{\sin(\alpha+\delta)}. \tag{1}$$

If the hanging-wall and footwall strain-marker surfaces are not parallel ($m_h \neq m_f$), the calculated vertical separation is a function of horizontal distance

$$v(x) = x(m_h - m_f) + b_h - b_f, \tag{2}$$

and the dip-slip calculation requires a knowledge of the position (or projection) $P(x,y)$ of the fault tip onto the scarp (Figure 3.2). A line between the top and bottom of the scarp $y = m_s x + b_s$ contains all possible points P. I divide the amount of dip slip into two parts: the distance from the footwall projection up to P,

$$s_f = \frac{x(m_s - m_f) + b_s - b_f}{\sin\delta + m_f\cos\delta} \tag{3}$$

and the distance from the hanging wall down to point P,

$$s_h = \frac{x(m_h - m_s) + b_h - b_s}{\sin\delta + m_h \cos\delta}. \tag{4}$$

Therefore,

$$s = s_f + s_h \ . \tag{5}$$

Assuming that the terraces have deformed by incremental slip during earthquakes, I incorporate an additional uncertainty in slip rate due to the earthquake cycle (Sieh and Jahns, 1984). Paleoseismic data from trench excavations suggest that major ground-rupturing earthquakes on individual faults recur on the order of one to several (~1–5) thousands of years (Chapter 6). Hence, deformation of a ~15 ka terrace may have occurred during a few earthquakes. To incorporate uncertainty due to the earthquake cycle, I follow Lavé and Avouac (2000) and consider that some elastically stored slip Δs may be presently stored, and some elastically stored slip Δs_o may have been stored at the time of terrace formation. In the Monte Carlo simulations, I add the additional terms $\Delta s - \Delta s_o$ to s.

Datable material collected from fine-grained sediments covering river-terrace gravel or from within a confined deposit offset by a fault provides a measure of the time since formation of the strain marker, t. Hence, the dip-slip rate, u, for the case of an offset terrace is:

$$u = \frac{s + \Delta s - \Delta s_o}{t}. \tag{6}$$

3.3 Measuring slip rate with fault-bend folding of terraces

Consider a terrace that has been deformed by fault-related folding, whereby the terrace's surface is folded in the hanging wall of the fault but is buried by aggradation in the footwall. I propose a method to calculate the amount of fault slip from profiles of deformed terrace treads and measurements of deformed strata exposed in terrace risers beneath them. A valid geometric and kinematic interpretation of the fault-related folding must be compatible with both the terrace deformation and the underlying geologic structure.

Observations in the field indicate that attitudes of Tertiary beds are well approximated by kink-style geometry, with sections of relatively constant dip (dip panels) separated by narrow axial surfaces. Fault-bend fold theory states that bedding-parallel slip accommodates the folding of hanging-wall strata across abrupt fault bends to produce a series of dip panels separated by narrow axial surfaces (Suppe, 1983). If an unconformity (e.g., terrace) crosses a series of dip panels and axial surfaces, the unconformity will deform across active axial surfaces that project to bends in active faults, but will not deform across inactive axial surfaces that indicate finite fault displacement or project to inactive fault bends (Figure 3.3). Under idealized conditions of planar fault sections and a planar axial surface, slip across a fault bend will create two bends in an overlying unconformity that form a fold limb: one bend coincides with the active axial surface (e.g., axial surfaces A and B in Figure 3.3), and another occurs across an inactive axial surface that marks the amount of rock that has passed through the fault bend (e.g., A″ and B″ in Figure 3.3b). This inactive axial surface is not present in the underlying strata. The prediction for "kink-band migration" is that nested terraces will show progressively longer fold limbs, with a shared active axial surface that projects to an active fault bend, and separate inactive axial surfaces that each mark the amount of displacement on the underlying fault (Figure 3.3c). Note in Figure 3.3 that the angles of the fold limbs are predicted to remain constant. Other fault-related fold geometries, such as décollement folds and folds above curved faults, would predict deformation of the unconformity that appears as limb rotation as opposed to kink-band migration (e.g., Erslev, 1986; Rockwell et al., 1988; Pinter, 2001).

In the evaluation of folded terraces in the Tien Shan, the first step is to rotate the terrace profile in the vertical plane so that axes are parallel and perpendicular to the present down-valley gradient, which is assumed to be close to the original gradient at the time of terrace formation (I use the term *down-valley* gradient, which is measured along a straight line, in contrast to the *river-channel* gradient, which is measured along a curved line following a channel thalweg). I assume that the angle between the down-valley gradient and the fault, δ, and the angle between the down-valley gradient and the hanging wall strata, α, are equal. In other words, the fault cuts parallel to the hanging-wall strata, which implies that slip on a fault, s, before and after a bend is equal (Suppe, 1983). The difference in height of a terrace across a fold backlimb (h_1–h_2) and the

fault dip beneath the terrace sections after and before the fault bend (δ_1–α_1 and δ_2–α_2) constrains the amount of fault dip slip (Figure 3.4):

$$s = \frac{h_1 - h_2}{\sin\delta_1 - \sin\delta_2}. \tag{7}$$

The 95% confidence minimum and maximum, and the most probable value of slip rate are calculated using equation 6 and the Monte Carlo simulations described in section 3.4.

A test of the fold model is possible from measurements of the dip of the terrace backlimb, ψ, defined in Figure 3.4, which is predicted by applying fault-bend fold theory to an unconformity:

$$\psi = \arctan\left(\frac{\sin\delta_1 - \sin\delta_2}{\cos\delta_1 + \sin\delta_2 \tan\left(\frac{\alpha_1 + \alpha_2}{2}\right)}\right). \tag{8}$$

In the field, we have observed that the backlimbs of progressively deformed terraces grow by a combination of limb rotation and kink-band migration (for example, the Djuanarik River terraces in section 4.4). I suggest that this is because the axial surfaces have finite widths, possibly due to curved fault bends that adjoin planar fault sections (Figure 3.5). For equation 8 to provide a valid test of the fault-bed fold geometry, total displacement must be greater than the width of the active axial surface. Furthermore, measurements of ψ should be considered minimum values.

The fold-growth analysis also predicts the change in river height since initial floodplain abandonment and terrace formation. Figure 3.4 also shows that the equation for a change in river height relative to the modern river, h_r, is

$$h_r = s^* \sin\alpha_1 - h_1. \tag{9}$$

Calculations from the Djuanarik, Kadjerty, and Alamedin Rivers indicate that h_r, and rates of river aggradation h_r/t, vary through time, and that estimates of slip rate or ages of undated terraces based only on terrace height above the modern river may be significantly in error. Predicted river aggradation rates provide a means of estimating ages of undated terraces, and can help evaluate a result if the predicted aggradation rates can be compared to aggradation rates in

basins measured using a paleomagnetic stratigraphy (e.g., Gould et al., 2000; Weberling et al., 2000).

3.4 Representation and calculation of uncertainties

Monte-Carlo simulations generate uncertainties in slip rate (Chapter 4) and shortening rate (Chapter 5). Ten-thousand calculations sample a variety of probability distributions for each variable (Figure 3.6). Frequency peaks define the most probable slip rate, and the 2.5% and 97.5% tails in the histograms bound the 95% confidence limits. These simulations take into account the standard errors associated with linear regressions of profile data (m, b), errors associated with measuring fault dip (δ), fault location across a scarp ($P(x,y)$), elastic strain accumulated during the earthquake cycle (Δs and Δs_o), and age (t). Because the shape of the probability density function for many of the measured parameters is complicated (e.g., calibrated age distributions of charcoal samples (Stuiver et al., 1998)) or poorly known (e.g., $P(x,y)$), I use several methods to describe uncertainty distributions. Normal distributions describe parameters characterized by a measurable mean and standard error (e.g., m and b). For parameters with either complicated (e.g., t) or otherwise asymmetric uncertainties, I use empirical probability distributions, which I will explain below.

The equations for calculating slip rate assume that strain markers that are offset by a fault, or that mark growth of a fold in a hanging wall, are planar surfaces. For deformed terraces, linear regressions of surveyed points oriented normal to fault strike provide a mean and standard error for m and b that define the strain markers. In trench exposures, linear regressions of points that are digitized from trench logs define mean and standard error of displaced strata.

Fault dip is either calculated by direct measurement, determined by cross-section geometry, or estimated based on geomorphic expression. For instances where the fault surface can be measured directly from natural and artificial exposures with an inclinometer or from a trench log, a "best estimate" and ~95% confidence values are considered to equal a mean and 2σ with a gaussian probability distribution if the uncertainty is symmetric about the best estimate. If uncertainties are asymmetric about a best estimate, the best estimate carries the maximum

probability in a triangular distribution with diminishing probabilities towards the ~95% minimum and maximum values (Humphreys and Weldon, 1994).

In cases for which a fault is not directly exposed, surveying the positions of fault scarps across successive inset terraces allows calculation of planar fault geometry with a probability distribution based on linear regression of surveyed points.

For faults that are blind or buried, and fault slip is manifested by growth of a fold, fault dip is derived from measurements of strata exposed within the hanging wall, based on fault-related fold models of fold growth (section 3.3). The measurements of hanging-wall strata (α, the angle between the strata and the modern river profile) determine the mean and standard deviation of the fault angle (δ, the angle between the fault and the modern river profile).

In cases for which direct measurement of the fault dip was not possible or hanging wall strata were unexposed or ambiguously related to fault orientation, I estimate fault dip based on topographic expression and by analogy with other faults in similar physiographic settings. Faults that appear to dip steeply are represented by a trapezoidal probability distribution, with an equal and maximum likelihood between 30–70°, and probabilities diminishing linearly to zero at 0° and 90° dips. Faults that appear to dip shallowly have a trapezoidal distribution with equal and maximum likelihood between 20–40°, and probabilities diminishing linearly to zero at 0° and 90° dips.

If the position (or projection) of the fault within the fault scarp ($P(x,y)$) is unknown, I use a trapezoidal probability distribution to represent x in equations 2–4 (section 3.2). Based on exposures of thrust faults in our study area and reviews in the literature (Carver and McCalpin, 1996), I give a maximum probability to a fault that projects to 1/3 – 1/2 the distance along the scarp face measured from the base of the fault scarp, and a likelihood diminishing to zero at the top and base of the scarp.

For uncertainties associated with the earthquake cycle, I follow Lavé and Avouac (2000) and consider that some elastically stored slip Δs may be presently stored, and some elastically stored

slip Δs_o may have been stored at the time of terrace formation. In the Monte-Carlo simulations, the values Δs and Δs_o range uniformly between zero and a maximum of 5 m, a value slightly greater than the maximum 4.2 m surface fault slip caused by the 1992 *Ms* 7.3 Suusamyr earthquake (Ghose et al., 1997). In instances where a scarp appears to have formed in a single earthquake, Δs and Δs_o vary between zero and the calculated value of s.

A variety of methods generate probability distributions for the ages of strain markers (terraces or layers in a trench exposure). Because of fluctuations in cosmogenically produced atmospheric ^{14}C through time, radiocarbon ages of organic material that incorporate atmospheric ^{14}C require calibration in order to be compared to the calendric time scale (Stuiver and Reimer, 1986; Stuiver et al., 1998). Calibrated (approximately calendric) radiocarbon dates have complicated probability distributions (Figures 3.6 and 2.3). Although detrital charcoal within a deposit has an inherited age that is older than the age of deposition (section 2.3.1), I assume that this inherited age is small compared to the analytical uncertainty of the radiocarbon age (typically 40–80 ^{14}C yr for our samples, see Table 2.1). In cases where the age of a deposit is constrained by a single radiocarbon sample (e.g., a charcoal sample collected from an offset layer in a trench), the slip-rate calculations sample from the discrete probability distribution of the calibrated radiocarbon age (Figure 3.6). If more than one sample is collected from a deposit, a significance test and geologic judgment determine whether the pooled mean radiocarbon age is calibrated to determine the unit age (Stuiver and Reimer, 1986) (e.g., Table 2.1). In the case of the Kadjerty River QIII(2) terrace, where radiocarbon samples above and below the upper gravel contact constrain the timing of river incision, the slip-rate calculations sample a model age distribution of the gravel contact (section 2.3).

Although the TL and IRSL ages of the QII(2) terraces have large uncertainties (Figure 2.6; Table 2.2), and the samples represent minimum ages, the area of overlap in the probability distributions suggest that the terraces may have formed during a narrow interval of time, similar to the QIII(2) terraces. To evaluate the hypothesis that the sample ages date the same event, I used a significance test that compares measurements with analytical uncertainties (Ward and Wilson, 1978). Each measurement has a preferred age and standard error, $A_i \pm E_i$. The test starts with the determination of the pooled mean age, A_p, whereby

$$A_p = \left(\sum_1^n A_i / E_i^2 \right) \Big/ \left(\sum_1^n 1 / E_i^2 \right) \tag{10}$$

and the test statistic, T, is

$$T = \sum_1^n (A_i - A_p)^2 / E_i^2 \tag{11}$$

which has a chi-squared distribution on n–1 degrees of freedom under the null hypothesis. For the four QII(2) samples, A_p = 140.7 ka, and the test statistic $T = 2.51$, falls below the chi-squared statistic for $n = 4$ ($\chi^2(0.05) = 7.81$), indicating that the four samples are not statistically different. The variance of the pooled age is given by

$$V(A_p) = \left(\sum_1^n 1 / E_i^2 \right)^{-1} \tag{12}$$

and equals 8.5 ka for the four QII(2) samples.

To increase the precision for the slip-rate calculations based on deformed QII(2) terraces, I use the pooled mean age and standard deviation (square root of the variance of the pooled ages) of the statistically similar TL/IRSL analyses (Figure 2.6). In the text of Chapter 4, I report the mean and ~95% confidence interval as 141 ± 17 ka.

For the study sites that lack local age control (e.g., in the southernmost Aksay basin), I use geomorphic criteria and correlation to estimate terrace ages. For terraces mapped as QII(2) or QIII(2), I use the pooled mean age of the terrace determined at other sites. For other terraces I estimate an age distribution based on the stratigraphic relationship between the terrace and other terraces or landforms.

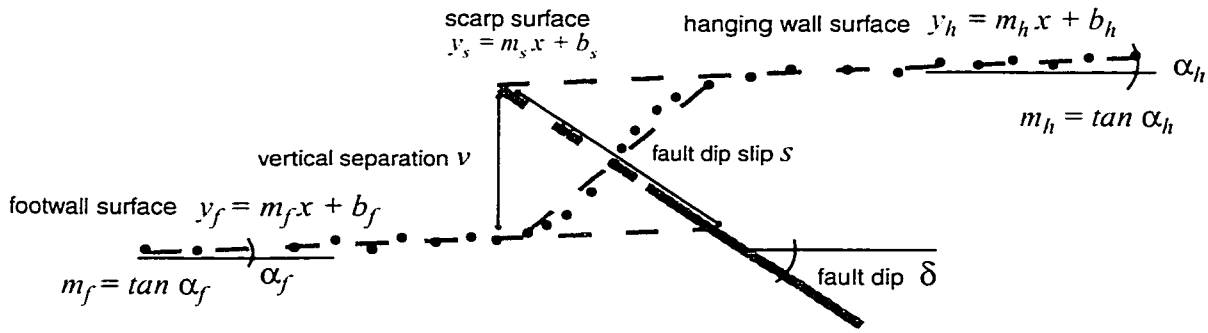

Figure 3.1: Analysis of a faulted river terrace. The figure shows surveyed points along a terrace tread that has been cut by a fault. The dashed thin gray lines indicate the hanging wall, footwall, and scarp surfaces that are represented by linear equations of the form y = mx+b, in a horizontal-vertical reference frame. The thick gray line represents the fault and has a dashed projection up-dip. The scarp face and fault dip, δ, are measured positive in opposite directions. Figure 3.2 explains the calculations for vertical separation and dip slip.

a

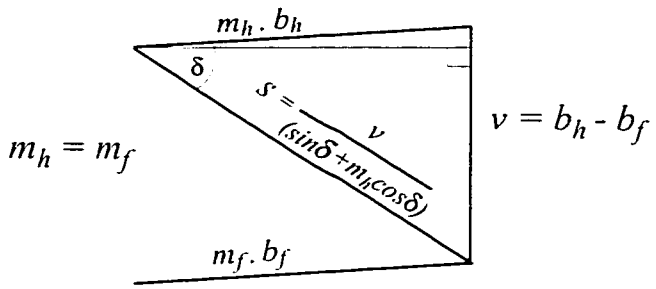

b

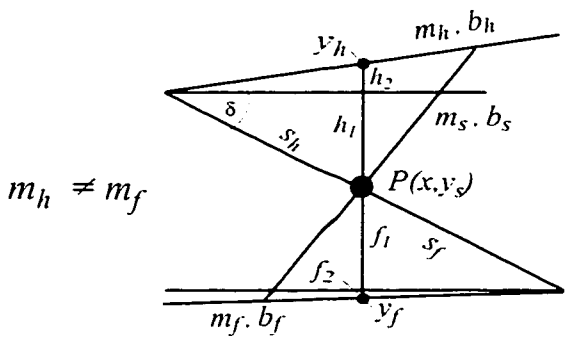

$$v(x) = y_h - y_f = m_h x + b_h - m_f x + b_f$$
$$= x(m_h - m_f) + b_h - b_f$$

$$h = h_1 + h_2 = y_h - y_s$$
$$= x(m_h - m_s) + b_h - b_s$$

$$f = f_1 + f_2 = y_s - y_f$$
$$= x(m_s - m_f) + b_s - b_f$$

$$h_1 = s_h \sin\delta$$
$$h_2 = s_h m_h \cos\delta$$

$$f_1 = s_f \sin\delta$$
$$f_2 = s_f m_f \cos\delta$$

$$x(m_h - m_s) + b_h - b_s$$
$$= s_h \sin\delta + s_h m_h \cos\delta$$

$$x(m_s - m_f) + b_s - b_f$$
$$= s_f \sin\delta + s_f m_f \cos\delta$$

$$s_h = \frac{x(m_h - m_s) + b_h - b_s}{\sin\delta + m_h \cos\delta}$$

$$s_f = \frac{x(m_s - m_f) + b_s - b_f}{\sin\delta + m_f \cos\delta}$$

$$s = s_h + s_f$$

Figure 3.2: Dip-slip calculation for a faulted river terrace. (a) Equations for vertical separation, v, and dip slip, s, for terraces with the same hanging wall and footwall slopes. (b) Equations for vertical separation and dip slip for terraces with different hanging wall and footwall slopes. Fault dip slip, s, depends on the position or projection of the fault within the scarp, $P(x,y)$. s can be expressed as the sum of slip above (s_h) and below (s_f) point P. The components of slip s_h and s_f can be calculated from the lines expressing the hanging wall ($y_h = m_h x + b_h$), footwall ($y_f = m_f x + b_f$) and scarp surface ($y_s = m_s x + b_s$), and the vertical distances from P to lines expressing the hanging wall ($h = h_1 + h_2$) and footwall ($f = f_1 + f_2$).

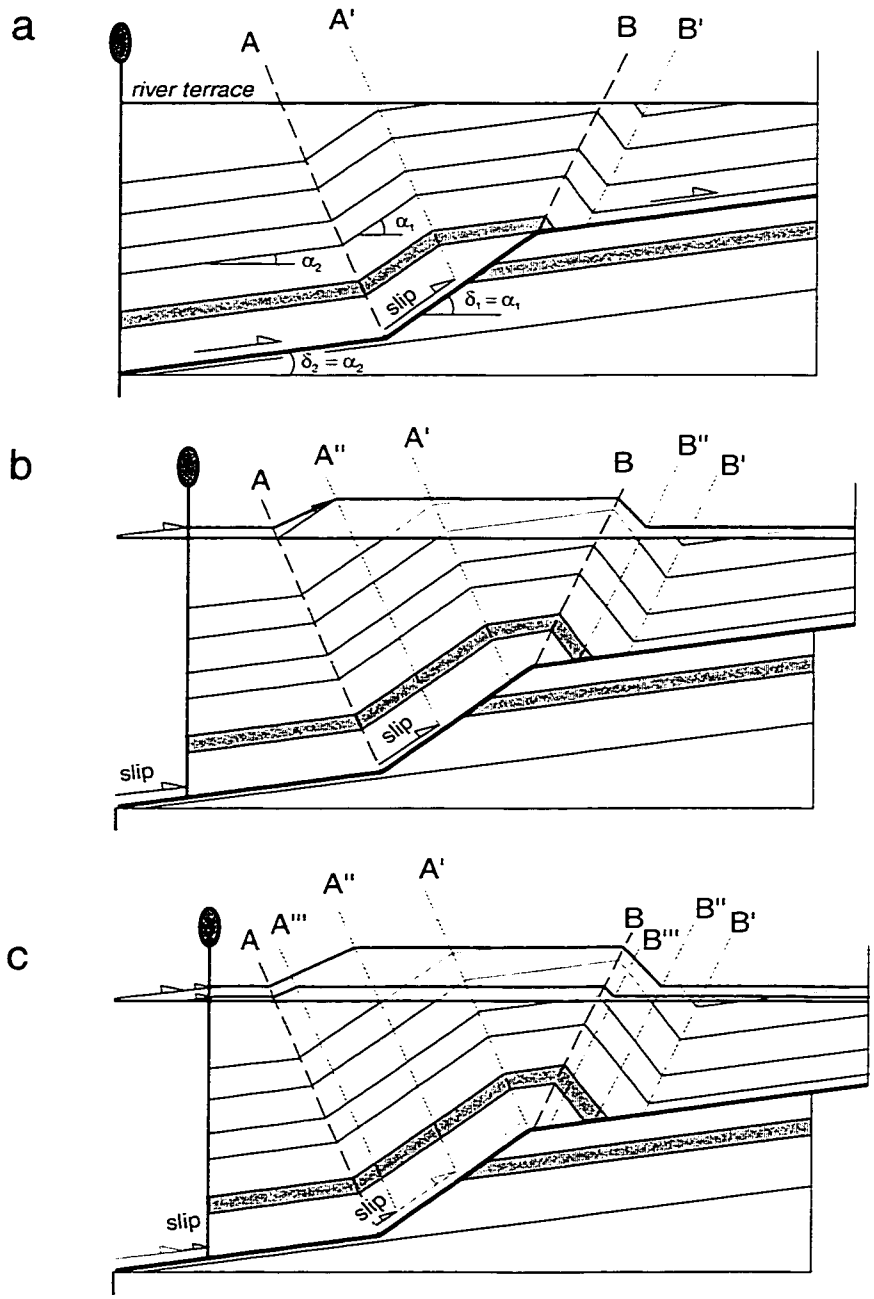

Figure 3.3: Deformation of unconformities in response to idealized fault-bend folding (Suppe, 1983). (a) A horizontal terrace forms across a growing fault-bend fold. Active axial surfaces A and B are fixed to bends in the fault; inactive axial surfaces A' and B' indicate the amount of rock to pass through the active axial surface, indicated by the slip vector. In this example, bedding angles α_1 and α_2 are parallel to the fault dips δ_1 and δ_2 in the backlimb. (b) Deformation of the terrace in response to an increment of fault-bend folding. New inactive axial surfaces A" and B" at the bends in the terrace indicate the amount of fault slip since formation of the river terrace. Note that this axial surface is not visible in the underlying strata. Lower horizontal line indicates formation of another, inset river terrace. (c) Continued fault-bend fold deformation. Notice the terrace fold limbs are parallel but have different lengths, indicating the different amounts of displacement on the underlying fault.

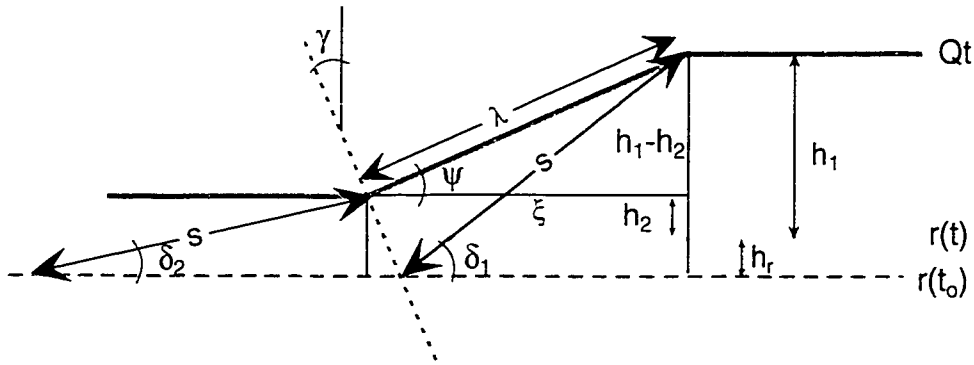

- s dip-slip displacement, m.
- δ_1, δ_2 angle between modern river and fault above and below the fault bend, degrees.
- α_1, α_2 angle between modern river and strata, degrees.
- h_1, h_2 height of terrace above river, m.
- γ orientation of axial surface computed by $\gamma = (\alpha_1 + \alpha_2)/2$
- ψ angle of the backlimb, degrees.
- λ length of the backlimb of the folded terrace: $\lambda = (h_1 - h_2) / \sin \psi$
- $r(t)$, $r(t_o)$ profile of modern river and river at time of terrace formation, t_o
- h_r change in height of river since initial terrace formation t_o, m.

$$s = \frac{(h_1+h_r)}{\sin \delta_1} = \frac{(h_2+h_r)}{\sin \delta_2}$$

$$s = \frac{h_1-h_2}{\sin \delta_1 - \sin \delta_2} \qquad (7)$$

$$\psi = \arctan\left[(h_1-h_2)/\xi\right]$$

$$h_1-h_2 = s(\sin \delta_1 - \sin \delta_2)$$

$$\xi = s \cos \delta_1 + (h_2+h_r) \tan \gamma;$$

$$h_2+h_r = s \sin \delta_2$$

$$\gamma = (\alpha_1 + \alpha_2)/2$$

$$\psi = \arctan\left[\frac{\sin \delta_1 - \sin \delta_2}{\cos \delta_1 + \sin \delta_2 \tan((\alpha_1 + \alpha_2)/2)}\right] \qquad (8)$$

$$h_r + h_1 = s \sin \delta_1$$

$$h_r = s \sin \delta_1 - h_1 \qquad (9)$$

Figure 3.4: Schematic illustration of terrace deformation predicted by fault-bend fold theory. Terrace Qt has been deformed as a result of a constant magnitude of slip, s, occuring across a fault that steepens from a dip δ_2 to δ_1 across an angular bend. The profile of the river terrace at its time of formation, $r(t_o)$, is indicated by the dashed line. This figure indicates a relative rise in river level since the time of terrace formation. Equation 7 shows the calculation of displacement from the change in terrace height across the fault bend and the dips of the underlying fault. Equation 8 is the relationship between the angle of the backlimb of the terrace, ψ, and the fault dips δ_1 and δ_2. Equation 9 is used to calculate the amount of relative vertical change of the river, h_r, since the terrace was formed.

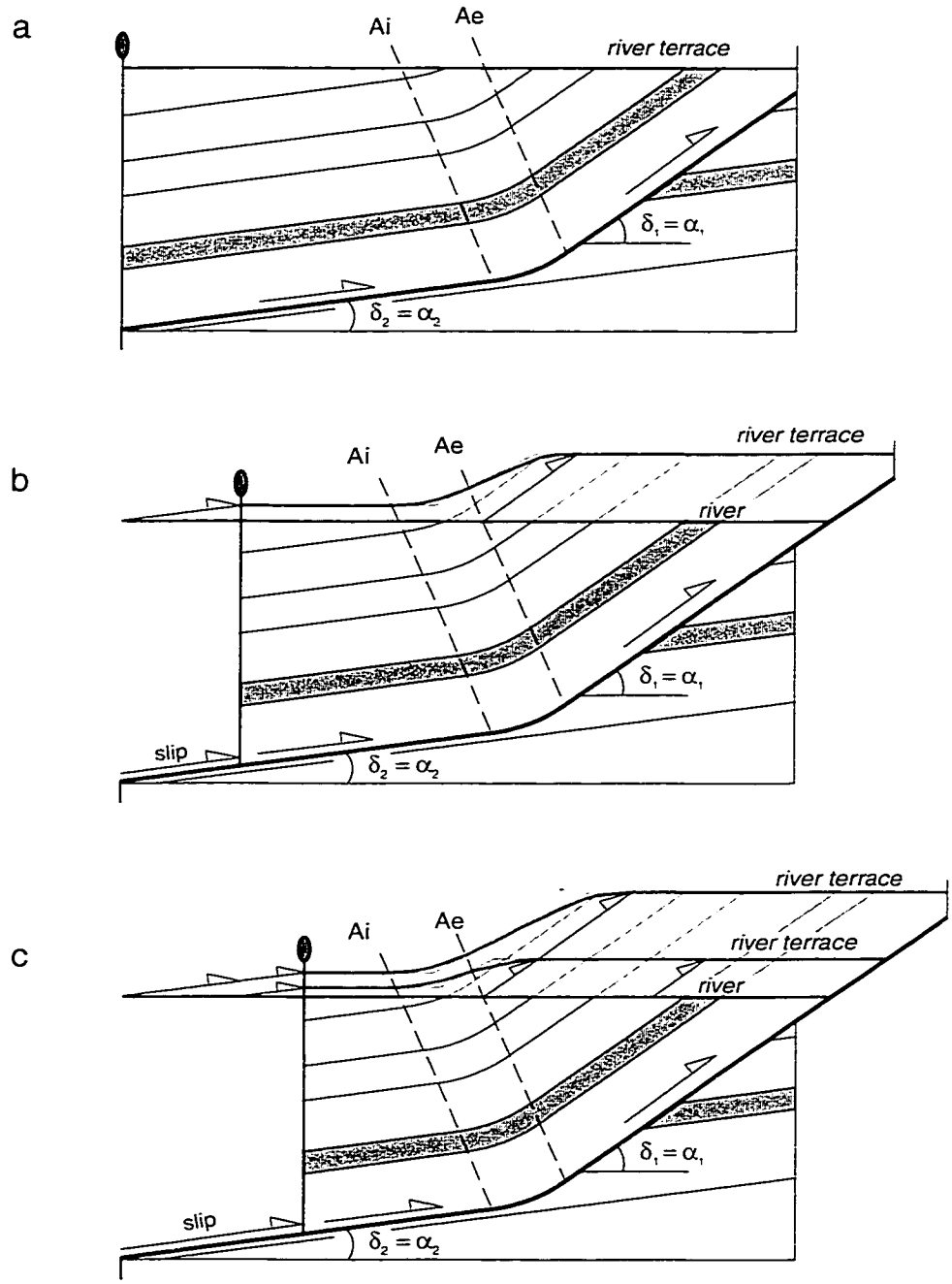

Figure 3.5: Progressive deformation of unconformities in response to displacement across a curved fault bend. Material passes through entry (Ai) and exit (Ae) axial surfaces that are fixed to the fault (Suppe et al., 1997). (a) Black horizontal line indicates a newly formed river terrace. (b) Terrace deformed by an amount of slip. Grey line beneath the black terrace shows the predicted deformation for a perfectly angular fault bend and axial surface. (c) Nested terraces deformed by continued fault slip. Notice the prediction for both progressive limb rotation and kink-band migration shown. Unlike the angular fault bend example in Figure 3.3, the lengths and angles of the back limbs for small amounts of slip do not represent the fault displacement and underlying fault dip.

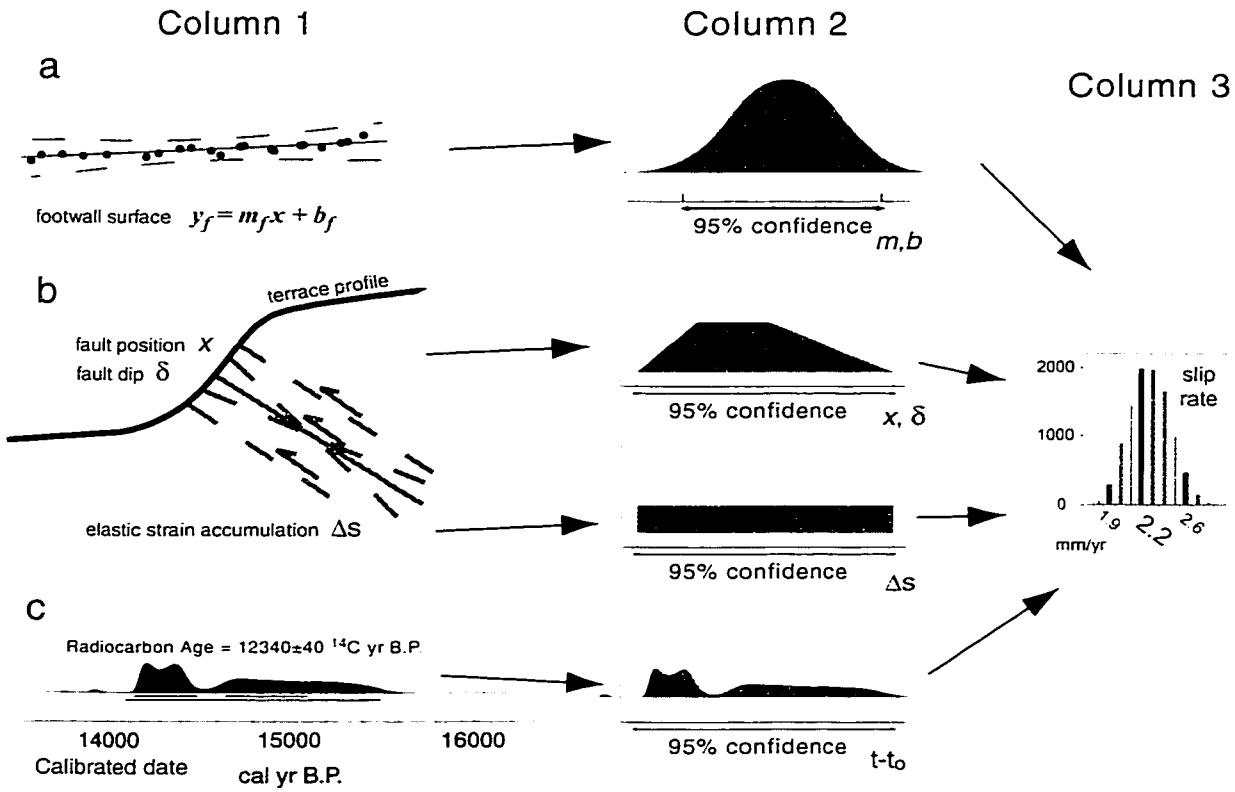

Figure 3.6: Calculation of uncertainties from measurements of slip-rate variables. Column 1 indicates measurements made in the field or laboratory, and Column 2 shows the probability representations of the different variables that go into the Monte Carlo simulation. (a) Linear regression of survey points on a terrace represents a hanging wall or footwall. Solid line indicates least-squares fit and dashed curved lines represent 95% confidence ranges given standard errors in slope, *m*, and intercept, *b*. (b) Measurements or constrains on the dip, δ, and location of a fault projecting onto a scarp, *x*, are represented by normal, uniform, or discrete distributions. A trapezoidal distribution is shown here. Elastic strain accumulation, Δs, is represented by a uniform distribution. (c) Calibration of a radiocarbon age, showing probability density of calibrated ages. The probability density of the calibrated age is represented in the error analysis if the offset unit is constrained by one radiocarbon age. Column 3 shows an example of a histogram of slip rate. The slip-rate numbers that correspond to black histogram bars are midpoints for bins, and indicate the most probable value and 95% confidence limits.

Chapter 4

Late Quaternary slip rates

This chapter presents the slip-rate determinations of the most active fault (or faults) in each of five basins (Figure 1.3). All these fault zones show signs of Holocene activity, and of multiple slip events since ~140 ka. Unless specified otherwise, all uncertainties represent the 2σ or 95% confidence interval.

4.1 Issyk-Ata fault, Chu basin

The Issyk-Ata fault defines the northern deformation front for the central Tien Shan between ~74° and ~75° E longitude (Figures 1.2 and 4.1a), and extends at least 120 km from the Aksu River east to its surface termination near the Shamsi River (Abdrakhmatov, 1988). As a moderately south-dipping thrust to reverse fault at the surface, the Issyk-Ata fault places Neogene sandstone and siltstone over Quaternary gravel. The Issyk-Ata fault merges at its western terminus with the Chonkurchak fault, which marks the boundary between pre-Cenozoic basement at the Kyrgyz Range front and late Cenozoic deposits in the western Chu basin (Figure 4.1a). Farther east, between the Ala-Archa and Alamedin Rivers, the Chonkurchak fault steps north and its eastward continuation is called the Shamsi-Tunduk fault. Late Pleistocene terraces near the Alamedin River are folded along portions of the Shamsi-Tunduk fault, although the amplitude of folding indicates minor late Quaternary surface shortening compared with the folded and faulted terraces above the Issyk-Ata fault. I interpret the Issyk-Ata fault as a splay from the Shamsi-Tunduk / Chonkurchak fault beneath the southern margin of the Chu basin. I estimated a slip rate for the Issyk-Ata fault at two locations: on its central portion, where it crosses the Alamedin River (Figure 4.1b), and on its western portion, where it crosses the Sokuluk River (Figure 4.1c).

4.1.1 Alamedin River site

Nested river terraces can be traced along the Alamedin River for about 12 km from within the Kyrgyz Range front to the Issyk-Ata fault, just south of Bishkek (Figure 4.1b). Starting about 5

km south of the Issyk-Ata fault, between the Alamedin and Ala-Archa Rivers, river terraces cover a prominent row of hills underlain by south-dipping Neogene strata (Figures 4.1b and 4.2) (Chediya, 1986; Abdrakhmatov, 1988). Terrace risers along the Alamedin River provide a continuous exposure of Neogene sedimentary rock dipping nearly uniformly at ~34 ± 2° S beneath the uplifted terrace section (Figures 4.2a and 4.3). We did not find Neogene strata outcropping south of the elevated portion of the terrace. North of the Issyk-Ata fault, in the footwall, coalescing alluvial fans show that the Alamedin River is aggrading there.

A profile of the contact between a thin layer of fluvial gravel (deposited on the Tertiary bedrock strath) and overlying fine-grained sediments for the QII(2) terrace shows a back-tilted section along the southern edge, particularly if rotated to remove the ~1.7° modern river gradient (Figure 4.3). The back-tilted segment, which I interpret as a growing backlimb of a fault-bend fold, rises to 103 ± 1 m for 1.7 km approximately parallel to the modern river profile. The top of the backlimb and the northern end, close to the fault, are higher. This variation in height could be due to steep faults or fault-related folding that we did not detect in our mapping of Neogene strata, or it could mean that an older terrace, ~125 m above modern river level, was inset by a terrace ~103 m above modern river level. The silt on top of the terrace gravel and bedrock strath, up to 30 m thick, obscures the variation in height of the gravel contact in distant views of the terrace (Figure 4.2).

I analyzed the QII(2) terrace deformation using simple fault-bend fold models of structural growth (Section 3.3). To test the geometry and kinematics of a structural interpretation, I compared the terrace profile to predictions of the deformation of a flat unconformity (river terrace) due to slip on an inferred fault (Figures 3.3 and 3.4).

A lack of structural data south of the high section of the QII(2) terrace along the Alamedin River hinders analysis of fold growth. A more complete analysis of fold growth is possible for the Akchop Hills fault in Kochkor basin, described below. Nevertheless, the amount of fault slip may be calculated from the difference in heights of the QII(2) terrace across the fold backlimb (h_1–h_2), from ψ, the angle between the slope of the terrace backlimb and the stream gradient, and

from δ_1, the angle between the fault and the stream gradient, which is assumed to be equivalent to the angle between the bedding and the stream, α_1 (section 3.3, Figure 3.3).

The ~36 ± 2° difference between the dips of Tertiary strata under the elevated terrace and the present gradient of the river provides δ_1. To estimate δ_2 (the angle of the fault south of the backlimb), I searched equation 8 iteratively for values consistent with measurements of δ_1 and ψ. A line fit to three surveyed points that define the QII(2) terrace backlimb makes an angle of ψ = 9.5 ± 1.5° S with the surface, but one pair of these points yields 17° (Figure 4.3). Because most violations of the ideal fault-bend-fold geometry will reduce measured values of ψ (e.g., Figure 3.5), I use a range of backlimb angles of ψ = 8–17° S in the error analysis. The change in height of the terrace across the backlimb of the fold, h_1–h_2, is given by the difference between the height of the flat middle section of the uplifted terrace, h_1 (103 ± 1 m), and the height of a point surveyed south of the growing backlimb (with an assigned uncertainty twice the value of the measured one), h_2 (24 ± 2 m).

An IRSL age of 170 ± 50 ka gives a limiting minimum age of the QII(2) terrace along the Alamedin River (Figure 2.6 and Table 2.2). The IRSL age was measured on silt sampled from ~2.5 m above an exposed contact between river gravel and ~30 m of overlying fine-grained material (Figures 2.6c and 4.2). The fine-grained deposit is mostly loess, although overbank sediment may be preserved or mixed with loess near the base of the sediment. To improve precision, I use the pooled age of 141 ± 17 ka for the QII(2) terrace in the calculation (section 3.4).

Solving equation 8 for δ_2 yields a value for fault dip south of the fold of 18 ± 6° S, and equation 7 yields 290 +230/–20 m of fault slip. The slip rate on the Issyk-Ata fault at the Alamedin River is calculated to be 2.1 +1.7/–0.3 mm/yr (Figure 4.3).

Equation 9 predicts that the modern Alamedin River has risen 53 +128/–17 m since QII(2) formation, which corresponds to a minimum footwall aggradation rate of 0.5 +1.0/–0.1 mm/yr. This rate is consistent with the 0.5–1.5 mm/yr aggradation rate of Plio-Pleistocene gravel

measured near the Noruz River, about 15 km east of the Alamedin River (Figure 4.1) (Bullen et al., in press).

4.1.2 Sokuluk River site

A single, sharply defined scarp trending N64°E marks the Issyk-Ata fault across a broad fan in the Sokuluk River valley (Figures 4.1c and 4.4). Ignatiev (1886) reported a 1–2 meter-high scarp along this section of the fault that he associated with the Byelovoda earthquake of 1885. In Chapter 6, I discuss paleoseismic results from a trench and profiles along the faulted QIII(2) fan and inset terraces. In this section, I limit discussion to the Issyk-Ata fault slip rate, using profiles of the QIII(2) fan across the scarp and fault-dip information from the trench.

Profiles of the faulted QIII(2) fan surface show a vertical separation of 6.3 +0.1/–0.2 m (Figure 4.4). The trench wall exposes a single fault trace dipping 25–26°S that places gently folded alluvial gravel in the hanging wall over a series of fine-grained colluvial and gravelly alluvial units in the footwall (Chapter 6; Figure 6.4). Alluvium and colluvium overlying original fan gravel in the footwall is ~0.6 m thicker than the fine-grained sediment overlying the fan gravel contact in the hanging wall (Chapter 6). I assume that the difference in thickness diminishes away from the footwall, so that the vertical separation across the scarp determined from a long profile represents total fault displacement (Figure 4.4). The flat surface of the QIII(2) fan in the hanging wall, shown by the long profile measured adjacent to the trench, indicates an underlying planar fault (e.g., Arrowsmith and Strecker, 1999). The dips of imbricated gravel beds measured in the trench within the hanging wall range from about 3° to about 15° adjacent to the fault (Figure 6.4). Because the fault is planar in the trench exposure, this folding probably reflects drag folding of the hanging wall and is not related to a fault bend. I cannot preclude, however, that the difference between the ~3°S dip of gravel beds measured in the hanging wall in the trench and the 1.6° dip of the fan surface is due to a change in fault dip beneath our trench exposure. This change in dip would occur below the rounded top of the fault scarp and would not be detectable in the long profiles. Fault-bend fold theory predicts that the ~1.5° dip change corresponds to a ~1° increase in fault dip. I incorporate this possibility in the fault dip estimate of 26 ± 2°.

Radiocarbon ages of snail shells and an IRSL age of silt capping the fan on the hanging wall provide minimum limiting ages of the QIII(2) surface near the Sokuluk River (Chapter 6). Although the calibrated radiocarbon age of the oldest shell (14.4–15.8 x 10^3 cal yr B.P.) is consistent with the ~13.5–15.7 x 10^3 cal yr B.P. age of QIII(2) terrace formation dated elsewhere, the shells do not show stratigraphic consistency. Also, an IRSL age of silt from the fine-grained sediments in the hanging wall of the trench is 21.6 ± 0.9 ka (Table 6.2), which is ~6–8 thousand years older than the radiocarbon ages. I discuss potential problems with the radiocarbon and IRSL ages in Chapter 6, and for the slip-rate calculation consider two possibilities. The first accepts the IRSL age as the true age of the fan. The second assumes that the shell and IRSL ages overestimate the true date of fan formation, and that the combined ~13.5–15.7 x 10^3 cal yr B.P. age of the QIII(2) surface is correct.

The parameters discussed above and inserted into equations 1–5 yield a slip rate of 0.6 ± 0.2 mm/yr using a 21.6 ka age and 0.9 ± 0.3 mm/yr using a 13.5–15.7 x 10^3 cal yr B.P. age (Figure 4.4). This rate is less than half the slip rate of the Issyk-Ata fault calculated at the Alamedin River, 35 km east. An increase in shortening rate from the west end of the Kyrgyz range to the central portion of the Kyrgyz Range is consistent with a component of anti-clockwise rotation seen in the GPS geodesy data (B. Meade, personal communication, 2000). Nevertheless, I hope that more detailed mapping and profiling of the QIII(2) terrace near the Alamedin River improves the slip-rate calculation there.

4.2 Akchop Hills and South Kochkor faults, Kochkor Basin

Active faults and folds deform the southern margin of the Kochkor basin, an east-west-trending intermontane basin south of the Kyrgyz Range (Figures 1.2 and 4.5). The South Kochkor fault follows the southern margin of the basin, placing Paleozoic metamorphic and igneous rock of the Terskey Ala-Too over weakly cemented Neogene sedimentary rocks (Fedorovich, 1935; Schulz, 1948; Tarasov, 1970; Sadybakasov, 1972). Although this fault and proximal splays cut late Quaternary river terraces and alluvial fans, most of the late Quaternary surface deformation occurs several kilometers to the north, within the basin, where it is expressed by a band of hills of folded Miocene to Pliocene Djuanarik Formation sandstone and

siltstone (Figure 4.5b). Erosion and deposition by the Djuanarik River, which flows northward across the southern margin of Kochkor basin, has produced multiple, nested river terraces that are progressively deformed across the growing Akchop Hills (Fedorovich, 1935) (Figure 4.6). We surveyed profiles along five river terraces and mapped the underlying strata on the west side of the Djuanarik River to evaluate the subsurface geometry and rates of slip on faults along the southern margin of Kochkor basin (Figures 4.5b and 4.7). The presence of an abrupt topographic front at the northern edge of the Akchop hills and the south-dipping strata underlying the hills indicate that the Akchop Hills overlie a south-dipping thrust fault (the Akchop Hills fault). I interpret the gently dipping Akchop Hills fault to connect south of the range front with the South Kochkor fault.

I have calculated slip rates for both faults from measurements of the deformed QII(2) terrace; and will start with the faster-slipping Akchop Hills fault.

4.2.1 Akchop Hills fault

Profiles of three river terraces along the west side of the Djuanarik River, rotated to remove the ~0.7° modern river gradient, show progressive vertical movement and development of back-tilted sections (Figure 4.7). Because the structure resembles a kink fold, fault-bend fold theory can predict the geometry and kinematics of fault slip at depth (section 3.3). Two synclinal axial surfaces in the Neogene stratigraphy in the back limb of the fold (Figure 4.5b) also mark bends in the QII(2) and QIII(1) river terraces (Figures 4.6 and 4.7a), indicating that the axial surfaces are presently active.

I infer that the southern synclinal bend (axial surface (i)) results from fault-bend folding above a thrust ramp that steepens from $\delta_2 = 9 \pm 2°$ S to $\delta_1 = 18 \pm 2°$ S (Figure 4.7b). The thrust fault geometry is supported by the agreement between the predicted backlimb angle (9 +4/–5°, from equation 8) and the measured backlimb angle (9°) (Figure 4.7b). The dip information and the difference in height of the QII(2) terrace across axial surface (i), inserted into equation 7, give the amount of fault slip (section 3.3).

TL and IRSL analyses of massive silt from the base of a ~4 m thick deposit overlying the fluvial gravel of the QII(2) terrace yielded an age of 128 ± 26 ka since last exposure to light and/or heat (Table 2.2 and Figures 2.5 and 4.6). In the slip-rate calculation, I use the pooled age of the four QII(2) terraces, 141 ± 17 ka, as the age of terrace formation (section 3.4). The dip-slip rate, using parameters described above and inserted into equations 7 and 6, is 2.9 +1.6/–0.7 mm/yr (Figure 4.7c).

4.2.2 South Kochkor fault

The offset QII(2) terrace at the range front provides data to calculate a slip rate for the South Kochkor fault (Figures 4.5 and 4.8). A profile of the QII(2) terrace across the fault extends 2.5 km south of the range front and a similar distance north. This profile has an abrupt bend (axial surface (iii) in Figure 4.5b) and a back-tilted section beginning ~600 m south of the fault (Figures 4.8b and c). Within ~100 m of the fault, the gravel contact of the QII(2) terrace folds into an anticline next to the fault scarp. In the footwall, the QII(2) terrace and the inset QIII(1) terrace tilt to the south for a distance of ~1 km. I interpret the back-tilting of the terrace in the hanging wall to be the result of rotation by a curved fault. The footwall tilt is due to either footwall fault-related folding of the South Kochkor fault or a gradual change in dip of the Akchop Hills fault underlying the terraces.

The 26 ± 3 m difference in height between six surveyed points in the hanging wall and one surveyed point in the footwall that is closest to the fault scarp provide data to calculate a slip rate. The active trace of the South Kochkor fault is not exposed at the range front. An older trace exposed in the hanging wall dips ~45°S and juxtaposes granite against Neogene sandstone (Sadybakasov, 1972). Based on the map pattern of the fault, which suggests a moderate to steep dip, the dip is represented by a trapezoidal probability distribution with a maximum likelihood of 30–70°S (section 3.4). The slip rate of the South Kochkor fault is 0.2 +0.9/–0.03 mm/yr (Figure 4.8d).

4.3 Kadjerty and Central Naryn faults, Naryn basin

The Naryn Valley, which occupies one of the largest intermontane basins in the Kyrgyz Tien Shan, contains abundant evidence for Quaternary shortening (Schulz, 1948; Makarov, 1977; Sadybakasov, 1990; Burbank et al., 1999). The Akchatash fault and associated folds separate the northern margin of Naryn basin from the Moldo-Too Range (Makarov, 1977) (Figures 4.9 and 2.2b). In several locations the Akchatash fault cuts a Plio-Pleistocene conglomerate, but in others the basin boundary is marked by monoclinal folding of the pre-orogenic erosion surface and by an unconformable contact between pre-Cenozoic "basement" and Cenozoic strata. The monoclinal folding at the basin margin may indicate a transfer of fault slip from a north-dipping crustal ramp underlying the Moldo-Too to the gently north-dipping Kadjerty and Central Naryn faults that penetrate the northern Naryn basin. Late Quaternary terraces that cross the boundary between basin and range do not seem deformed.

Much of the late Quaternary shortening across the northern and eastern Naryn basin occurs by slip on the Central Naryn and Kadjerty faults (Figures 1.2 and 4.9). Anticlinal folding and the preservation of hanging-wall cut-offs mapped along the fault traces indicate that total displacement on either fault is less than a few kilometers (Figure 4.9b). I calculated late Quaternary slip rates for the Kadjerty and Central Naryn faults along the south flowing Kadjerty River, a tributary to the west-flowing Naryn River. I also calculated a slip rate for the Kadjerty fault 50 km west, where it crosses the Kurtka River.

4.3.1 Kadjerty fault, Kadjerty River site

On the east side of the Kadjerty River, the Kadjerty fault cuts as many as five terrace levels by progressively greater amounts. The lowest of these terraces—a QIV(4) terrace—adjoins to the modern floodplain, while the highest of these—a QII(2) terrace—marks the divide with the adjacent drainage (Figures 4.9 and 4.10). Profiles across the fault scarp that crosses the broad QIII(2) terrace east of the Kadjerty River show vertical separations that increase from ~8 m at the east end to ~12 m near the west edge of the tread. A profile at the west end of the terrace tread provides data to calculate the slip rate of the Kadjerty fault (Figure 4.10). Because the fault plane is not exposed in either valley wall of the Kadjerty River, I determined the fault dip from

measurements of the scarp locations on the QIII(2) terrace and on the adjacent QIV(2) terrace (Figure 4.10a). Using the average trend of the QIII(2) terrace scarp (N66°E) and the QIV(2) terrace scarp (N71°E) to constrain the strike of the fault, the fault dips 29 ± 5°N at the QIII(2)/QIV(2) terrace riser. The uncertainty in the dip incorporates the 5° difference in strike above and below the riser and the uncertainties in locating the fault within the scarps on the upper and lower terrace surfaces. Because the fault dip was determined from local offset terraces, I use surveyed points close to the fault scarp to calculate slip rate (Figure 4.10c). Changes in the height and slope of the terrace above and below the surveyed points are probably due to fault-related folding. The decrease in the height of the terrace above the river at the north end of the profile is consistent with a fault dip decreasing from 29°N at the surface to ~10°N beneath the north end of the profile (Figure 10c). Along strike, the decrease in vertical separation across the fault scarp from ~12 m to ~8 m is consistent with a fault dip that decreases from 29°N at the west end of the terrace tread to ~19°N at the east end of the terrace tread, at the base of the riser to the QII(2) terrace.

Three radiocarbon analyses on detrital charcoal constrain the timing of river incision, floodplain abandonment, and formation of the QIII(2) terrace along the Kadjerty River (section 2.3.1; Table 2.1). The three samples together give a 13.7–15.3 x 10^3 cal yr B.P. age range for the QIII(2) terrace gravel contact (Figure 2.3b). Using the parameters outlined above, equations 3–6 yield a slip rate of 1.8 ± 0.4 mm/yr (Figure 4.10c). The vertical separation of the ~141 ka QII(2) terrace is 65–90 m (Figure 4.10a). Given the estimated ~19°N dip of the fault near the riser between the QIII(2) and QII(2) terraces, the displacement of the QII(2) terrace yields a slip rate of ~1.4–2.0 mm/yr, similar to the QIII(2) terrace slip rate.

4.3.2 Kadjerty fault, Kurtka River site

The Kadjerty fault offsets the broad QIII(2) terrace and other inset terraces at the Kurtka River in north-central Naryn basin (Figure 4.9). On the west side of the river, the scarp trends ~N89°E across the QIII(2) terrace tread to the valley wall. East of the river, the scarp diminishes in height to the valley wall, and the buried continuation of the fault is indicated by a prominent topographic front that coincides with a synclinal axial surface. Although we have not mapped

the fault between the Kurtka River and the Kadjerty River 50 km east, I infer that it is the same fault based on its similar distance (~7 km) south of the Moldo-Too Range front, and the similar amount of total shortening indicated by mapped Tertiary strata in the hanging wall of the fault.

A profile of the contact between gravel and fine-grained sediments on the QIII(2) terrace west of the Kurtka River shows a vertical separation of 6 ± 3 m (Figure 4.11). Two locations of the fault surveyed along the west riverbank constrain the fault dip. The scarp on the QIII(2) terrace clearly constrains the fault position at the top of the riverbank. Within the riverbank, the fault must lie north of flat-lying layers of Quaternary gravel that outcrop below the QIII(2) scarp, indicating that the fault must dip less than 40°N. A 2 m, north-side up difference in the elevation of an inset strath terrace may indicate the fault location (Figure 4.11), which would imply a dip of 20 ± 5°N. Although the river may have cut the straths at different times in the Holocene, numerous springs and small landslides suggest that displacement of the Kadjerty fault caused the change in strath height.

Two charcoal samples collected from the same outcrop ~5–10 cm above the gravel contact of the QIII(3) terrace on the east side of the river have statistically similar radiocarbon ages (Figure 4.11 and Table 2.1). The calibrated age of the pooled radiocarbon age is 13.8–15.4 x 10^3 cal yr B.P. (Table 2.1). Profiles of the QIII(2) and QIII(3) terraces on the east side of the river show similar vertical separations, indicating that they were displaced during the same earthquakes. Because of this observation, and because the QIII(3) age is similar to the calibrated radiocarbon ages collected from the QIII(2) terrace at the Kadjerty River (Figure 2.3), I infer that the formation of the inset QIII(3) terrace closely approximates the timing of incision and abandonment of the QIII(2) terrace at the Kurtka River (section 2.3).

The mean vertical separation of the fault scarp on the west side of the river, the 20 ± 5° dip of the fault, and the minimum terrace age of 13.8–15.4 x 10^3 cal yr B.P. inserted into equations 3–6 yields a slip rate of 1.2 +0.8/–0.7 mm/yr (Figure 4.11). There was no clear indication of the fault position within the east bank of the river, but a ~13° dip is permissible. This dip and the ~4 m vertical separation of the QIII(2) and QIII(3) terraces east of the river results in a similar slip rate.

The ~1.2 mm/yr slip rate is comparable to the rate measured for the fault at the Kadjerty River, 50 km west.

4.3.3 Central Naryn fault

Two splays of the Central Naryn fault that cut QIII terraces west of the Kadjerty River merge into a single fault trace near the west river bank (Figure 4.9), where the Central Naryn fault dips 37 ± 2° N in a ~40 m-high exposure (Figure 4.12). A profile of the top of fluvial gravel on the QIII(2) terrace shows a small anticline near the fault scarp and an abrupt bend ~750 m north of the scarp. North of the bend, the terrace slopes 0.9° S, as does the floodplain of the modern river (Figure 4.12). South of the bend, the sub-horizontal terrace surface indicates a back-rotation caused by changes in underlying fault dip. The change in terrace height, with the assumption of constant fault dip and the recognized ~37°N dip at the surface, is consistent with a fault dip of ~12° N at depth.

The vertical separation of the QIII(2) terrace, using points surveyed close to the scarp, is 20.6 ± 1.0 m (Figure 4.12). A point surveyed on the fault plane constrains the location of the fault (point P in section 3.2). Given the known fault location, the 37 ± 2° dip, and the age distribution described in section 2.3.1, the rate of dip slip for the Central Naryn fault is calculated to be 2.3 +0.3/–0.4 mm/yr (Figure 4.12).

4.4 Oinak-Djar fault, At-Bashi basin

The south-vergent Oinak-Djar fault ("Quaternary fault" of Makarov (1977)) apparently accommodates most of the late Quaternary shortening across the western and central At-Bashi basin (Figures 1.2 and 4.13). For most of its 80-km strike length, the fault separates hills composed of steeply dipping Tertiary sediments and late Quaternary fans (Figure 4.13). Although for ~35 km a well-defined scarp indicates that the Oinak-Djar fault reaches the ground surface, the thrust fault is concealed along its eastern portion, where slip is transferred into a fault-propagation fold. Right-stepping en-echelon fold axes in the hanging wall of the fault and deflected drainages indicate a minor component of left-lateral shear (Makarov, 1977) (Figure 4.13).

We excavated a 20-m-long trench across the Oinak-Djar fault where the fault has offset the head of an alluvial fan repeatedly during the late Quaternary Period (Figures 4.13 and 4.14). I limit the discussion in this section to estimations of slip rate; details of the trench-wall stratigraphy and evidence for paleoearthquakes appear in Chapter 6.

Two deposits that extend across the fault zone provide data to calculate slip rate (Figure 4.14). The older of these (unit 20 in Figures 4.14 and 6.7) is the lower of two layers of silty sand interstratified with coarse sand and fine gravel alluvium, while the younger (unit 60 in Figures 4.14 and 6.7) contains sandy and pebbly alluvium with a laminated silt layer at its base. In order to restore the anticlinal folding of units 20 and 60 in the hanging wall, the contacts projected into the fault zone dip 8.4°S, similar to the terrace surface immediately north of the trench (Figure 4.14). Vertical separations of layers 20 and 60 are 4.2 +0.5/–0.3 m and 4.0 +0.4/–0.3 m, respectively. Radiocarbon ages of detrital charcoal fragments indicate that unit 20 was deposited ~9.6–10.5 x 10^3 cal yr B.P. and the laminar silt at the base of unit 60 was deposited ~9.0–9.3 x 10^3 cal yr B.P. (Figure 6.7 and Table 6.1). This yields a slip rate of 0.9 ± 0.4 mm/yr for unit 20 and a 0.9 +0.5/–0.4 mm/yr slip rate for unit 60. The pooled slip rate is 0.9 ± 0.3 mm/yr for the Oinak-Djar fault (Figure 4.14).

4.5 North and South Kyrkungey faults, Aksay basin

Only two faults appear to have significant late Quaternary slip rates in the eastern Aksay basin. The North and South Kyrkungey faults are part of a ~40 km-long system of folded hills that trends about 10 km southeast of and parallel to the southeastern At-Bashi Range front (Makarov, 1977) (Figures 1.2 and 4.5). Our reconnaissance suggests that this fault system within the Aksay basin is more active than the North Aksay fault that defines the northern margin of the basin. Moraines, formed during the last glacial period, are offset less than one meter along the North Aksay fault. Inset, younger moraines do not appear displaced. The North and South Kyrkungey faults cut alluvial terraces downstream of the range front, and show abrupt fault scarps and offset gullies in several locations. Both the North and South Kyrkungey faults dip south, in a direction opposite of the North Aksay fault that marks the southern boundary of the At-Bashi Range. Perhaps the south-dipping faults form a structural wedge (Narr and Suppe, 1994) that extends into basement rock and connects to the north-dipping North Aksay fault at

depth. We know little about the Kyrkungey faults because we spent little time on them and because late Cenozoic strata are poorly exposed. Despite the imprecision, the estimated slip rates of these faults are low compared to those discussed above.

4.5.1 North Kyrkungey fault

The North Kyrkungey fault displaces the heads of small Holocene fans and terraces southeast-side up between the Djolbogoshtu and Kashkasu rivers (Figures 4.15 and 4.16). Elsewhere along the fault trace, evidence for recent surface faulting is absent or unclear; either the fault does not reach the surface in all locations, or it consists of several short segments. An aligned row of folds to the northeast, however, shows that late Quaternary deformation continues along strike. With a hand level, we measured a scarp 1 ± 0.5 m high across a low terrace ~2 m above the Kashkasu River at bank-full (Figures 4.16b,c). The age of the terrace and the dip of the fault are uncertain. Because the offset terrace is below and between terraces that aggrade to moraines of the last glacial period upstream, I consider it to be postglacial in age, and assume it formed 6–12 ka. The fault has a sinuous trace that suggests a shallow dip. A trapezoidal probability distribution for the dip, with maximum probability between 20–40°S (section 3.4), gives a dip-slip rate of 0.1 +1.1/–0.07 mm/yr for the North Kyrkungey fault (Figure 4.16d). Although we saw evidence for recent surface ruptures along the fault trace, small cumulative displacement of less than a few meters across older late Quaternary surfaces (such as the terraces in the background of Figure 4.16b) suggests that the late Quaternary slip rate is low.

4.5.2 South Kyrkungey fault

The South Kyrkungey fault lies 2–3 km south of the North Kyrkungey fault and strikes parallel to it (Figure 4.15). The fault has displaced, southeast-side up, a broad terrace ~40 to 75 m above the modern Kashkasu and Bogoshti-Kakasu rivers (Figure 4.17a). A profile across the fault scarp shows a vertical separation of 24 ± 5 m (Figure 4.17b). Many gullies along the scarp face are deflected left-laterally about 1–2 m—evidence for a component of sinistral slip. The straight map trace implies that the fault has a steep dip; I use a trapezoidal probability distribution with maximum likelihood between 30–70°S in the slip-rate calculations (section 3.4).

I estimate the age of the displaced terrace from stratigraphic relationships and correlation to dated terraces in other intermontane basins. Air-photo analysis and field observations show that moraines inferred to be from the last glacial period cover a terrace that correlates to the one we measured. The stratigraphic relationship and the height and prominence of this terrace indicate it is the QII(2) terrace (K. Abdrakhmatov, unpublished data). Assuming that major terraces aggraded and incised synchronously, I assign it an age of 141 ± 17 ka (Chapter 2, Figure 2.6). The parameters described above yield a rate of dip slip for South Kyrkungey fault of 0.2 +0.9/–0.1 mm/yr (Figure 4.17b). The eastward continuation of the fault into the Kashkasu River valley does not appear to offset an inset terrace, nor does it interrupt the same low terrace that is cut by the North Kyrkungey fault. This negative evidence supports the low slip rate.

4.6 Summary of slip rates

We identified eight faults that appear to have the highest late Quaternary slip rates along an approximately north-south transect that crosses the northern two-thirds of the central Tien Shan (Figure 4.18). The rates of dip-slip faulting on individual faults range from ~0.1 mm/yr to ~2.9 mm/yr. Most of this slip accommodates shortening in a north-south direction. The high slip rates of faults within the intermontane Kochkor and Naryn basins show that late Quaternary shortening was distributed across the belt.

The most active faults lie in the major Cenozoic basins. Both mapping of their surface traces and measurements of terrace deformation indicate that they splay from faults that dip beneath five mountain ranges. The upper crust probably consists of fault-bounded blocks with a spacing of ~35 to 80 km. While the dominant motion of these blocks is north-south shortening, the factor of two or more change in slip rate along the Issyk-Ata fault may be evidence for vertical axis rotation (e.g., Cobbold et al., 1994). Other evidence for block rotation may come from the southern At-Bashi and Aksay basins, where active faulting appears restricted to the western and eastern portions of those basins, respectively. However, the change in fault activity along strike may only be apparent, and instead reflect changes from localized and easily detectable faults accommodating shortening to more distributed displacement near the surface or longer-wavelength fault-related folds.

Because several faults within the ranges displace an early Cenozoic erosion surface (Figure 1.3), some late Quaternary deformation probably took place there. However, these faults transect areas of high relief with eroding hillslopes and steep, bedrock-floored channels. Deposits and landforms that could record late Quaternary fault slip are consequently rare. For example, although the 1911 $M \approx 8$ Chon-Kemin earthquake produced surface rupture in the steep-sided Chon-Kemin valley (Bogdanovitch et al., 1914; Kuchai, 1969) (Figure 4.18), landslides and aggrading debris-flow fans have covered much of the evidence for prior events along this portion of the fault trace (Delvaux et al., in review).

In the next chapter, I attempt to address the question of how much of the shortening occurs by slip on the major faults described above, by comparing late Quaternary slip rates to current geodetic shortening rates.

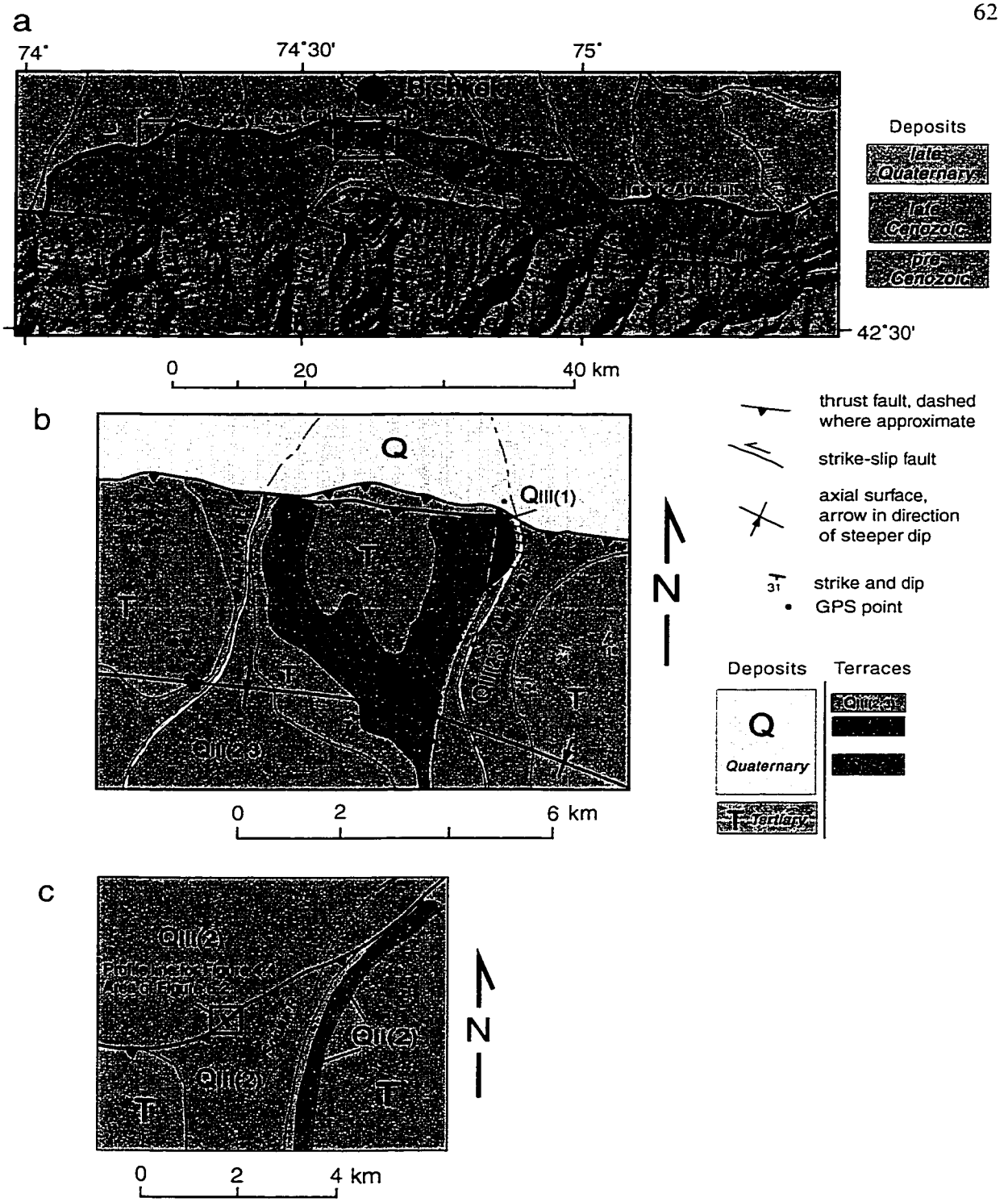

Figure 4.1: Maps of the Issyk-Ata fault, Chu basin. (a) Tectonic map of the southern Chu basin, showing major faults, geologic units, and rivers on a shaded-relief digital topographic base. (b) Geologic map of the Alamedin River site, showing terraces, differential GPS survey points, and strikes and dips of Tertiary strata. (c) Geologic map of the Sokuluk River site, showing QIII(2) fan, QII(2) terrace, and profile line for Figure 4.4.

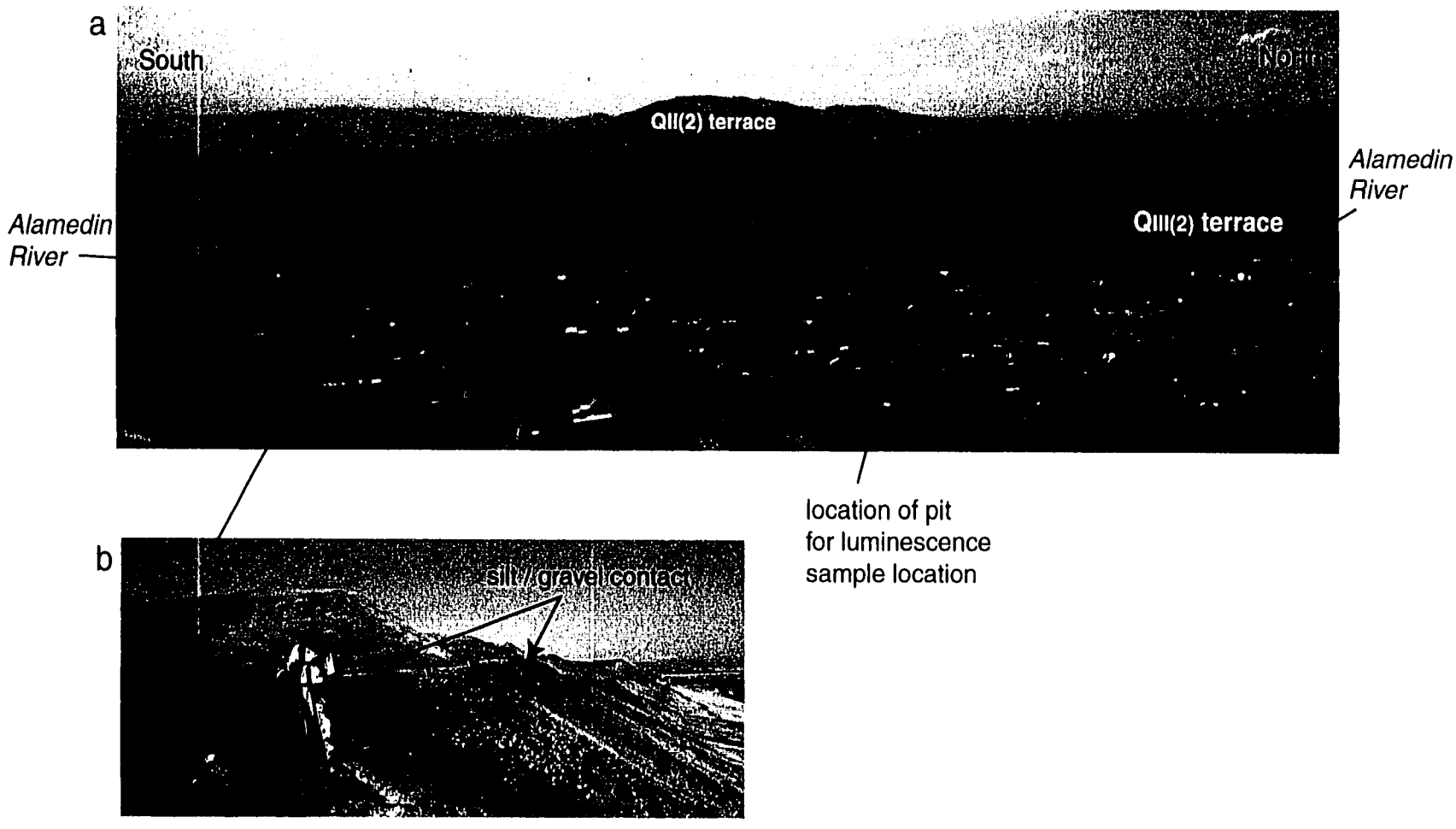

Figure 4.2: Photos of the Alamedin River terraces. (a) Folded terraces of the Alamedin River (river flows to the north). Note the south-dipping QII(2) terrace surface at the south end of the photo (labeled "backlimb"), and inset QIII(2) and QIII(3) terraces (in foreground, under houses and trees). (b) View north along the contact between fluvial gravel and overlying fine-grained deposits (mostly silt) for the QII(2) terrace. Location of the luminescence samples that date the formation of the QII(2) terrace is indicated.

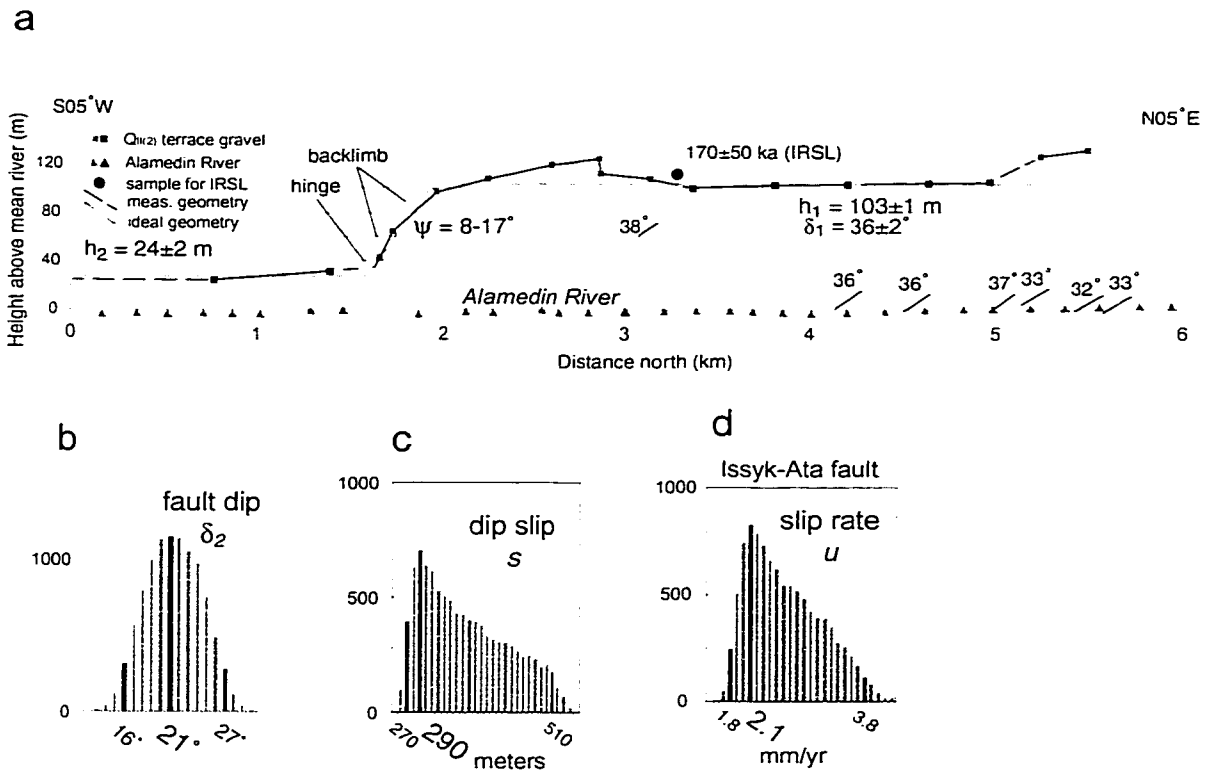

Figure 4.3: Slip-rate evaluation for the Issyk-Ata fault at the Alamedin River. (a) Alamedin River profile, showing the deformed $Q_{II(2)}$ terrace west of the river, the location and age of the sample collected for luminescence dating, and the apparent dips of Neogene strata exposed below the terraces. Points along the $Q_{II(2)}$ terrace are from differential GPS surveying. Points along the Alamedin River are from 1:25,000-scale topographic maps with a 5-m contour interval (gray) and differential GPS (black). The modern river gradient was removed by rotating the data about a horizontal axis so that the x-axis is parallel to the gradient of the river. Apparent dips of strata were similarly rotated. Solid black lines connect surveyed points with continuous exposure; black dashed line indicates our interpretation of a hinge and secondary folding near the top of the hinge and at the northern front. The dashed gray line schematically illustrates the simplification of the geometry of the terrace; this line is constrained by the black points that define the terrace south and north of the fault bend. We base the slip-rate calculation on this simplified geometry with the values of h_1, h_2, ψ, and δ_1 indicated on the figure. The method for calculating slip rate is described in Appendix B. (b) Histogram showing the predicted value of δ_2, based on equation B2 in Appendix B. The black bars indicate the 95% confidence minimum and maximum, and the most probable value. (c) Histogram showing the predicted amount of dip slip on the Issyk-Ata fault since formation of the $Q_{II(2)}$ terrace. (d) Histogram showing the probability distribution of slip rate.

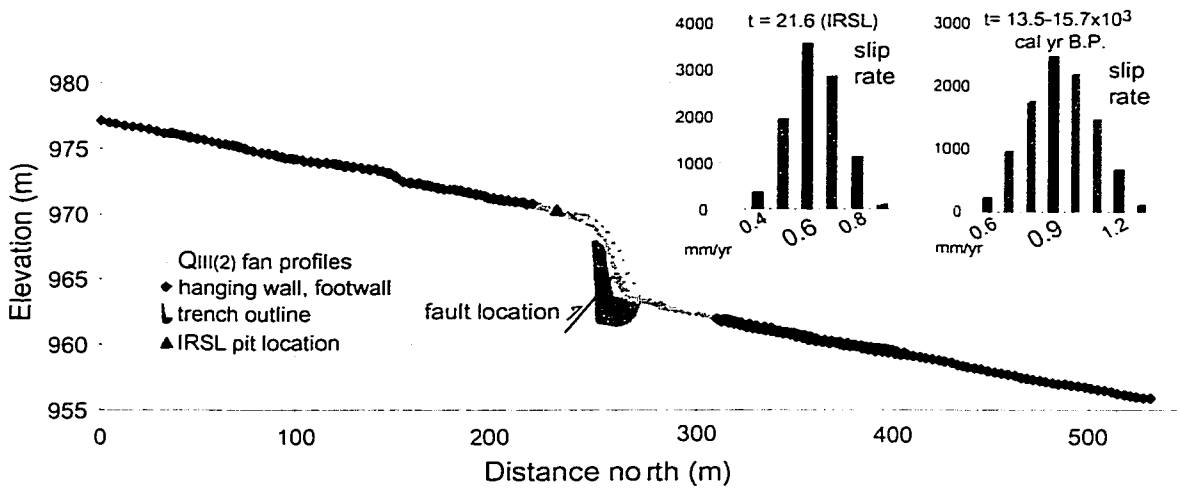

Figure 4.4: Profile of the QIII(2) fan surface across the Issyk-Ata fault west of the Sokuluk River; location of the profiles is shown on Figure 6.2. Black diamonds indicate the points used to define the surfaces on the hanging wall, and footwall. The outline of the trench and location of the fault are projected onto the scarp. The pit excavated in the hanging wall for IRSL sample collection is indicated with the triangle. Inset histograms show the slip rate distributions using the 21.6 ka IRSL age and the ~14.5 ka combined age for the QIII(2) terrace dated elsewhere (Chapter 2). The most probable slip rates and the 95% confidence limits are indicated by the black bars and corresponding values.

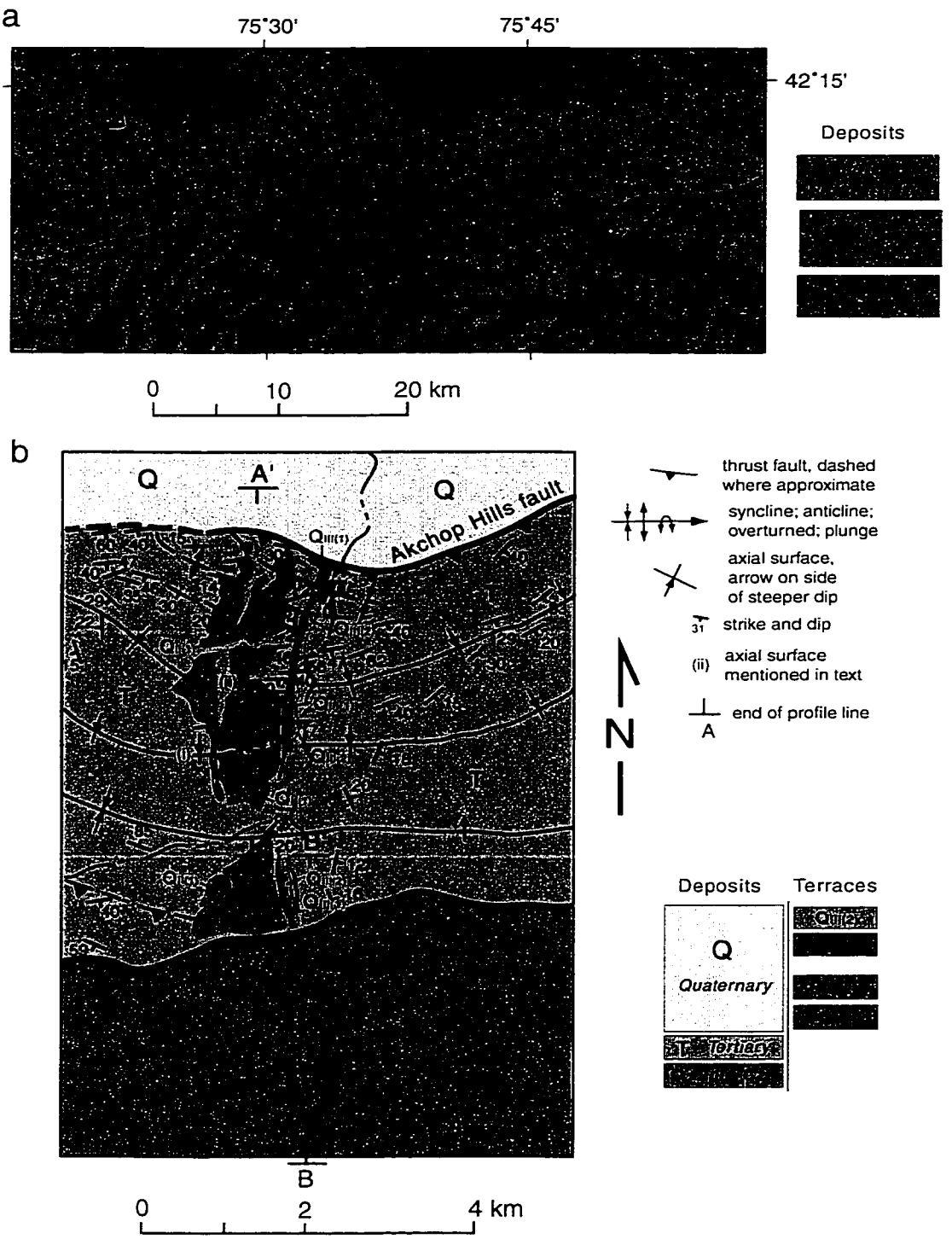

Figure 4.5: Maps showing active deformation in the southern Kochkor basin. (a) Simplified geologic map. The Akchop Hills consist of folded Tertiary strata in the hanging wall of the Akchop Hills fault. (b) Geologic map of the Djuanarik River area, showing nested terraces along the west bank of the Djuanarik River and strikes and dips of underlying strata. Axial surfaces labeled (i), (ii), and (iii) are discussed in the text and in later figures. Surveyed points along the extensive $Q_{II(2)}$ terrace constrain our analyses of slip rate for the Akchop Hills fault (profile line A-A') and South Kochkor fault (profile line B-B').

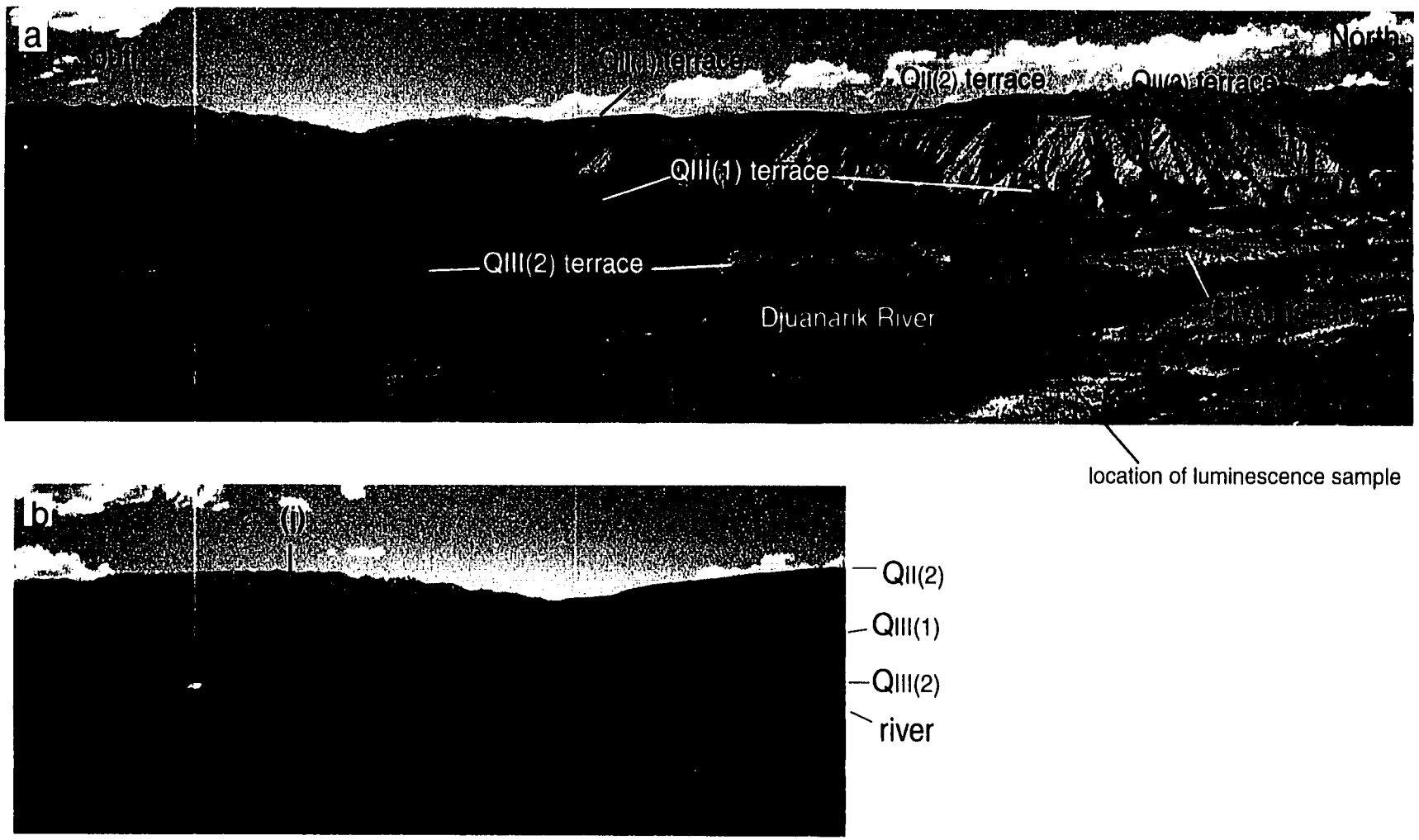

Figure 4.6: Nested terraces along the west side of the Djuanarik River, Kochkor basin. See Figure 4.7 for scale. (a) West view of terraces and Djuanarik River (the river flows north). Arrows indicate the locations of the luminescence sample pit and the charcoal sample. (b) West view of the Djuanarik River terraces across active axial surface (i).

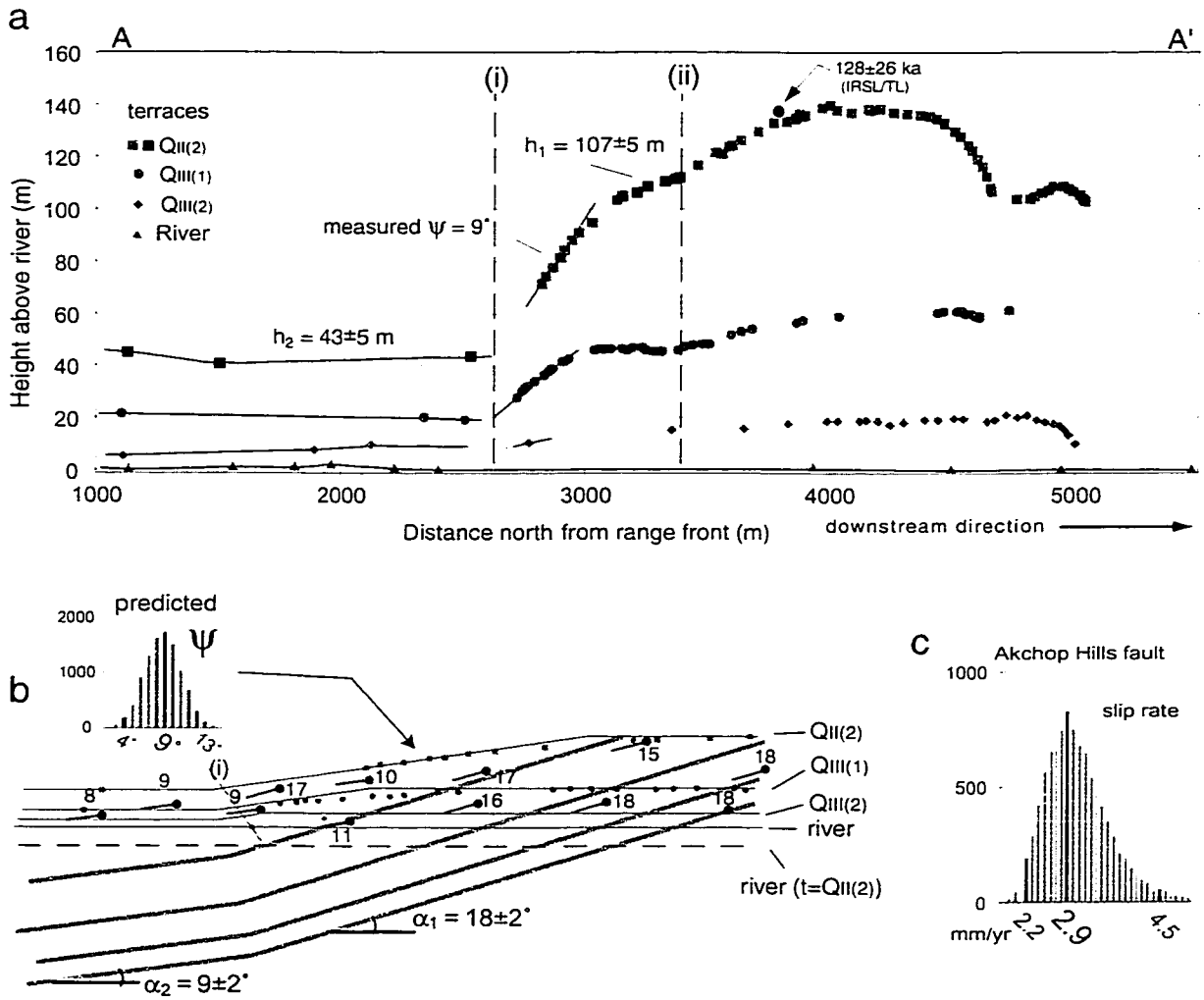

Figure 4.7: Slip-rate determination of the Akchop Hills fault from the Djuanarik river terraces. (a) River terrace profiles were rotated counter clock-wise 0.7° so the horizontal axis would parallel the modern river. Note the progressive limb rotation and kink-band migration recorded by the backlimbs of the $Q_{III(1)}$ and $Q_{II(2)}$ terraces off of active axial surfaces (i) and (ii): I infer a back limb for the $Q_{III(2)}$ terrace but did not sample enough points to measure it. The black squares on the $Q_{II(2)}$ terrace were used to define the heights of the terrace across axial surface (i). (b) Cross-section across axial surface (i), showing apparent dips of Pliocene Djuanarik Formation strata and surveyed points along the terraces and modern river. Thick gray lines schematically illustrate dipping strata across the fold. Thin black lines show the predicted terrace profiles assuming that the terraces are deformed by ideal fault-related folding (see Chapter 3). Inset box shows the predicted backlimb angle (equation 8 in section 3.3). Horizontal dashed line shows inferred position of the river at the time of $Q_{II(2)}$ terrace formation. (c) Histogram showing slip-rate probability distribution for the Akchop Hills fault based on equation 7 in section 3.3.

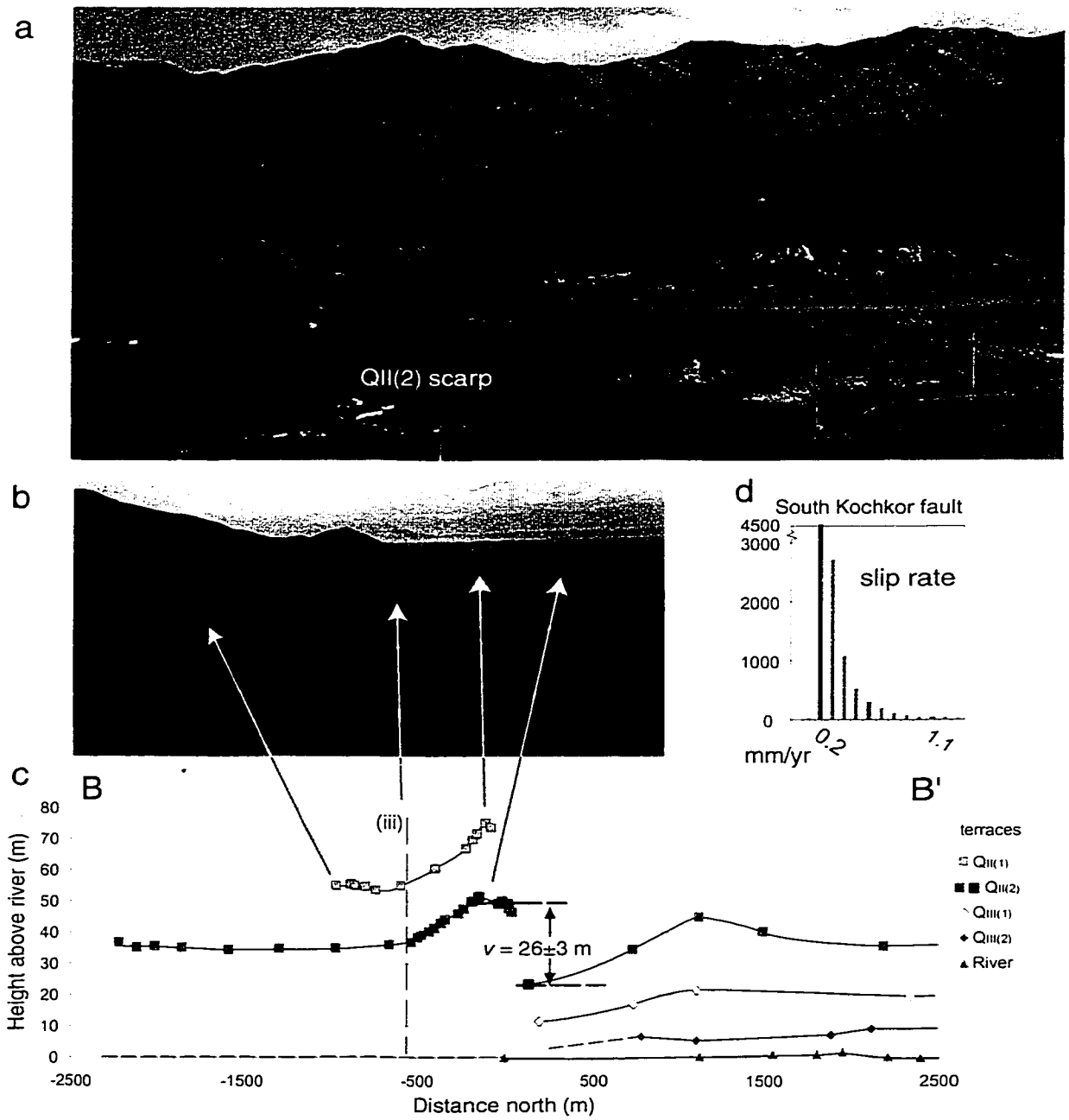

Figure 4.8: Slip rate of the South Kochkor fault. (a) View south from the QII(2) terrace towards the range front. Arrow points to the fault scarp across the QII(2) terrace. (b) View northwest from the range looking towards the range front. Lower silt-covered terrace on the opposite side of the river is the QII(1); the QII(2) terrace is on the east side of the river below the photographer. The gulley is the approximate location of axial surface (iii). Wide silt-covered terrace at the range front is the QII(2) terrace. (c) Profile of river terraces across the South Kochkor fault, showing terrace correlation, and folding in the hanging wall across axial surface (iii). Black points and horizontal dashed lines indicate the vertical separation used in the slip rate calculation. (d) Histogram showing slip rate calculation for the South Kochkor fault. The 0.2 mm/yr bin contains the minimum slip rate (2.5% tail). Adding another significant digit to the histogram bins yields a 0.17 mm/yr minimum slip rate.

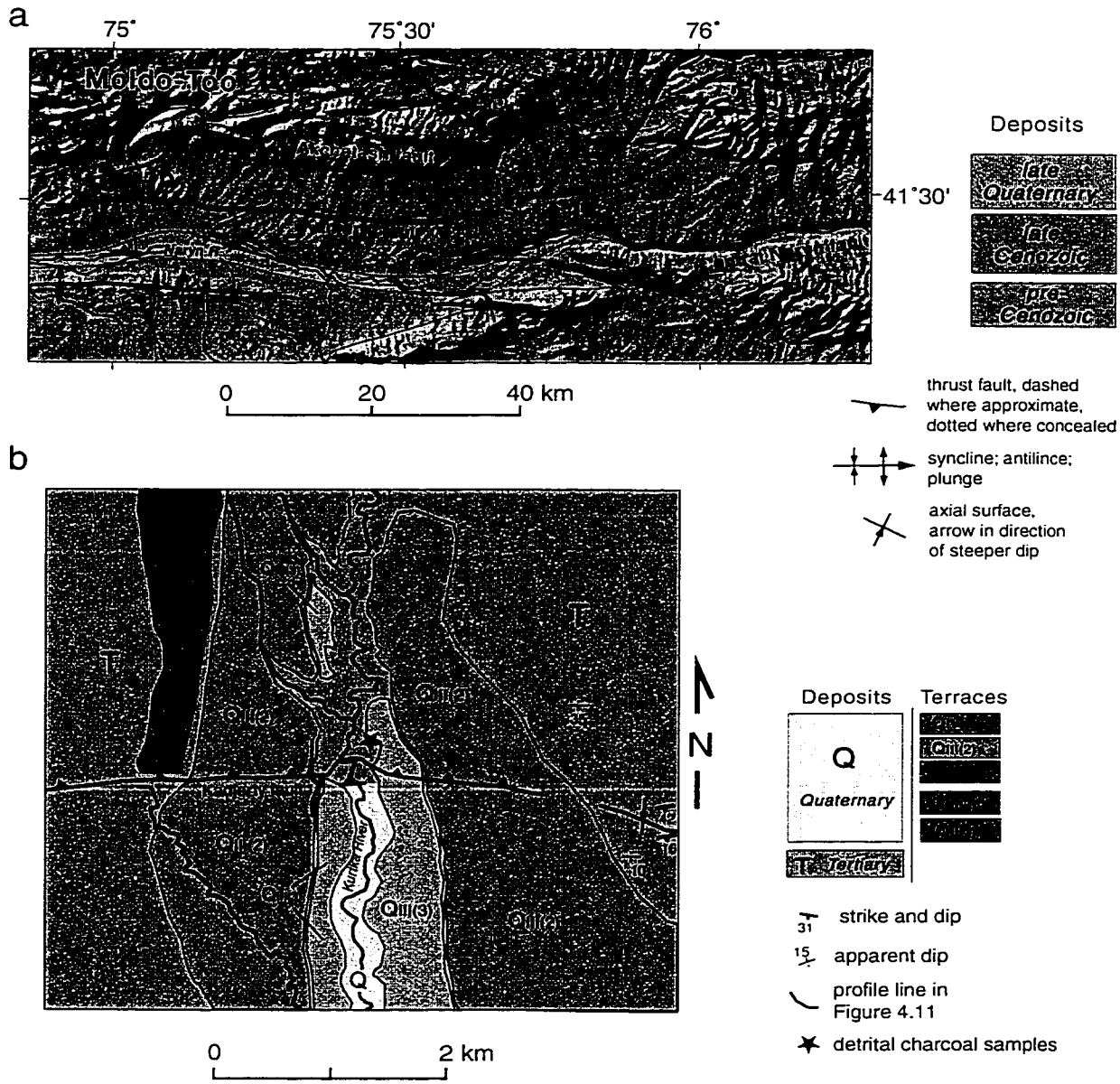

Figure 4.9: Maps of the northern Naryn basin. (a) Simplified geologic map of northeastern Naryn basin. The Kadjerty and Central Naryn faults appear to accommodate most of the shortening at the surface across the northern Naryn basin margin. Boxes show the areas of (b) and (c). (b) Geologic map along the Kurtka River, showing dips of Tertiary strata, trace of the Kadjerty fault, and river terraces. Red line indicates the profile in Figure 4.11.

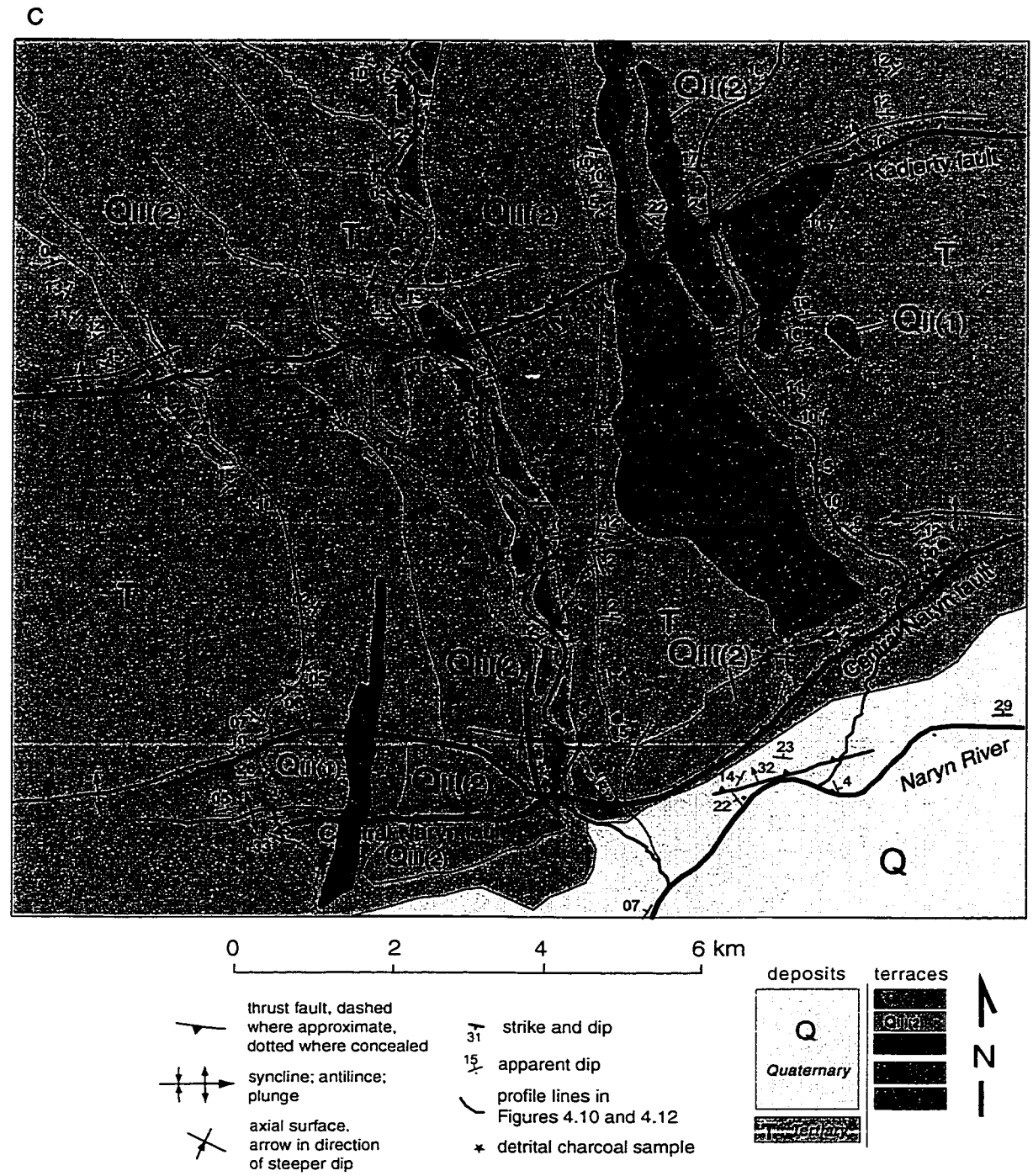

Figure 4.9 (continued): (c) Geologic map along the Kadjerty River, showing dips of Tertiary strata, fault and fold traces, and river terraces. Red lines show locations of the profiles of the QIII(2) terrace across the Kadjerty and Central Naryn faults (Figures 4.10 and 4.12).

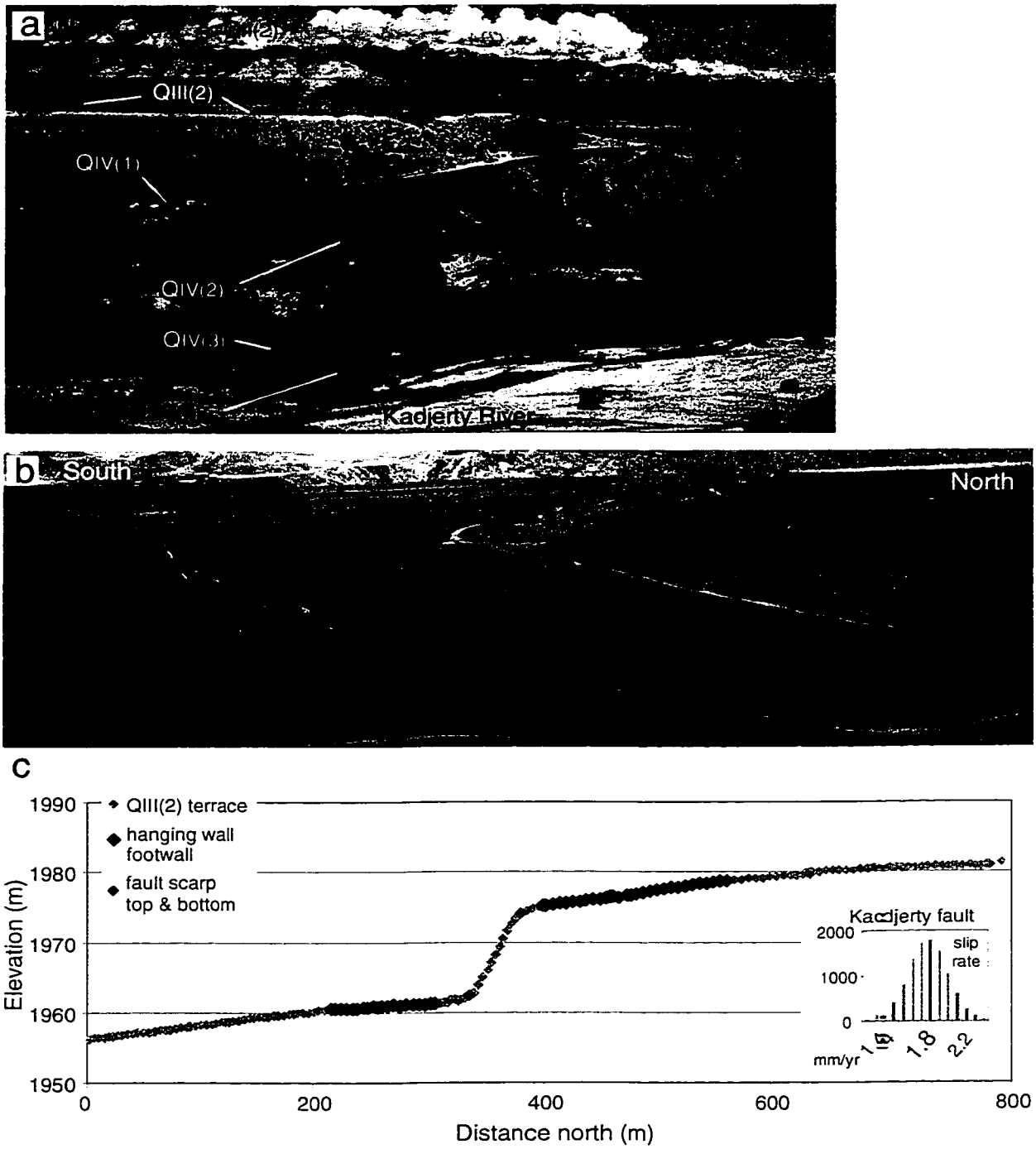

Figure 4.10: Kadjerty fault in the Kadjerty River valley. (a) View east of the Kadjerty fault cutting nested terraces. Black arrows indicate the position of the fault scarp. The scarp across the QII(2) terrace in the distance is ~80 m high. (b) View west from the QII(2) terrace looking across the faulted QIII(2) terrace. Location of the profile in (c) is approximated by the black line. (c) Profile of the QIII(2) terrace across the Kadjerty fault. Large black diamonds indicate the points used to define the surfaces on the hanging wall and footwall; small black diamonds indicate the top and bottom of the fault scarp. Inset histogram shows the slip rate distribution.

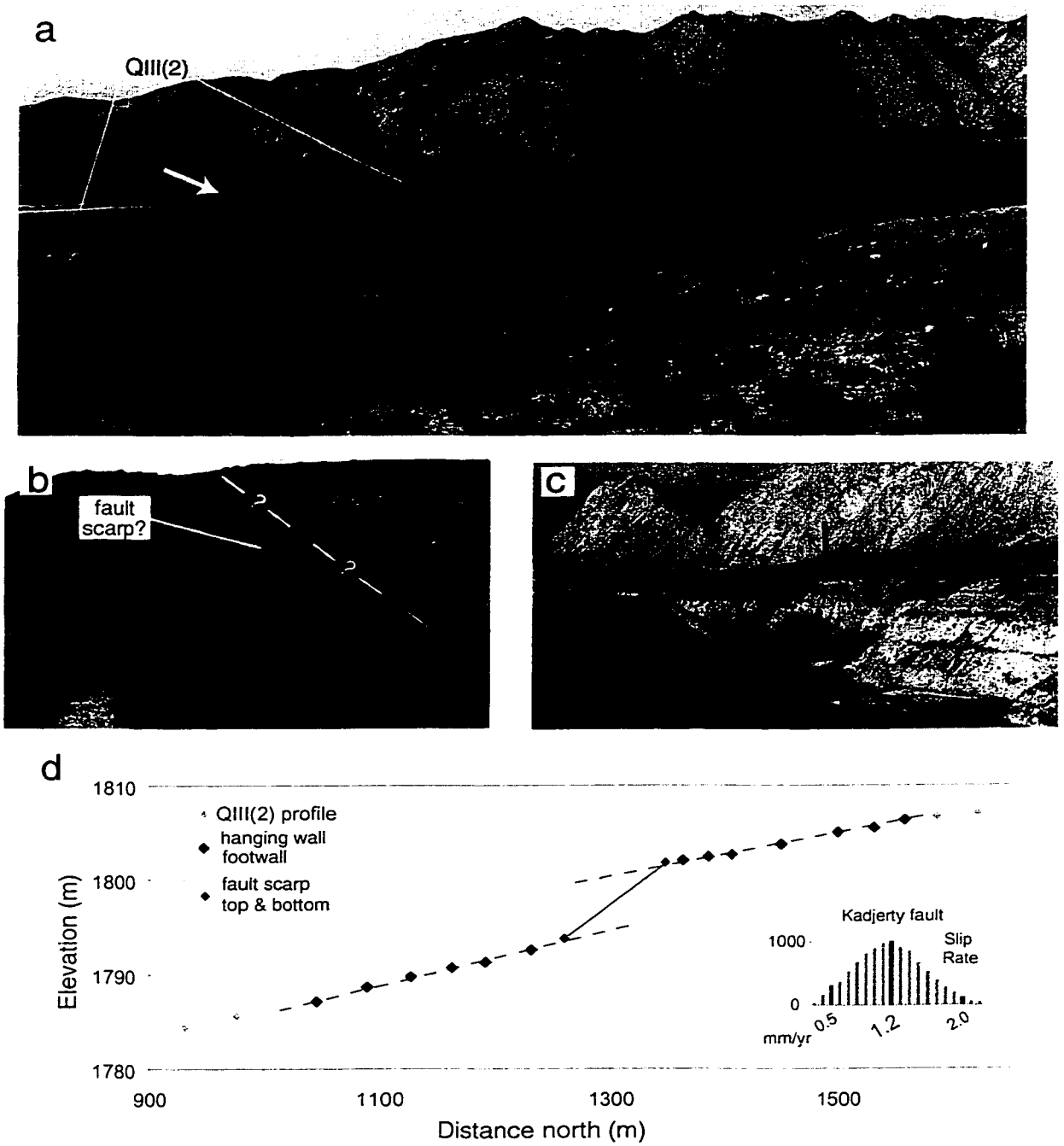

Figure 4.11: Kadjerty fault in the Kurtka River valley. (a) View west of the Kadjerty fault cutting the QIII(2) and QIII(3) terraces. White arrow indicates the fault scarp west of the river. The person in the foreground is on the QIII(2) fault scarp east of the river. (b) Querried dashed line indicates the location of the Kadjerty fault in the west river bank, as suggested by the change in height of the inset strath terrace. Scarp is about 2 m high. (c) View northeast of the QIII(2) and slightly inset QIII(3) terraces east of the Kurtka River. Arrow shows the outcrop where charcaol was collected. (d) Profile of the upper gravel contact of the QIII(2) terrace across the Kadjerty fault on the west side of the Kurtka River. Large black diamonds indicate the points used to define the surfaces on the hanging wall and footwall; small black diamonds indicate the top and bottom of the fault scarp. Inset histogram shows the slip rate distribution.

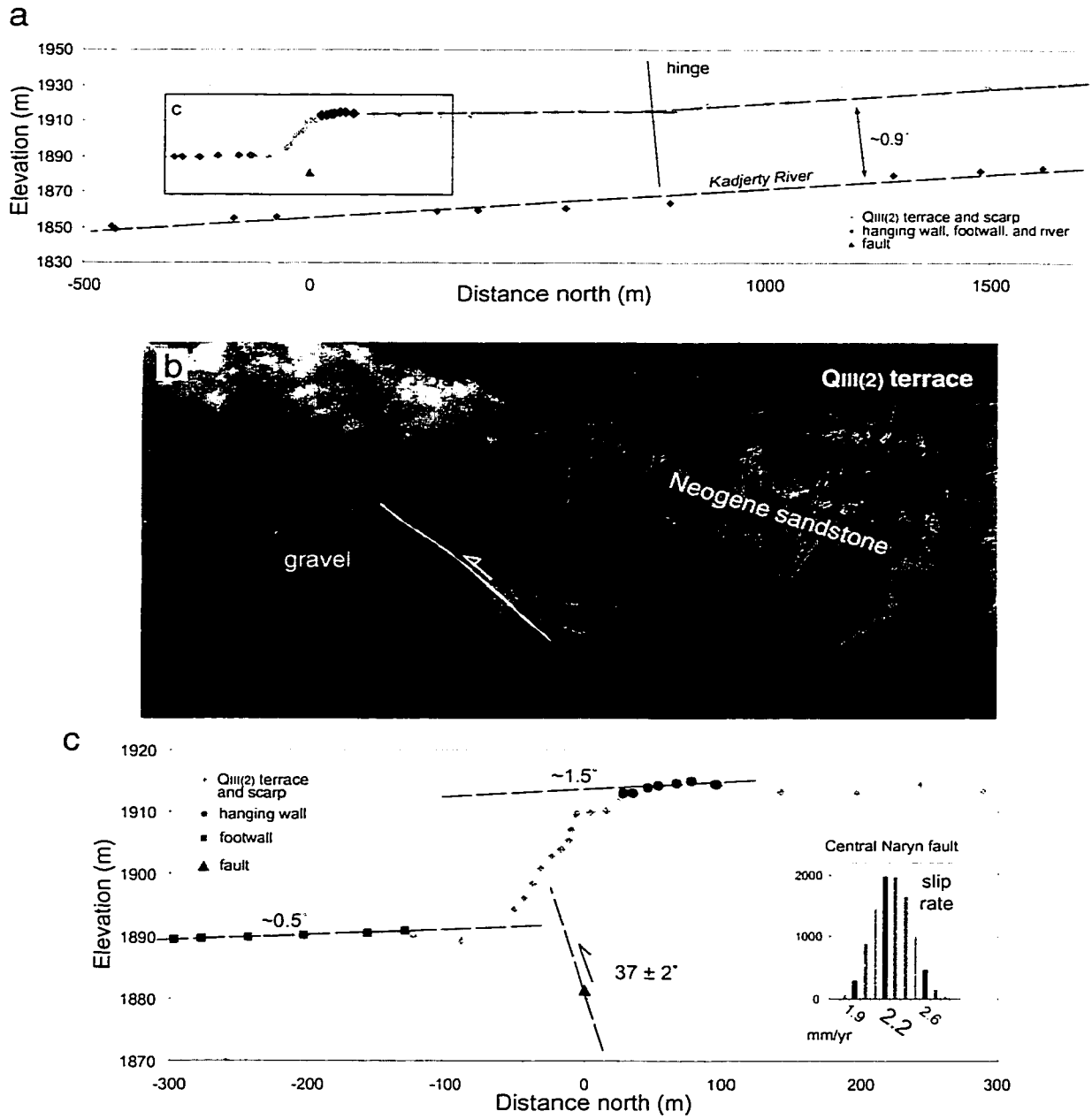

Figure 4.12: Central Naryn fault near the Kadjerty River. (a) Profile of the upper gravel contact of the Qiii(2) terrace across the Central Naryn fault; profile is located on Figure 4.9b. The gradient of the Qiii(2) terrace and the modern river are similar north of the labeled "hinge," but south of the hinge the terrace surface is subhorizontal, indicating that it has been rotated due to slip on the Central Naryn fault. (b) Central Naryn fault dipping 37±2°N is exposed along the west bank of the Kadjerty River. View is to the southwest. Neogene strata in the hanging wall dip ~11-15°N. Notice the thick accumulation of late Quaternary gravel in the footwall of the fault compared to the gravel in the hanging wall. (c) Profile across the fault scarp, showing the surveyed points used to define the hanging wall and footwall and the dips of those surfaces. A single point surveyed on the exposed fault surface and the measured dip are used to constrain the fault location in the slip rate calculation. The inset box shows the probability distribution of slip rate.

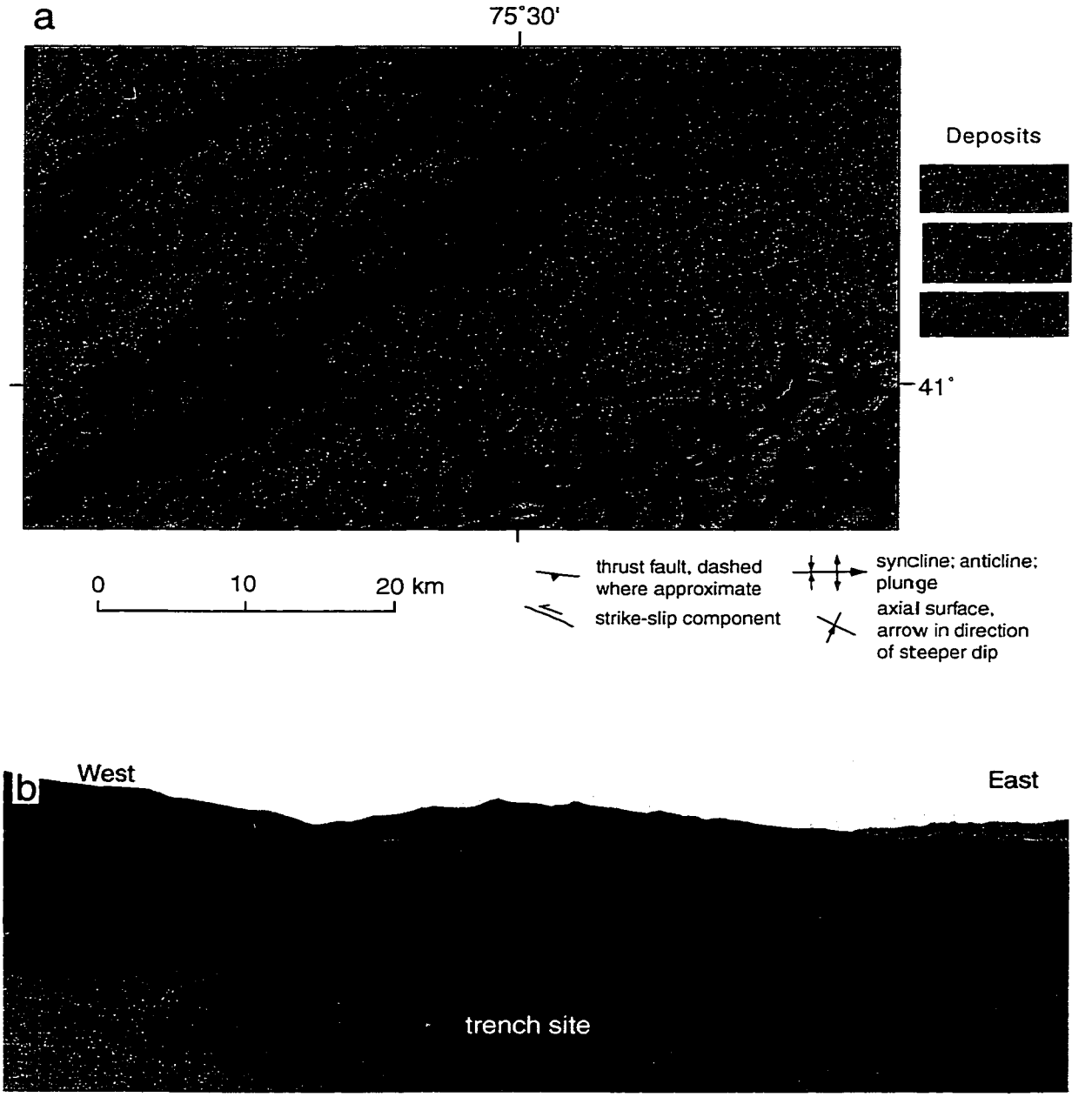

Figure 4.13: Map and photos of the Oinak-Djar fault, At-Bashi basin. (a) Simplified geologic map of the western At-Bashi basin. The Oinak-Djar fault marks the boundary between Tertiary strata and late Quaternary deposits, and defines the southeast margin of deformation for the larger structure that separates the Naryn and At-Bashi basins. The Oinak-Djar fault reaches the surface along the western half of the mapped trace; to the east the fault is blind, and the surface expression is a fault-propagation fold with a sharp synclinal axial surface. Trench site is indicated by the boxed area. (b) View north of the Oinak-Djar fault (between horizontal arrows) and the trench site. The trench site is on the eastern side of a broad wash that has several progressively offset terraces.

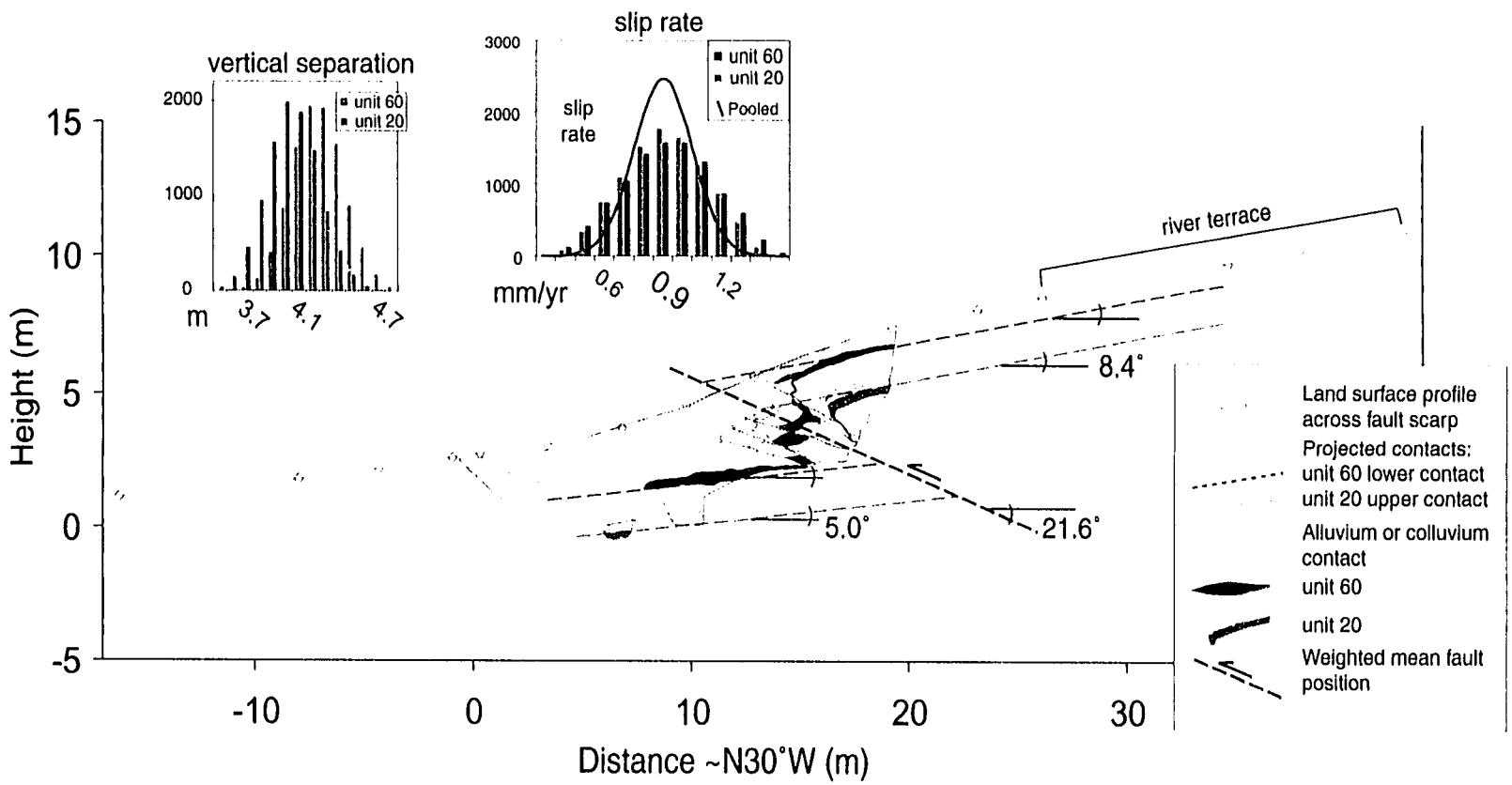

Figure 4.14: Slip rate of the Oinak-Djar fault. A simplified map of the western trench wall is shown with a profile of the land surface. The slope of an inset river terrace in the hanging wall is assumed to represent the original depositional slope of the hanging-wall strata, and is used to project units 20 and 60 into the fault zone. Changes in layer dip near the fault are interpreted to be due to drag folding. The position and dip of the fault are determined by a weighted average of the dips and displacements of the four fault splays. Histograms above the profile show the similar amounts of vertical separation and slip rate for units 20 and 60. The solid line in the slip rate histogram shows the pooled mean slip rate and uncertainty by combining the two measurements. Figure 6.6 shows the setting of the trench and the inset terrace; Figure 6.7 shows a more detailed trench log.

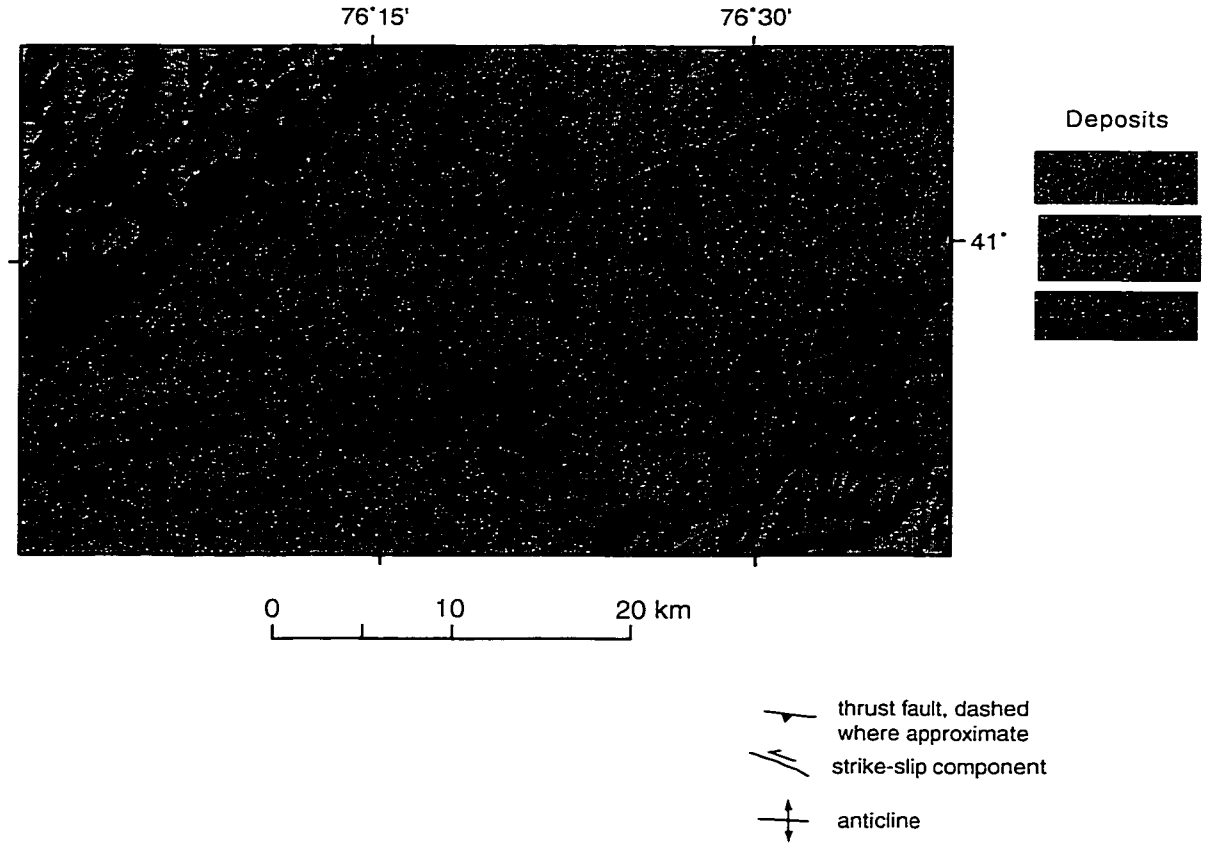

Figure 4.15: Simplified geologic map of the eastern Aksay basin. The North and South Kyrkungey faults are part of a zone of late Quaternary folds within the northeastern Aksay basin, and appear to accommodate most of the shortening across the basin. Late Quaternary deposits include large amounts of glacial till and outwash; large moraines from the last glacial period are preserved along the southern At-Bashi Range front and are not offset by more than ~1 m by the North Aksay fault. Locations of photos in Figure 4.16 and profile line in Figure 4.17 are shown.

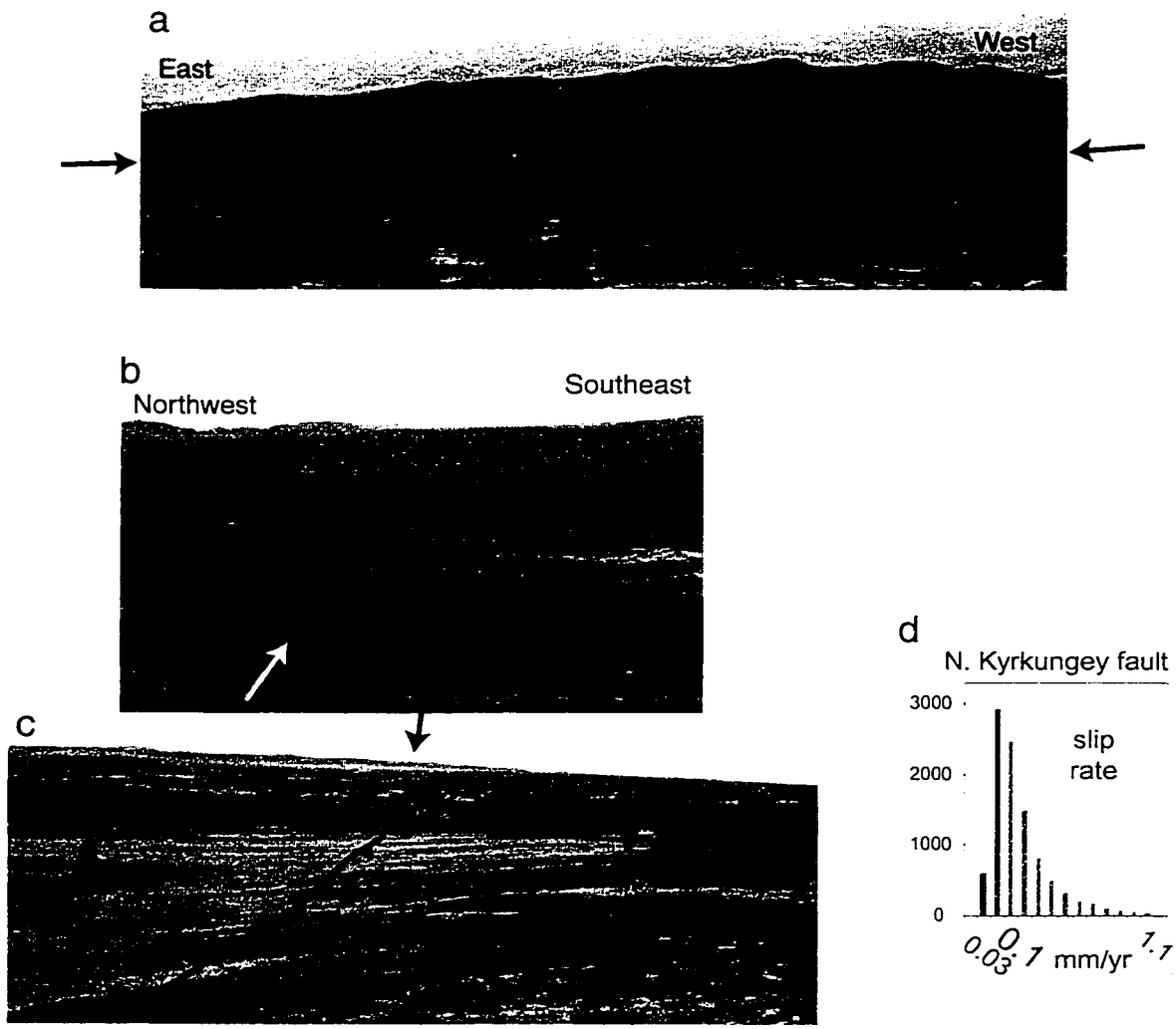

Figure 4.16: Slip rate of the North Kyrkungey fault. (a) View to the south of the North Kyrkungey fault scarp. The fault separates hills of Tertiary strata in the hanging wall from aggrading alluvial fans in the footwall. Although the fresh scarp morphology (between arrows) indicates recent activity, the muted morphology of the hills in the hanging wall and the lack of well-developed facets in the interfluves suggest that the fault does not have a high slip rate relative to Holocene-active faults in the intermontane basins to the south. (b) View to the northeast of the contrasting vegetation and ground wetness that marks the North Kyrkungey fault (between arrows) where it crosses the floodplain of the southeastward flowing Kashkasu River. The southeast side of the fault is uplifted relative to the northwest side. (c) View to the northeast along the fault scarp (marked by the fault line) across the floodplain of the Kashkasu River. Hand-level measurements across the scarp suggest a height of 1 ± 0.5 m. (d) Histogram showing probability distribution of slip rate for the North Kyrkungey fault. Minimum rate is shown with an extra significant figure to distinguish it from zero.

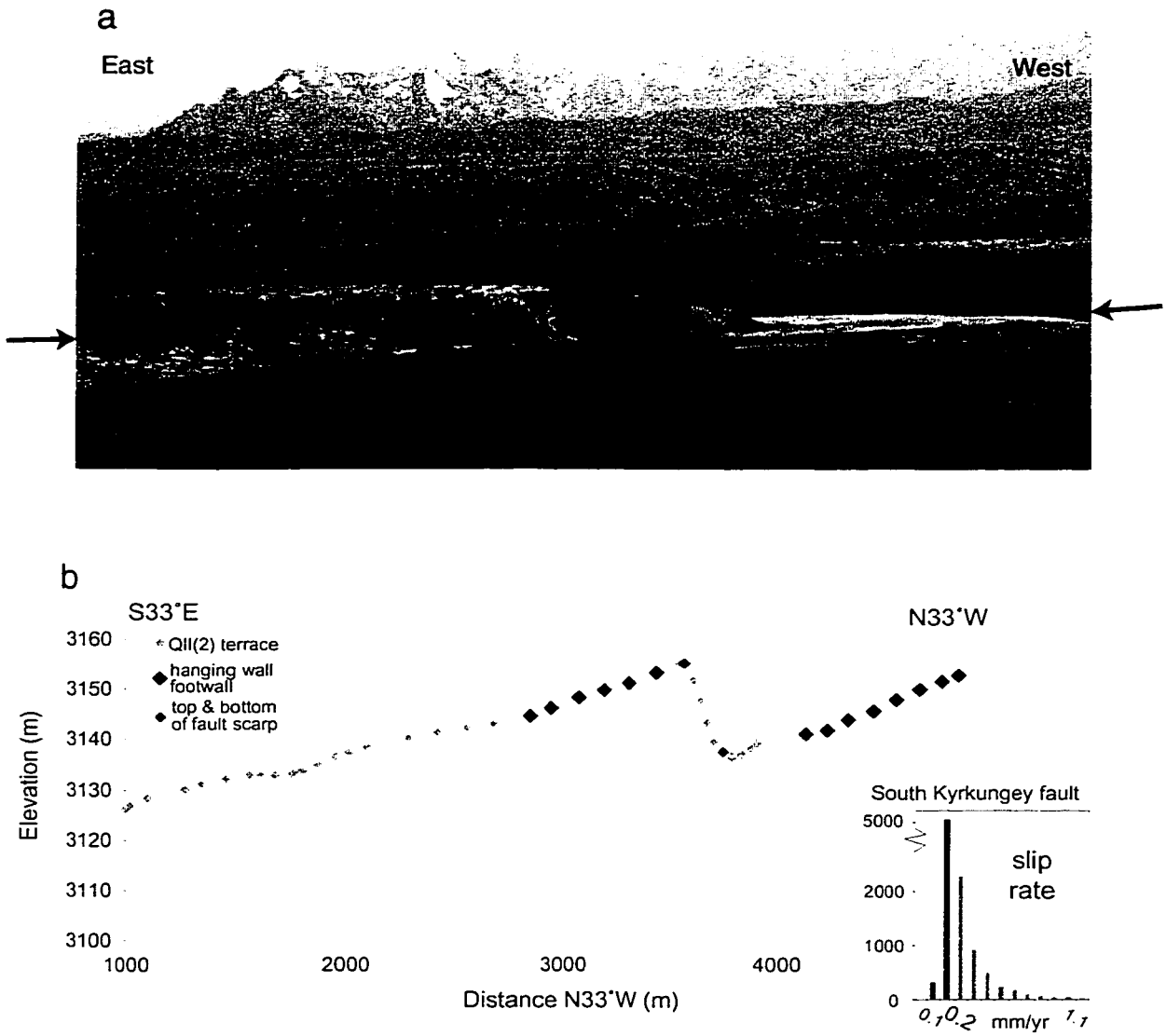

Figure 4.17: Slip rate of the South Kyrkungey fault. (a) View to the south of the South Kyrkungey fault (between arrows). The north-vergent fault here displaces the $Q_{II(2)}$ terrace in the hanging wall against small fans and the modern floodplain of the Bogoshti-Kakasu River, which lies west of the Kashkasu River. East of the photo the older terrace is preserved in the footwall of the fault, which is the location of the topographic profile shown in (b) (see also Figure 4.15). (b) Profile of the $Q_{II(2)}$ terrace surface across the south-dipping South Kyrkungey fault. Inset histogram shows the probability distribution of slip rate for the fault.

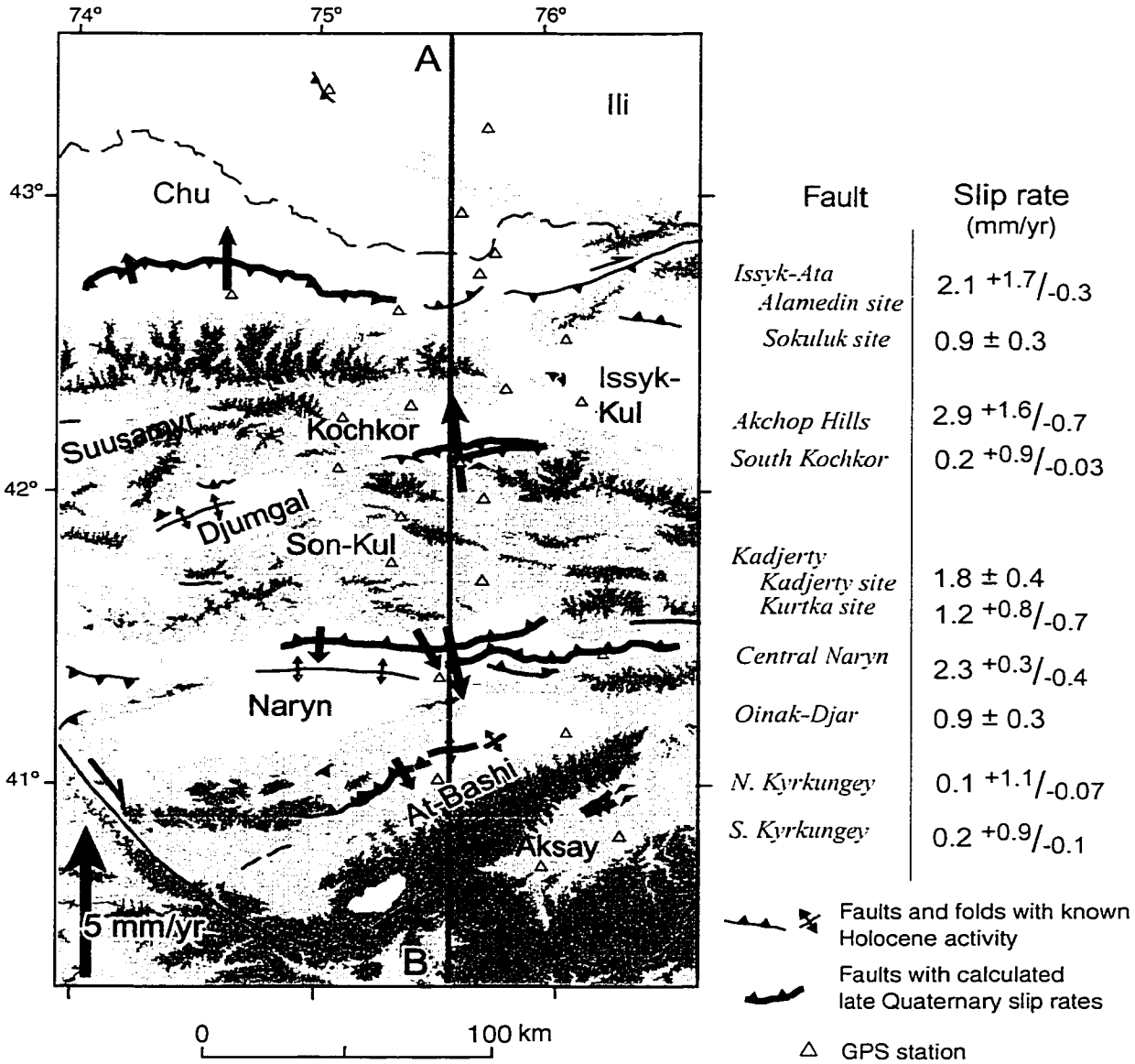

Figure 4.18: Recently active faults and fault slip rates. Gray-scale changes indicate 1500, 2500, 3500, and 4500 m contours. Vertical arrow in lower left corner represents 5 mm/yr slip rate. The arrows point in the up-dip direction and are oriented perpendicular to local fault strike, to emphasize that the data represent the dip-slip portion of fault slip only. The slip rate values and 95% confidence intervals are shown on the right. The north-south components of the shortening rates are projected along fault strike to profile line A-B. Triangles show GPS stations used to compare north-south shortening rate in Figure 5.3. The north component of velocity at each GPS site was measured relative to station AZOK, which lies north of this map.

Chapter 5

Converting slip rates to geologic shortening rates

To evaluate whether the faults we identified account for the total crustal shortening along a transect across the Kyrgyz central Tien Shan, I converted the calculated fault slip rates into crustal shortening rates, which I then compared with modern crustal velocities measured by GPS (T. Herring, written communication, 2001) (Figure 4.18). North velocities determined at GPS sites were projected normal to a north-south transect line, while geologic slip rates were projected along fault strike. As some of our study sites are tens of kilometers away from the transect line, I treat fault slip as constant along strike, recognizing that such an assumption cannot be correct everywhere (section 4.6).

5.1 Fault geometry in the upper crust of the Tien Shan

Our mapping indicates that the faults with high slip rates in the intermontane basins are splays that connect at shallow depths with faults with lower slip rates that occur along the margins of the basins. Thus, slip rates determined for two faults at the surface within the same intermontane basin (i.e., at Kochkor, Naryn, and Aksay basins) likely combine to represent slip on a single crustal-scale ramp at depth. How the geometry and displacement along a fault change between the point of measurement at the surface and at ~2–20 km depth affects the comparison between slip rates and horizontal velocities measured by geodesy across a region.

A cross-section of the southern Kochkor basin, based on the mapping and terrace profiling in Figures 4.5–4.8, provides a typical example of how I interpret the fault geometry across the basin margins (Figure 5.1). The thrust ramp beneath the Akchop Hills must shallow south of the fold to account for the change in vertical height of the terraces. This low dip angle, which I infer from dips of Tertiary strata is ~8° or less, projects beneath the Tersky Ala-Too range front. The South Kochkor fault dips south at a higher angle, and unless the fault shallows to a similar ~8°S dip, it will intersect the Akchop Hills fault. The profile of the QII(2) terrace south of the range front implies that the dip of the fault system is shallow for at least two kilometers south of the

range front (Figures 4.8 and 5.1). The ~3 km length of the gently dipping fault that places Paleozoic rock on Tertiary rock reflects the approximate amount of shortening inferred across the Akchop Hills fault.

The ~4–5 km of structural relief on the pre-Cenozoic unconformity across the southern Kochkor basin margin implies that a crustal-scale ramp underlies the Tersky Ala-Too. Although the dip of the crustal-scale ramp is uncertain, the intermediate dip shown in Figure 5.1 is likely based on focal mechanisms of moderate-sized earthquakes and the 50 ± 13° dip of the fault plane that ruptured during the 1992 Suusamyr earthquake (Mellors et al., 1997; Ghose et al., 1998). Faults beneath the ranges in the Tien Shan may dip closer to ~30°, however, if the faults are similar to those imaged beneath the Rocky Mountain foreland (Gries, 1983; Stone, 1993).

The cross-section geometry proposed in Figure 5.1 is partially supported by a high-resolution magnetotellurics (MT) experiment across the southern margin of Kochkor Basin, located along the Ukok River valley 15 km east of the Djuanarik River (Figure 4.5a). The MT profile shows a ~2-km-thick layer of low-resistivity material underlying high-resistivity material at ~1 km depth along a low-angle contact. The low-resistivity layer—inferred to be Tertiary sediments thrust under Paleozoic igneous rock—extends for ~ 2 km south of the range-front. The southern end of the low-resistivity layer ends by a south-dipping contact determined to be of intermediate dip (S. Park, written communication, 2001).

5.2 Method to convert slip rate to north-south shortening rate

To convert a fault's slip rate measured at the surface into its shortening rate across a region, one cannot simply assume that slip on the crustal-scale ramp equals that on the fault segments at shallow crustal depths. Most of the faults that we have examined in this study dip ~ 20–40° at the surface and appear to flatten to dips of ~ 5–20° at depths of less than a few kilometers, within Tertiary sedimentary rock (e.g., Figures 5.1 and 5.2; Table 5.1). Fault-bend fold theory predicts that—in layered strata at least, where shear can occur parallel to bedding—slip remains approximately constant on consecutive fault segments with dips that steepen upwards (see p. 699 in Suppe (1983)).

The shallow faults that lie at a few kilometers depth appear to intersect more steeply dipping faults that underlie the mountain ranges and involve much of the previously deformed basement rock in the upper crust (Figure 5.1). Strain must occur in the hanging wall to absorb the movement in different directions of the portions adjacent to segments with different dips. The fraction of slip, s, transferred from a deeper, steeper fault (dip = δ_1) to a more gently dipping, shallower fault (dip = δ_2) is approximately equal to $\cos\delta_1/\cos\delta_2$ (see the Fault-bend Anticline example in Narr and Suppe (1994), p. 814, and Figure 5.2). If deformation of the hanging wall occurs only by shear on vertical planes, the approximate equality becomes exact. In the case where shear occurs on planes with a non-zero angle β_3, the equation for the shortening rate u_h derived in Figure 5.2, is

$$u_h = \frac{u_2 \cos\delta_2 (1 - \tan\delta_2 \tan\beta_3)}{1 - \tan\delta_1 \tan\beta_3}. \qquad (13)$$

Values of u_2 are derived from the slip-rate calculations, and I estimate (or infer) δ_2 from cross-sections and terrace profiles (Table 5.1). If there are no constraints on δ_2 based on mapping, δ_2 varies between the dip of the fault measured or estimated at the surface and 0°. The dip of the crustal scale ramp, δ_1, varies between 30° and 55°. The angle of hanging-wall shear, β_3, varies between 0 and 5° in the direction of fault vergence.

In order to compare the late Quaternary shortening rates to the north component of GPS shortening rates, I determine the N-S component of slip on faults that do not strike normal to this direction (Figure 4.18). Simple end-member cases are to assume pure dip slip on each fault (N-S component $\leq$ calculated dip slip), or to assume that oblique slip occurs such that maximum shortening is oriented N-S (N-S component $\geq$ calculated dip slip). I incorporate this uncertainty by defining ϕ as the angle between the strike-normal direction of the fault and north (Figure 5.2b) and assuming:

$$u_h \cos\phi \leq u_{hns} \leq u_h/\cos\phi. \qquad (14)$$

5.3 Results of the shortening rate comparison

Cumulative geologic shortening rate plotted against distance southward shows an approximately linear trend across the northern two-thirds of the belt, with a total rate of 11.5 +2.8/−1.5 mm/yr (Table 5.1 and Figure 5.3). The geologic shortening rates are comparable to the dip-slip rates. This is primarily due to the inference that the horizontal component of slip on a deep crustal ramp is transferred to a gently dipping fault at shallow depths, and that slip is transferred up-dip to a shallow ramp (Figure 5.2). The most probable cumulative rate of 11.5 mm/yr is larger than the sum of the most probable dip-slip rates, 10.5 mmy/yr. The broader uncertainty on the side of the maximum slip rate for the Issyk-Ata and Akchop Hills faults explains much of this difference.

The cumulative geologic rates and current GPS rates are indistinguishable at a 95% confidence level (Figure 5.3). If the total convergence rate across this area has remained constant over the past ~10^5–10^6 years, and if the GPS rates across the belt match far-field (measured across thousands of km) convergence rates (cf. Hager et al., 1999), slip on the faults we studied account for nearly all of the crustal shortening. This result suggests that only minor deformation occurs within blocks bounded by major fault zones. The faulting and folding that do occur presently within the blocks likely amount to minor adjustments within hanging walls at fault bends.

Table 5.1 Parameters used to calculate geologic shortening rate and results.

Fault name, basin	Site, marker used in analysis	Dip-slip rate (mm/yr)	Dip direction[a], ϕ (degrees)	Shallow dip[b], δ_2 (degrees)	Cumulative shortening rate[c] (mm/yr)
Issyk-Ata, Chu	Sokuluk R., QIII(2) fan	0.9 ± 0.3 or 0.6 ± 0.2 [d,e]			
	Alamedin R., QII(2) terrace	$2.1^{+1.7}/_{-0.3}$	0-10	5-24	$2.2^{+1.6}/_{-0.2}$
Akchop Hills, Kochkor	Djuanarik R., QII(2) terrace	$2.9^{+1.6}/_{-0.7}$	0-5	0-10	
S. Kochkor, Kochkor	Djuanarik R., QII(2) terrace	$0.2^{+0.9}/_{-0.03}$	0-5	0-10	$6.0^{+2.2}/_{-1.3}$
Kadjerty Naryn	Kurtka R., QIII(2) terrace	$1.2^{+0.8}/_{-0.7}$ [e]			
	Kadjerty R., QIII(2) terrace	1.8 ± 0.4	20-30	0-15	
Central Naryn, Naryn	Kadjerty R., QIII(2) terrace	$2.3^{+0.3}/_{-0.4}$	0-10	0-15	$10.2^{+2.2}/_{-1.5}$
Oinak-Djar, At-Bashi	'98 trench site, units 40, 70	0.9 ± 0.3	15-25	10-25	$11.0^{+2.4}/_{-1.4}$
N. Kyrkungey, Aksay	Kulakashu R., QIV(1) terrace	$0.1^{+1.1}/_{-0.07}$	55-65	*f*	
S. Kyrkungey, Aksay	Kulakashu R., QII(2) terrace	$0.2^{+0.9}/_{-0.1}$	25-35	*f*	$11.5^{+2.8}/_{-1.5}$

[a] Angle is measured from the normal to fault strike to north.
[b] Dip of shallow décollement inferred from geologic mapping, analysis of terrace profiles, and cross-sections.
[c] Dip of crustal ramp assumed to be 30-55°, angle of hanging-wall shear 0-5°. The cumulative rates are inferred to represent shortening at each major range front, and are generated by summing probability distributions. Most probable value and 95% confidence limits are shown.
[d] The two rates assume either a ~14 or ~21 ka age of the QIII(2) fan at the Sokuluk River.
[e] Slip rate at this site was not used in the shortening-rate analysis.
[f] Dip of shallow décollement assumed to vary between 0 and 20° less than the dip estimated for the surface fault trace.

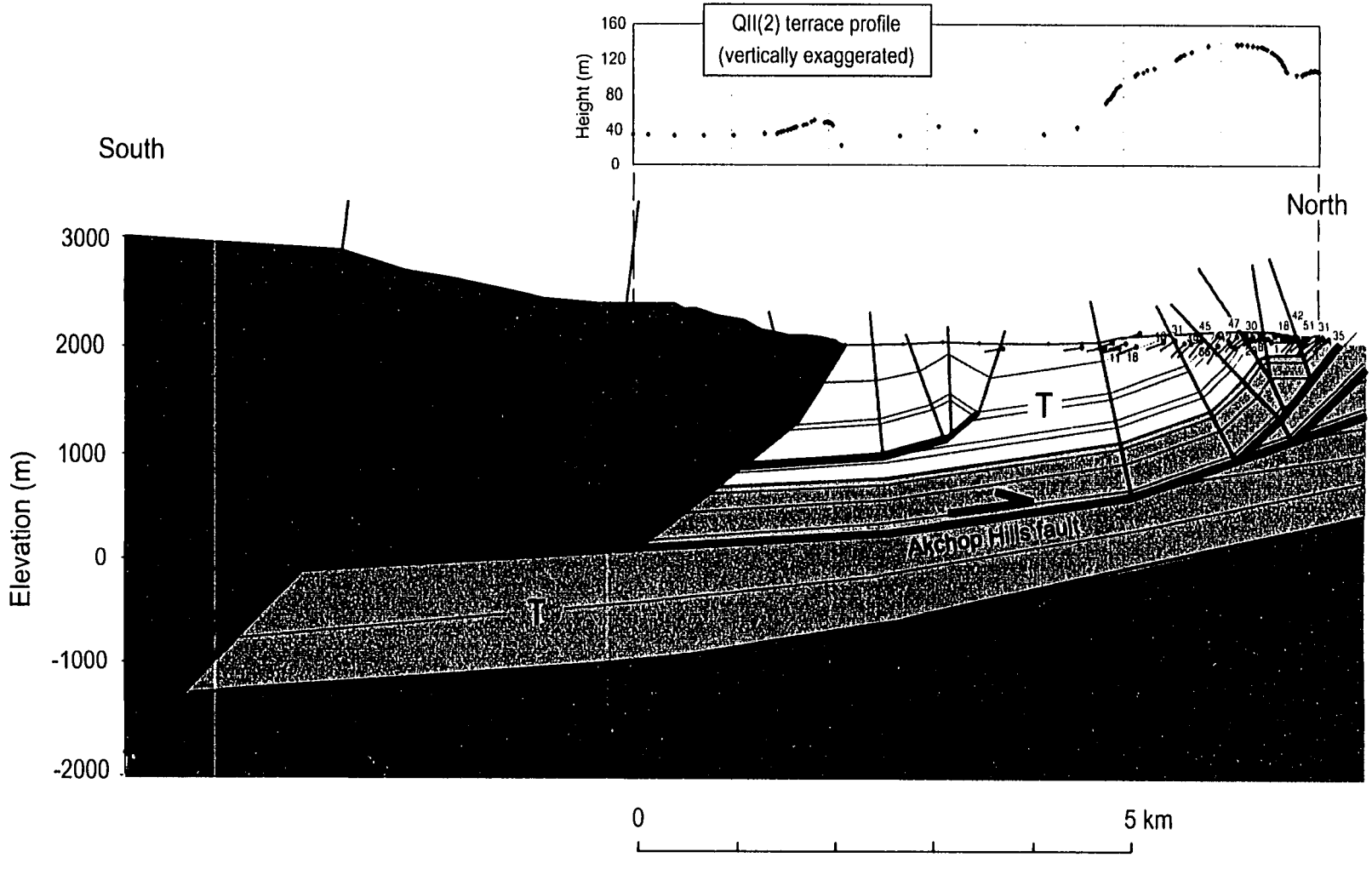

Figure 5.1: Geologic cross-section of the southern Kochkor basin near the Djuanarik River, showing the connection between the Akchop Hills and South Kochkor faults. The cross-section emphasizes the changing fault geometry, from low-angle flat-and-ramp-style faulting in the basin to a moderately dipping fault within the Paleozoic basement. The cross-section shows ~3 km of underthrusting of Tertiary sediment beneath the southern margin of the basin across a low-angle fault. The amount is equivalent to the minimum amount of shortening determined across the Akchop Hills fault. A vertically exaggerated profile of the QII(2) terrace shows that the vertical component of displacement is small for at least two kilometers south of the range front, consistent with the underlying low-angle fault.

a

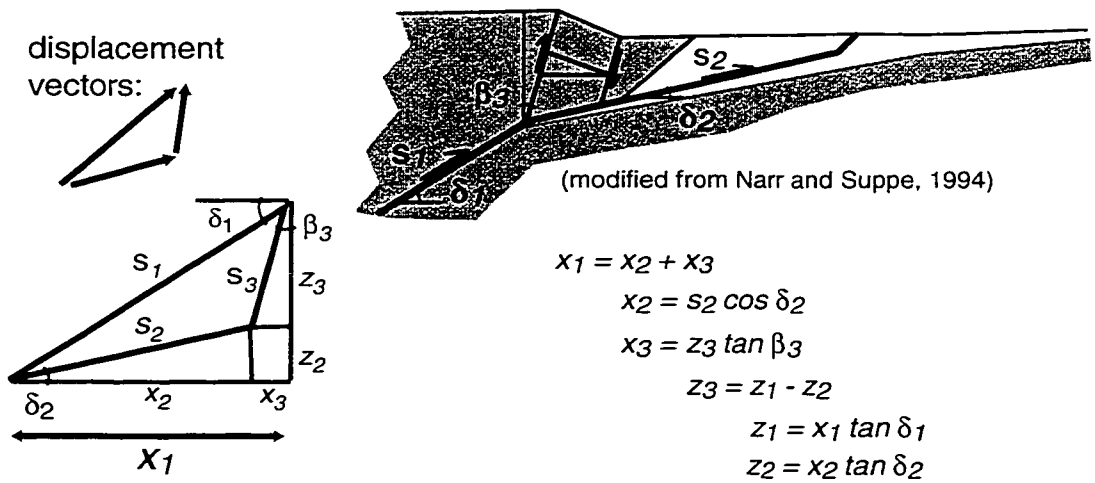

$$x_1 = x_2 + x_3$$
$$x_2 = s_2 \cos \delta_2$$
$$x_3 = z_3 \tan \beta_3$$
$$z_3 = z_1 - z_2$$
$$z_1 = x_1 \tan \delta_1$$
$$z_2 = x_2 \tan \delta_2$$

$$x_1 = s_2 \cos \delta_2 + (x_1 \tan \delta_1 - s_2 \cos \delta_2 \tan \delta_2) \tan \beta_3$$

$$x_1 = \frac{s_2 \cos \delta_2 (1 - \tan \delta_2 \tan \beta_3)}{1 - \tan \delta_1 \tan \beta_3}$$

if $\beta_3 = 0$,

$$x_1 = s_2 \cos \delta_2$$

b

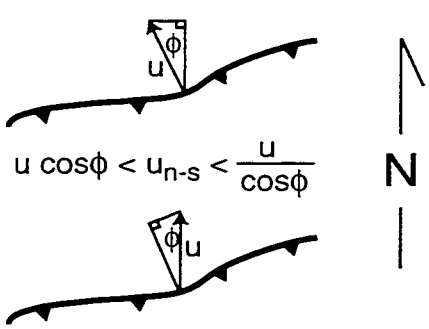

Figure 5.2: Conversion from fault dip slip to horizontal shortening. (a) Relationship between amount of horizontal shortening x_1 and slip s_2 on a shallow fault that dips at an angle δ_2. (b) North component of shortening rate $u_{n\text{-}s}$ constrained to between the pure dip-slip direction and due north-south.

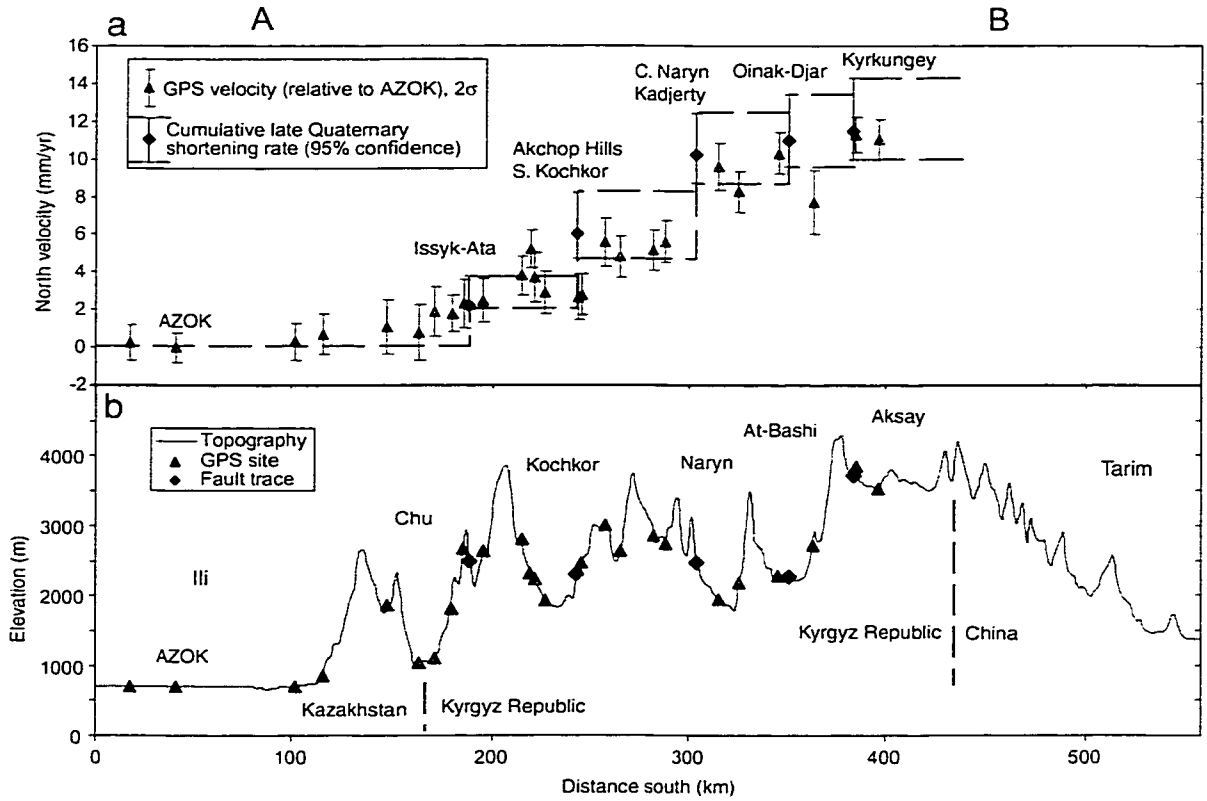

Figure 5.3: Comparison of geologic and geodetic shortening rates. Figure 4.18 shows the location of the profile line, GPS stations, and slip-rate sites. (a) Cumulative late Quaternary geologic shortening rates and current geodetic shortening rates (relative to station AZOK) along a north-south transect through the Kyrgyz Central Tien Shan. GPS velocities, showing 2σ ranges, are projected normal to the profile line A-B (data are courtesy of T. Herring, written communication, 2001). Shortening rates of faults inferred to intersect at shallow depths (for example, the Akchop Hills and South Kochkor faults) are combined, and are plotted at the appropriate range-front. The geologic data are projected along fault strike to line A-B. Dashed lines show the 95% minimum and maximum cumulative geologic shortening rate, with vertical jumps at the data points to indicate rigid blocks between fault zones. The two data sets show similar north velocities along the transect. (b) Vertically exaggerated topography across the transect. GPS sites projected onto the transect are shown to lie on the topographic profile. Major basins are labeled. The topography highlights the gradual southward increase in basin elevation and mean topography on the northern side of the belt, and the steeper topographic slope on the southern side of the belt.

Chapter 6

Paleoseismic evidence for average displacement and recurrence interval for faults in the central Tien Shan

6.1 Introduction

The rapidly deforming central Tien Shan offers an opportunity to examine the occurrence of large-magnitude earthquakes across a convergent mountain belt in a continental interior. The Tien Shan has experienced numerous $M > 7$ earthquakes in the 19th and 20th centuries (Figure 6.1) (summarized in Molnar and Ghose, 2000). Although some of the earthquakes occurred in intermontane basins, most events occurred near or along the northern and southern margins of the belt. Based on the historic distribution of large earthquakes, seismic hazard maps have assigned a greater hazard to the margins, despite the widespread late Cenozoic deformation (Medvedev, 1976; Kalmurzaev, 1979; Zonenshain and Savostin, 1979).

The distribution of late Quaternary slip rates shows that most shortening across the central Kyrgyz Tien Shan occurs on faults within the intermontane basins, and not near the northern margin (Chapter 4). These data suggest that the historical distribution of large earthquakes does not represent longer-term deformation, and that reliance on the historic earthquake record to assess earthquake hazard may be misleading. One possibility is that the intermontane regions were not densely populated during much of the last two centuries, and therefore large earthquakes that may have occurred were not recorded. Within uncertainties, however, the moment release during the historical large events is consistent with the ~20 mm/yr of shortening measured by GPS (Molnar and Ghose, 2000).

This chapter examines paleoseismic evidence for repeated earthquakes on three faults within the central Tien Shan, in order to estimate displacements and recurrence intervals. The data provide a kinematic description of how deformation may occur at timescales between the late Quaternary (10^5 to 10^6 yr) and present-day (10^1 yr, as measured by GPS). A more accurate description of the earthquake cycle on individual faults improves the ability to simulate the

relationship between permanent strain—measured by geology—and interseismic strain—measured by GPS (e.g., Hager et al., 1999). A secondary goal of this chapter is to estimate the recurrence rate for large earthquakes in the central Kyrgyz Tien Shan. The preliminary estimate—based on paleoseismic and slip-rate data—provides a framework for assessing earthquake hazards to the region as well as a measure of expected frequency of large earthquakes to compare with the historical record.

Paleoseismic evidence comes from trenching and profiling across the Issyk-Ata fault at the seismically active northern front and across the Kadjerty and Oinak-Djar faults within the interior of the belt. Each of the sites has been introduced previously in Chapter 4. Trenches excavated across the Issyk-Ata fault at the Sokuluk River valley and across the Oinak-Djar fault in At-Bashi basin were strung with a 1 m grid and logged on gridded mylar at a scale close to 1:20 (1 inch = 50 cm).

6.2 Sokuluk fan trench site, Chu basin

The north-vergent Issyk-Ata fault defines the northern deformation front of the Kyrgyz Tien Shan along the central and western portion of its length (section 4.1). The western portion of the fault, extending from the Aksu River to the east side of the Sokuluk River valley, is associated with a clear fault scarp and absence of a hanging-wall syncline (Figure 4.1). The 1885 $M \approx 6.9$ Byelovoda earthquake ruptured the surface for 20 km along the western portion of the fault, and reportedly formed a 1–2 m-high scarp across the Sokuluk River QIII(2) fan (Ignatiev, 1886). Prior events are clearly implied by the > 6 m height of the scarp across the alluvial fan (section 4.1.2). We investigated the displacement and timing of surface-rupture events on the Issyk-Ata fault with a topographic survey of the mouth of a small drainage that has developed within the uplifted hanging wall, and an excavation across the fault scarp adjacent to the mouth.

6.2.1 Topographic profiles

A detailed topographic map of the site shows the displaced QIII(2) fan surface, a broad drainage floor, and narrow inset terraces close to the fault scarp (Figure 6.2). A topographic profile along the faulted QIII(2) fan surface shows a total vertical separation of ~6.3 m (Profile A

in Figure 6.3). A profile of the drainage floor (Profile D) and the most narrow inset terrace (Profile C) shows 1.5 m of vertical separation between the hanging wall and a small fan in the footwall near the scarp (Figures 6.2 and 6.3). I presume that the 1.5 m vertical separation formed during the 1885 event (Ignatiev, 1886). The "1885" terrace merges the drainage floor about 20 m upstream (Figure 6.2).

The next-highest inset terrace in the hanging wall above the drainage floor has a vertical separation of ~3.0 m above the QIII(2) fan surface in the footwall (Profile B, Figures 6.2 and 6.3). This offset probably records the 1885 earthquake and the penultimate event. Although the "penultimate event" terrace tread is limited to ~20 m in length, the terrace surface projects to the drainage floor about 50 m south of the fault scarp, implying a continuous drainage floor prior to the penultimate event. Thus the steps in the profile of the present drainage floor apparently represent headward migration of a knickpoint related to discrete earthquakes. The height of the knickpoint step between the 1885 drainage floor and the penultimate event drainage floor, however, is less than the inferred ~1.5 m vertical offset during the penultimate event. To be internally consistent, these observations require that the small fan north of the drainage floor was constructed after the penultimate event but before the 1885 event.

A narrow, inset "QIV(1)" terrace located ~ 50 m south of the fault is about half the distance between the present drainage floor and the QIII(2) fan surface (Figures 6.2 and 6.3). It is not clear whether this terrace records the ante-penultimate event, or its formation (i.e., past incision of the ephemeral stream) was influenced by past climatic changes. The vertical separation of the QIV(1) terrace above the fan footwall is ~4.5 m, thus suggesting another ~1.5 m vertical displacement.

6.2.2 Trench structure and stratigraphy

The trench was excavated across the margin of the small fan north of the internal drainage (Figure 6.2). The trench wall exposes a single fault trace dipping 25–26°S that places gently folded alluvial gravel in the hanging wall over a series of fine-grained colluvial and gravelly alluvial units in the footwall (Figure 6.4). As the trench did not cross the entire scarp of the QIII(2) fan, the trench wall does not record the total displacement of the QIII(2) fan. I will next

describe the units in the trench before addressing the age control and evidence for paleo earthquakes.

The oldest exposed stratigraphic unit is a stratified and locally imbricated, pebble- to cobble-size gravel with a coarse sand matrix (Figure 6.4, unit 10). Cobble imbrication suggest a northerly flow of the river, indicating that the sediments were deposited during aggradation of the QIII(2) fan. Unit 10 was exposed in the hanging wall and the footwall.

A ~25 cm-thick silt to silty-sand deposit overlies unit 10 in the footwall (unit 20, Figure 6.4). The unit contains rare rounded pebbles that are more abundant in the lower ~10 cm. Ped faces and pores have $CaCO_3$ coatings. A silt to fine-sand deposit with similar clast content and $CaCO_3$ coatings is mapped in the hanging wall of the trench as unit 20. Because the hanging wall exposes the scarp face, however, this part of unit 20 may have been partially reworked. In a sample pit excavated ~20 m southwest of the northern end of the trench, on the fan surface, ~1.6 m of silt and fine sand with minor clasts and coarse sand overlies river terrace gravel (Figure 6.4b). Sediments in the pit showed evidence of bioturbation, particularly in the upper ~70 cm. Unit 20 probably comprises overbank deposits associated with the original QIII(2) fan construction, overlain by loess, and locally stirred by bioturbation.

Four alluvial units (units 30, 50, 53 and 55) exposed in the footwall reflect deposition from the ephemeral drainage adjacent to the trench (Figure 6.4). These alluvial deposits are supported by pebble- to cobble-sized clasts with coarse sand matrix. Wavy lower contacts show evidence for channel scour. The reddish hue (iron oxide stains?) of the matrix and the lack of well imbricated gravel distinguishes the four units from the gray sand in the matrix of unit 10. Unit 70 similarly has abundant gravel and a wavy lower contact, although the unit is supported by a silt to coarse sand matrix.

The trench wall exposes two similar colluvial deposits consisting of sand and silt colluvium with rare gravel clasts and coarse sand lenses (units 40 and 60, Figure 6.4). The units form a single, massive colluvial deposit close to the scarp. We did not detect the presence of former

long-lived land surfaces within either unit. The matrix of both deposits reacts mildly to dilute HCl, possibly indicating buried calcium carbonate (Bk) soil horizons.

Colluvium of unit 80 (Figure 6.4) can be distinguished from the older overlying units 60 and 70 by differences in matrix color (unit 80 = brown; unit 60, 70 = yellowish brown) and a difference in carbonate content (unit 80 does not effervesce with dilute HCl; unit 60 is moderately reactive). The uppermost part of unit 60 lacks a noticeable change in color or consistency that would indicate soil formation below a former land surface. Unit 80 contains a soil consisting of an A/Bw/Cox profile that is buried at its southern end by colluvium (units 100 and 110, Figure 6.4). Unit 100 contains mostly gravel with a coarse sand matrix, but has minor silt and sand matrix, unlike underlying unit 10. Unit 110 is distinguishable from the laterally continuous and underlying unit 20 because it has a looser, more friable consistency and it does not react strongly to HCl, indicating less $CaCO_3$.

6.2.3 Age control

Radiocarbon ages of snail shells and bone, and an IRSL age of silt capping the fan on the hanging wall, limit the age of the QIII(2) surface and younger deposits in the trench (Figure 6.4 and Table 6.1). No charcoal was found in the trench walls or in a pit excavated 20 m southwest of the trench. The broad spectrum of shell ages, from ~15.8 to ~3.3 x 10^3 cal yr B.P (Figure 6.4 and Table 6.1) does not show stratigraphic consistency, presumably because 1) land-snail shells burrow during winter hibernation (Zhou, 1999), incorporating younger snails in older deposits, and 2) shells in fine-grained scarp-derived colluvium may survive reworking after earthquake rupture (Lozek, 1990). Other potential problems with radiocarbon dating of snail shells include incorporation of inorganic carbon during shell growth (Goodfriend, 1987) and post-depositional mineral alteration. Although carbonate rock is absent in the Sokuluk River drainage, XRD analysis of the silt in unit 20 indicates abundant calcite, probably due to carbonate source regions of loess (J. Hinthorne, written communication, 2000). Ingestion of ancient carbon can produce anomalously old shell ages by several thousand years (Zhou, 1999 #184; Goodfriend, 1987 #182). Prior to radiocarbon dating, I mechanically cleaned the shells and lightly leached them in acid to remove exotic carbonate. XRD analyses of the cleaned snail shells indicate aragonite composition (J. Hinthorne, written communication, 2000). Although none was apparent, Calcite

present in the shell material would indicate secondary alteration of primary aragonite and possible incorporation of young or old carbon.

If there is no contamination by ancient carbon in the shells, the oldest shell age provides a minimum age for abandonment of the fan surface. The oldest shell, collected from near the top of unit 60, has a calibrated radiocarbon age of 14.4–15.8 x 10^3 cal yr B.P. (Figure 6.4 and Table 6.1). This age is consistent with the assumption that terraces designated QIII(2) regionally formed between 13.5–15.7 x 10^3 cal yr B.P. (Chapter 2; Figure 2.4).

Samples for IRSL dating were collected from the pit excavated in the hanging wall of the terrace (Figure 6.4b). Silt from ~50 cm above the contact with river gravel yielded an IRSL age 21.6 ± 0.9 ka (Table 6.2), ~6000 years older than the radiocarbon ages. The sample material—a mixture of eolian and fluvial deposits—may not have been completely "bleached" by exposure to sunlight prior to deposition; such partial bleaching would result in an anomalously old age (Little et al., 1998). Alternatively, the IRSL age may date the QIII(2) alluvial fan in the Sokuluk River drainage, in which case the fan was abandoned several thousand years before the QIII(2) and QIII(3) terraces were incised elsewhere (Figure 2.3).

A mammal bone in unit 70 gave a calibrated radiocarbon age of 2.3–2.7 x 10^3 cal yr B.P. (Table 6.1), which provides a maximum age for overlying unit 80 (Figure 6.4). Two shell ages at the base of unit 80, however, date to 3.3–3.9 x 10^3 cal yr B.P. These shells may have been reworked, similar to the shells in unit 60. If the two shells at the base of unit 80 formed early in the deposition of unit 80, however, they must have incorporated enough ancient carbon to make them at least 600–1600 yr older than the unit. This discordance resembles the age offset found elsewhere in shells (Goodfriend, 1987; Zhou, 1999).

6.2.4 Evidence for earthquakes

Offset terraces in the small drainage are consistent with four events each producing a vertical offset of ~1.5 m (Figure 6.3). The trench stratigraphy reveals evidence for at least three events, based on the number of individual scarp-derived colluvial wedges (e.g., Carver and McCalpin, 1996; Rubin et al., 1998). Burial of the Bw soil horizon on unit 80 by reworked alluvium and

colluvium in units 100 and 110 presumably resulted from scarp collapse during or soon after the 1885 earthquake (Figure 6.4). I restore 3.5 m of displacement from the 1885 event, based on the 1.5 m-high scarp and the 25° fault dip (Figure 6.5b and Figure 6.3). Although no buried soil was detected in unit 60, overlying unit 80 seems to represent scarp-derived colluvium generated from fault displacement during the penultimate event. The lack of a coarse facies close to the fault is curious and indicates that perhaps most scarp-derived material consisted of the overlying colluvium. An alternative possibility is that fine-grained eolian deposits accumulated against the scarp (R. Weldon, written communication, 2001). The scarp-derived colluvium from the 1885 event also lacks a gravel facies in the footwall projection of the fault. If deposition of unit 80 coincided with the penultimate earthquake, the earthquake would post-date the bone deposited in unit 70, or ~2.3–2.7 x 10^3 cal yr B.P. Figure 6.5c restores another 3.5 m of displacement, equal to the amount of slip during the 1885 event and consistent with the interpretation of the terrace profiles (Figure 6.3).

Evidence for prior events is less clear, as no clear unconformity is visible within the footwall stratigraphy to separate discrete scarp-derived deposits. At least one prior event must have occurred in order to create the relief necessary to deposit units 30–70. If so, this event had ~7–8 m of displacement in order to account for the total ~6.3 m vertical separation across the QIII(2) fan—perhaps an unreasonably large amount of displacement. The inset QIV(1) terrace, which may have formed as a result of base-level change following an earthquake, suggests there were two events prior to the penultimate event.

6.2.5 Summary

The profile and trench data indicate that two earthquakes with a similar ~3.5 m of displacement occurred within the last ~2.3–2.7 x 10^3 cal yr B.P. Although less clear, the vertical separation of the QIII(2) fan surface and the QIV(1) terrace suggest that there were a total of four events of similar displacement since ~15–21 ka. However, the data are consistent with only three earthquakes, and there is no evidence to rule out more than four earthquakes. Although the repeat time between the penultimate event and most recent event was ~2.5 ka, the average recurrence interval for four events is ~3.8–5.3 ka.

6.3 Oinak-Djar fault, At-Bashi basin

We excavated a trench across the Oinak-Djar fault in the western At-Bashi basin (Figure 4.13). Progressively offset fan surfaces in the hanging wall lie within a broad, grass-covered wash occupied by an ephemeral stream that begins in Tertiary siltstone, sandstone, and conglomerate. The trench extends across the fault scarp to the southern edge of a small, inset Holocene terrace in the hanging wall, and into an aggrading, lobate fan in the footwall (Figure 6.6).

6.3.1 Trench stratigraphy and radiocarbon dating

The trench exposed a well-bedded sequence of alluvium and collvium that record Holocene aggradation of the alluvial fan and occasional deformation by four faults (Figures 6.6 and 6.7). The oldest unit in the trench, exposed in the hanging wall, contains bedded, clast-supported alluvium with alternating coarse-sand and pea-gravel layers and cobble and small boulder layers (unit 10, Figure 6.7). Within the unit are discontinuous lenses of matrix-supported silty sand with cobble clasts. Overlying the alluvium are two massive fine-sand layers ~15–30 cm thick with rare cobble clasts (units 20 and 40), interstratified with a ~15 cm-thick coarse sand to cobble alluvium (unit 30). The units are clearly exposed in the hanging wall and are correlated to a similar sequence in the footwall, revealed in pits excavated into the trench floor (meter 7–8 and meter 10–11, Figure 6.7). Two charcoal samples collected from unit 20 in the hanging wall are dated at 9.6–10.2 and 10.2–10.5 x 10^3 cal yr B.P (Figure 6.7 and Table 6.1). A 1.2–1.5 m-thick unit of imbricated coarse-sand to cobble alluvium overlies unit 40 (unit 50).

The contact between unit 50 and the overlying unit 60 is marked by a ~5 cm-thick laminated silt that is continuous in the hanging wall but discontinuous in the footwall (Figure 6.7). The rest of unit 60 is a coarse sand and pea-gravel alluvium with cobble clasts, similar to some beds in underlying units 10 and 50. A charcoal sample collected from the basal laminar silt within the fault zone gave a calibrated radiocarbon date of 9.0–9.3 x 10^3 cal yr B.P (Figure 6.7 and Table 6.1). The basal laminar silt of unit 60 pinches out in the footwall, and because unit 60 is otherwise indistinguishable from unit 50, I draw the entire unit to terminate as well (meter 9, Figure 6.7). Overlying unit 60 is a poorly-sorted, matrix-supported, silt to medium-sand

colluvium with some pea-gravel clasts (unit 70, Figure 6.7). Cobble clasts are present within the lower ~15 cm of unit 70 across the fault zone, and the unit locally contains a cobble-rich layer (unit 75). Overlying unit 70 is a coarse sand to cobble alluvium with discontinuous ~2–5 cm-thick laminated silt layers (unit 80, Figure 6.7). Two charcoal samples collected from a layer of charcoal and reddish soil within a laminar silt at the base of unit 80 gave identical radiocarbon ages, which together correspond to 7.8–7.9 x 10^3 cal yr B.P (Figure 6.7 and Table 6.1). Unit 80 is absent in the hanging wall.

Overlying unit 80 is massive, wedge-shaped silt and fine- to medium-sand colluvium of unit 90 (Figure 6.7). Unit 90 contains ~20% pea gravel and rare cobbles. Two radiocarbon samples collected from the base and top of unit 90 indicate that this unit aggraded during the middle Holocene (Figure 6.7). The lower sample gave an age of 7.0–7.3 x 10^3 cal yr B.P. and the upper sample, collected 30 cm below the upper contact, gave an age of 3.5–3.7 x 10^3 cal yr B.P (Table 6.1). Because it is wedge-shaped and lacks overlying sandy gravel alluvium, unit 90 probably formed as the adjacent ephemeral stream incised unit 80. A stone line, mapped on the east trench wall, extends for at least 1.5 m south of the northernmost fault trace (Figure 6.7b). This stone line—which probably indicates a land surface (Ruhe, 1959)—marks the lower contact of unit 93, a colluvium that is otherwise identical to unit 90. The gently dipping lower contact of unit 93 is inferred on the western trench wall. Unit 100, the youngest deposit in the trench, extends across the scarp face. This unit is a fine-sand to silt colluvium with local coarse sand. The deposit is more friable, and contains more pea-gravel and small cobble clasts, than do underlying units 70, 90, and 95. Unit 100 coincides with an Ac soil horizon (R. Burke, personal communication, 1998).

6.3.2 Trench structure

The trench reveals evidence for multiple ruptures along four thrust faults (Figure 6.6b and Figure 6.7). Most displacement has occurred on the northern fault, labeled "D" in Figure 6.7, which dips 29°N. A wedge-shaped deposit of clast-supported sand, granule, and cobble gravel coinciding with fault D on the east wall (unit 95, Figure 6.7b) appears to be an injection feature (see, for example, Weber and Cotton, 1980, plate XIV, reproduced in Carver and McCalpin, 1996).

Although long profiles of the older terraces in the hanging wall show a ~6° S surface dip, a small terrace that ends at the north end of the trench has a flat 8.4° S dip, which I infer was close to the original depositional slope for units in the hanging wall (Figure 4.14). Close to fault D these units presently dip 16° S, indicating gentle anticlinal folding. Clast orientations and the upper and lower contacts of units 40 and 20 show evidence for drag folding within ~1 m of fault D. The footwall of fault D contains a syncline that has overturned units 60, 70, and 80 close to the fault. Thin seams of colluvium continuous with layer 20, and seams of alluvium and laminated silt associated with layer 60, are sheared beside traces of the fault in the hanging wall and footwall, respectively. The combination of brittle and ductile deformation is similar to that found in excavations across other thrust faults (Beanland and Barrow-Hurlbert, 1988; Meghraoui et al., 1988).

The three other faults in the footwall (faults A, B, and C) dip less steeply than fault D and have less total displacement (Figure 6.7). These faults displace units 50–80, and cut the lower part unit 90. Faults A–C show greater amounts of displacement across the bottom contact of unit 70 than the bottom contact of unit 80 (Figure 6.8). The greater displacement of the older unit suggests that faults A–C ruptured during at least two events, although it is possible that there was a large component of strike slip to the faults and the progressive offset is only apparent. For example, the apparent normal offset of the base of unit 80 across fault C may be due to oblique slip. Although most displacement has occurred by discrete slip on fault planes, steep or curved unit contacts between faults indicate a component of tilting and/or folding by distributed shear.

6.3.3 Evidence for earthquakes

The trench reveals evidence for two to four separate earthquakes, although more events are permissible. The most recent event likely occurred on fault D, which cuts unit 93 and produced the wedge-shaped unit 95 on the east trench wall (Figure 6.7). This event occurred after ~3.6 ka. Coarse material from unit 95 appears to reach the ground surface, although roots and a friable consistence indicate that unit 100 is an Ac horizon here. As the east wall of the trench is close to a wash that is heavily used by local herdsmen, I infer that most of the unit 100 has been eroded on the east side of the trench (Figure 6.6a). A line of stones at the base of unit 100 on the west wall is not cut by the fault (Figure 6.6b).

At least one prior event is suggested for fault D. If the lower contact of unit 93—defined by the stone line on the east trench wall—unconfomably overlies the overturned syncline in the footwall of fault D—visible on the west wall—then unit 93 likely represents a scarp-derived colluvial wedge deposited after an event that folded the footwall units (Figure 6.7). Unfortunately, the cross-cutting relationship for the two events before the most-recent event is not apparent on one trench wall. Evidence for the overturned syncline was ambiguous on the east trench wall, as we did not have time to carefully map it. Large channel-filled alluvial deposits cut out most of unit 70 in the footwall of fault D, which prevented a simple comparison of deformation across the trench. If the footwall syncline never occurred on the east trench wall (i.e., deformation was dramatically different along strike), it is permissible that no events prior to the most-recent event occurred on fault D.

The western trench wall contains evidence for two events on faults A–C (Figures 6.7 and 6.8). Each fault displaces the bottom of unit 70 more than the bottom of unit 80. Unless large amounts of lateral displacement produced the apparent offsets, the differences in offset require at least two distinct events. The earlier of these events occurred after deposition of unit 60, or after 9.0–9.3 x 10^3 cal yr B.P., and before deposition of unit 80, or before 7.7–7.9 x 10^3 cal yr B.P (Figure 6.7 and Table 6.1). The similar thickness of strata between unit 20 and the base of unit 60 in both the hanging wall and the footwall indicates that no events occurred during deposition of these units, or between ~10 and ~9 x 10^3 cal yr B.P.

The later event on faults A–C occurred after 7.7–7.9 x 10^3 cal yr B.P (Table 6.1). The faults offset the base of unit 80 about as much as they displace the base of unit 90 (Figure 6.8). Faults A–C could not be traced into unit 90 above the fault contacts with unit 80. The apparent upward termination of displacement may not indicate that most of unit 90 post-dates the later event on these faults, however, as fault displacement can terminate below the land surface (e.g., Bonilla and Lienkaemper, 1990). The evidence in the trench cannot place a firm upper bound on the timing of the later displacement episode on faults A–C.

The restorations of the Oinak-Djar fault trench illustrate interpretations of deformational style and magnitude of displacement along separate faults (Figure 6–9). They are not intended to

completely recreate rupture during distinct paleo-earthquakes. The first restoration considers the total deformation due to fault D (Figure 6.9a). The folding and displacement of the units across fault D are restored to an 8.4°S dip, consistent with the slope of a small inset terrace directly above the trench (Figures 4.14 and 6.6a). This restoration suggests ~4 m of fault displacement and hanging-wall folding. As discussed above, I infer that this slip occurred during one to three events.

Figure 6.9b restores the inferred depositional slope of unit 80, and requires ~3 m of slip along faults A–C. The original depositional slope is inferred to change from ~8° in the hanging wall to 5° in the footwall, which is the current slope of the fan surface and units in the footwall. The thin layer of unit 90 is a supposition, and represents a minimum thickness. The restoration shows units 70 and 80 changing thickness to smooth topography over a pre-existing scarp, seen in underlying unit 60.

The final restoration to pre-earthquake form of units 20–70 requires ~2 m of displacement on faults A–C (Figure 6.9c). The restored depositional slope of units 20 and 40 has a slightly steeper gradient than units 60 and 70. This difference is not enough to require a third event on faults A–C.

6.3.4 Summary

The Oinak-Djar fault trench shows evidence for at least two, and perhaps three or four earthquakes in the last ~10^4 cal yr B.P. Two unique events probably occurred on faults A–C. The minimum number of events—two—requires that the inferred contact between units 93 and the underlying overturned syncline is false, and restorations "a" and "b" in Figure 6.9 represent the same event. Three events, as illustrated in the three restorations of Figure 6.9, are also permissible if the cross-cutting relationship is false. If the inferred cross-cutting relationship is correct, two unique events occurred on fault D, and three or four events are likely. Three events are possible if fault D slipped after restorations "a" and "b", or "a" and "c", in Figure 6.9.

The total displacement across the trench is 9 m. The restorations of faults A–C suggest a minimum of 2–3 m of displacement per event. The range of average displacement per event, considering two and four events, is 4.5 to 2.3 m, respectively.

6.4 Kadjerty River, Naryn basin

The south-vergent Kadjerty fault parallels the northern margin of the Naryn basin and is one of two active faults that are inferred to intersect the Akchatash fault beneath the Moldo-Too Range (Figure 4.9). The fault can be traced almost continuously across river terraces from its eastern termination at the northeastern margin of the Naryn basin east of the Ottuk River to just west of the Kadjerty River. The Kadjerty fault probably continues at least 50 km farther west, although its trace is not apparent from remotely sensed images west of the Kadjerty River valley (section 4.3).

The Kadjerty fault has left a remarkable record of repeated late Quaternary earthquakes near the Kadjerty River, where it has displaced a series of river terraces that range in age from ~141 ka to late Holocene (Figures 6.10 and 6.11). The oldest terrace—unit QII(2)—has a vertical separation of ~65–90 m. The ~141 ka age of the QII(2) terrace is limited by four luminescence analyses on correlative terraces at other sites; two of the ages are from the QII(2) terrace at the Djergetal River, located ~13 km east (Figures 2.1 and 2.6; Table 2.2). To the west, the fault trace crosses the broad QIII(2) terrace, and is marked by a scarp that increases in height from 8 to 12 m from east to west (section 4.3.1). Detrital charcoal collected from the uppermost gravel and overlying silt and sand constrain the age of the QIII(2) terrace to ~ 14.1 x 10^3 cal yr B.P (Figure 2.3 and Table 2.1). Evidence for earthquake displacements come from vertical separations of faulted Holocene terraces inset to the QIII(2) terrace and estimates of the fault's dip.

The modern Kadjerty River has incised ~60–70 m into the paired QIII(2) terrace (Figure 6.11). At least two inset Holocene terraces—the QIV(2) and QIV(3) terraces—are cut by the Kadjerty fault (Figures 6.10 and 6.11). Two scarps cross the QIV(2) terrace that trend subparallel to the fault. I infer that both are fault scarps, one from each of two fault splays. A shallow trench excavated across the upper scarp, which strikes N63°E, exposed a single fault

plane that dips 13°N. Across the riser between the QIII(2) and QIV(2) terraces, however, the fault dips ~29 ± 5°N (section 4.3.1). The vertical separation across the upper and lower scarps, measured at the west end of the terrace tread where the scarps converge, is 5.5 ± 0.3 m (Figure 6.11). The location of the upper QIV(2) terrace scarp and the scarp across the inset QIV(3) terrace suggests a dip, indistinguishable from the dip determined at the riser between the QIV(2) and QIII(2) terraces.

The two youngest Holocene terraces within the nested sequence provide maximum estimates of displacement during individual earthquakes. The vertical separation across the QIV(3) terrace is 1.9 + 0.2/–0.1 m (Figure 6.11). The 31 ± 4°N dip of the fault beneath the QIV(3) terrace was estimated from the locations of the fault scarps above and below the riser between the QIV(2) and QIV(3) terraces. The apparent vertical separation across the QIV(4) terrace is ~0.9 m. It is possible that the scarp across the QIV(4) terrace is a terrace riser and is not a fault scarp. The grassy surface of the QIV(4) terrace in the hanging wall clearly distinguishes it from the active floodplain of the Kadjerty River. The inferred QIV(4) terrace in the footwall, however, has a height and cobbly surface that are similar to gravel bars within the active floodplain (Figure 6.10a). Although the location of the inferred QIV(4) terrace fault scarp is close to that of the QIV(3) terrace fault scarp, their relative locations require a ~2–5°N dip of the fault near the surface and an abrupt ~15° change in fault strike. Thus, the ~1.9 m-high scarp across the QIV(3) terrace provides an upper bound on the maximum displacement during the most recent earthquake. The ~0.9 m-high scarp across the QIV(4) terrace, however, may have formed in the most recent event, and the scarp may have been modified by the river.

The estimated ~31°N fault dip and the ~1.9 m-high scarp across the QIV(3) terrace suggest 3.7 ± 0.5 m of dip-slip displacement. If the QIV(4) terrace is cut by the fault, this displacement may have been produced by a maximum of two events. The ~31°N dip and the ~5.5 m-high scarp across the QIV(2) scarp suggest a 11.1 +1.7/–1.3 m displacement, corresponding to three earthquakes each with ~3.7 m of displacement. The 12 m-high QIII(2) scarp was produced by ~24.5 m displacement, which implies six or seven such events since the terrace formed ~14.1 x 10^3 cal yr B.P. These arguments, which assume characteristic earthquake behavior as defined by Schwartz and Coppersmith (1984), imply a maximum average recurrence interval of ~2000–2400

years. If the QIV(3) scarp was instead produced by two events with ~1.9 m of displacement, about thirteen such characteristic events would have deformed the QIII(2) terrace with an average recurrence of ~1100 years.

6.5 Summary of average displacement, recurrence interval, and magnitude for large earthquakes.

The paleoseismic data from the Issyk-Ata, Oinak-Djar, and Kadjerty faults are consistent with periodic ground-rupturing events with ~2–4 m of displacement, and an average recurrence interval of about 1000 to 5000 years. However, the data permit both smaller and larger events, and obviously are incapable of discriminating paleoearthquakes that did not produce surface rupture. The stratigraphic evidence used to identify separate earthquakes would not distinguish events that are either small or recur over a short time interval. Many historic large thrust and reverse fault earthquakes in the Tien Shan did not rupture the ground surface, or produced surface rupture that was much shorter than the subsurface rupture length (Ghose et al., 1997; Molnar and Ghose, 2000). Although the earthquake record is preserved inadequately in the trench and terrace stratigraphy, the evidence in the paleoseismic and the historic records for ~2–4 m events justifies exploring the hypothesis that such events recurred characteristically.

6.5.1 Comparison with historical events

The trench across the Issyk-Ata fault in the Sokuluk River valley revealed evidence for 3.5 m of displacement during the 1885 Byelovoda earthquake, which produced a ~20 km-long surface rupture (Ignatiev, 1886). The estimated magnitude for this event—based on intensity—is $M = 6.9 \pm 0.5$ (Kondorskaya and Shebalin, 1977). The ~3.5 m displacement measured at the trench may indicate that previous workers underestimated the magnitude of this event, or that the displacement measured at this point was much greater than the average displacement on the fault.

The 1992 $M_s = 7.3$ Suusamyr earthquake was the most recent large earthquake to occur in the Kyrgyz Tien Shan (Ghose et al., 1997; Mellors et al., 1997). The aftershock distributions suggests that an area ~23 km wide and ~50 km long ruptured along a fault dipping ~50°S (Mellors et al., 1997). However, only ~4 km of total surface rupture occurred during the event,

indicating that most of the fault displacement, at least locally, transferred into growth of the Chet-Korumdy ridge (Ghose et al., 1997). The maximum displacement measured along the shorter "eastern" surface rupture was 4.2 m. The ~3.4 km-long "western" surface rupture consisted of three distinct sections that indicated vertical offsets of ~1.8 to 0.8 m.

6.5.2 Estimated magnitudes of paleo-earthquakes

The maximum displacement and the scarp heights produced during the 1992 Suusamyr earthquake are similar to the estimates and observations for past events inferred on the Issyk-Ata, Kadjerty, and Oinak-Djar faults. Thus, analogy indicates that $M \approx 7.3$ events occurred in the past on each of these faults.

Paleo-earthquake magnitudes are frequently estimated by comparing inferred rupture parameters—surface rupture length, maximum and average surface displacement—to measured rupture parameters after historical ground-rupturing earthquakes of known magnitude (e.g., Wells and Coppersmith, 1994). Although I do it anyway, the application of these empirical regressions to the data collected in this study is problematic for several reasons. First, although the data presented above estimate paleo-earthquake displacement, magnitude-*displacement* regressions using the subset of reverse faults in the Wells and Coppersmith compilation are *not* significant at the 95% confidence level (Wells and Coppersmith, 1994). Second, only a single location on each fault has an estimate of displacement. As shown from the Suusamyr event (Ghose et al., 1997), displacement frequently varies by a factor of two or greater along a surface rupture length (see also Carver and McCalpin, 1996; McGill and Rubin, 1999), and five to ten measurements of surface displacement are required to get good precision from empirical regressions (Hemphill-Haley and Weldon, 1999). Third, although the regression between surface *rupture length* and magnitude *is* significant at the 95% confidence level (Wells and Coppersmith, 1994), I lack appropriate data for paleo-earthquake rupture lengths. Although discontinuities in fault trace, changes in fault orientation, and intersections of active folds or faults may act as potential barriers to earthquake rupture, growing evidence shows that estimations of paleo-rupture lengths based on "geologic" or "geometric" segments are unreliable (e.g., McCalpin, 1996; Rubin, 1996; Hemphill-Haley and Weldon, 1999).

Caveats notwithstanding, the empirical regression using the entire Wells and Coppersmith (1994) catalog suggests that an average surface displacement of 2–4 m is consistent with $M_w \approx$ 7.2–7.4 events, and a maximum surface displacement of 2–4 m is consistent with $M_w \approx$ 6.9–7.1 events. Previous investigations indicate that paleoseismic investigations are more likely to select from sites that are close to average or maximum displacement, where features of the events are preserved (Carver and McCalpin, 1996; Hemphill-Haley and Weldon, 1999). The $M_w \approx$ 6.9–7.4 range encompasses the moment magnitudes estimated by Molnar and Ghose (2000) for the 1885 Byelovoda and 1992 Suusamyr earthquakes.

6.6 Recurrence interval of M ~6.9–7.4 earthquakes in the Central Tien Shan

To estimate the average repeat time of large earthquakes in the central Kyrgyz Tien Shan, I assume that the active faults such as those studied in Chapter 4 follow a characteristic earthquake distribution (e.g., Wesnousky, 1994), and assume that most elastic strain in the upper crust is released during 2–4 m events of $M \approx$ 6.9–7.4. I do not consider larger events in this estimation, even though the 1911 $M \approx 7.8$ Chon-Kemin earthquake clearly showed that they do occur in the central Tien Shan. I restrict the analysis to the faults shown on Figure 4.18. Empirical relations between rupture length and moment magnitude, using the Wells and Coppersmith (1994) catalog of reverse-slip events, suggests that **M** = 6.9–7.4 events produce subsurface rupture lengths of 49–65 km. This regression predicts that **M** = 7.3 events produce 61 km-long subsurface ruptures, which is close to the ~50 km-long subsurface rupture length estimated for the 1992 Suusamyr event (Mellors et al., 1997), and is certainly sufficient for this simple exercise.

I divided the lengths of the faults shown in Figure 4.18 into 16 sections between ~50–65 km long (Figure 6.12), and assume that each section ruptures independently. A single section covers most surface traces of faults within the intermontane region. For longer faults, I chose section boundaries based on distances from fault ends or based on changes in structural style. Rupture sources include the faults that broke during the 1992 Suusamyr and 1911 Chon-Kemin earthquakes, although the ruptures from those events extended outside the study area. I assigned each fault section a slip rate, u. For fault sections with a measured slip rate, the slip-rate probability distribution from Chapter 4 describes u. For other fault sections I assumed a value

for u based on slip rates along strike and ± 1 mm/yr uncertainty (Figure 6.12). For a section of the Talas-Ferghana fault I assumed a slip rate of 5–10 mm/yr, based on previous work (Trifonov et al., 1992; Burtman et al., 1996) and recent geodetic estimates (B. Meade, personal communication, 2000). Along each of the n fault sections, I assumed that all slip occurs in earthquakes with a displacement s: 2 m < s < 4 m. The earthquake recurrence, R, is

$$R = \sum_{i=1}^{n} \frac{u_i}{s_i} \tag{15}$$

and the recurrence interval T is simply $1/R$. A Monte Carlo simulation determined uncertainties. Slip-rate probability distributions are either empirical (i.e., from Chapter 4), gaussian (the assumed values of $u \pm 1$ mm/yr) or uniformly distributed (for the Talas-Ferghana fault). Values of displacement were drawn from a uniform probability distribution.

The result predicts that an event of $M \approx 6.9$–7.4 occurs every 60-70 years in the study area (Figure 6.12). Historically, three ground-rupturing events have occurred in the study area since 1885, and no prior major events are reported for the area during the 19th century. Thus, at first glance, the predicted recurrence rate of large earthquakes appears compatible with the historical seismicity. However, the sparsely populated intermontane region suggests that the written record there is probably much shorter and less complete than the record along the more densely populated northern margin.

Table 6.1: Radiocarbon and calibrated ages of paleoseismic trench samples.

Sample name	Lab code[a] (CAMS #)	Trench	Unit	material	$\delta^{13}C$[c] (per mil)	Radiocarbon age[d,e] (^{14}C yr B.P.)	Calibrated age range[f] (cal yr B.P.; 95.4%)	Area[g]
99/Sokuluk/35	57609	'99 Sokuluk	40/60	shell	-8	10,470 ± 50	12,840 - 12,270	0.851
							12,260 - 12,090	0.135
							12,000 - 11,970	0.014
99/Sokuluk/39	57610	'99 Sokuluk	40/60	shell	-8	9350 ± 50	10,730 - 10,720	0.007
							10,690 - 10,400	0.990
							10,310 - 10,290	0.002
99/Sokuluk/10a	57616	'99 Sokuluk	40/60	shell	-8	10,870 ± 50	13,120 - 12,810	0.861
							12,730 - 12,650	0.139
99/Sokuluk/22	57617	'99 Sokuluk	40/60	shell	-8	8720 ± 50	9890 - 9840	0.100
							9830 - 9550	0.900
99/Sokuluk/18	57614	'99 Sokuluk	40/60	shell	-8	8430 ± 60	9530 - 9400	0.798
							9390 - 9280	0.202
99/Sokuluk/25	57611	'99 Sokuluk	40/60	shell	-8	10,950 ± 50	13,150 - 12,840	0.942
							12,720 - 12,670	0.058
99/Sokuluk/16	57615	'99 Sokuluk	40/60	shell	-8	12,770 ± 50	15,750 - 14,390	1
SCT/062399/1	59762	'99 Sokuluk	70	bone[i]	-20	2410 ± 50	2710 - 2560	0.329
							2540 - 2340	0.970
99/Sokuluk/12	57612	'99 Sokuluk	80	shell	-8	3180 ± 40	3470 - 3340	0.985
							3280 - 3270	0.015
99/Sokuluk/1	57613	'99 Sokuluk	80	shell	-8	3530 ± 40	3960 - 3950	0.003
							3910 - 3690	0.997
98/Odjr/8	51039	'98 Oinak-Djar	20	charcoal	-25	8790 ± 40	10,150 - 9990	0.087
							9940 - 9660	0.889
							9650 - 9600	0.024
98/Odjr/104	51040	'98 Oinak-Djar	20	charcoal	-25	9140 ± 50	10,470 - 10,460	0.024
							10,430 - 10,210	0.976

Table 6.1: Radiocarbon and calibrated ages of paleoseismic trench samples (continued).

Sample name	Lab code[a] (CAMS #)	Trench	Unit[b]	material	$\delta^{13}C$[c] (per mil)	Radiocarbon age[d,e] (^{14}C yr B.P.)	Calibrated age range[f] (cal yr B.P.; 95.4%)	Area[g]
98/Odjr/100	51044	'98 Oinak-Djar	60	charcoal	-25	8180 ± 50	9400 - 9360	0.007
							9280 - 9010	0.993
98/Odjr/5	51042	'98 Oinak-Djar	80	charcoal	-25	7010 ± 50		
98/Odjr/6	51043	'98 Oinak-Djar	80	charcoal	-25	7030 ± 40		
	pooled mean, standard deviation[h]		(T'=0.08; χ^2(0.05)=3.84)			7022 ± 34	7930 - 7890	0.291
							7880 - 7790	0.645
							7780 - 7760	0.063
98/Odjr/14	51160	'98 Oinak-Djar	90	charcoal	-25	6290 ± 40	7310 - 7160	0.866
							7120 - 7030	0.134
98/Odjr/13	51045	'98 Oinak-Djar	90	charcoal	-25	3340 ± 50	3690 - 3650	0.085
							3650 - 3470	0.915

[a] Samples run at Center for Accelerator Mass Spectrometry, Lawrence Livermore National Labs.

[b] See Figures 6.4 and 6.7

[c] $\delta^{13}C$ values are assumed according to Stuiver and Polach (1977).

[d] The quoted age is in radiocarbon years using the Libby half life of 5568 years and following the conventions of Stuiver and Polach (1977).

[e] Sample preparation backgrounds have been subtracted, based on measurements of samples of 14C-free coal and limestone. Backgrounds were scaled relative to sample size.

[f] Calibration using CALIB v 4.3 (Stuiver and Reimer, 1993) and the calibration dataset in Stuiver et al. (1998)

[g] Relative area under the probability distribution that lies within the 95% confidence limits.

[h] Calibration of pooled radiocarbon ages described in CALIB manual. T' = test statistic; T' $<\chi^2$ if not statistically different at 95% confidence.

[i] Bone sample prepared according to the method of Brown et al. (1988).

Table 6.2: IRSL data for the QIII(2) Sokuluk River fan.

Sample code Lab number [a,b]	Dose rate [c] ±1σ (Gy/ka)	Preheat [d]	Bleach [e]	Equivalent dose [f], ±1σ (Gy)	Time[g] (s)	Age [h] ±1σ (ka)	Location	Material; thickness of deposit (m) Height above gravel (m)
SCT/060899	4.21±0.11	140°C/2d	780/2h	73.9±2.1	1-55		Sokuluk R.,	Silt; 1.6
TIEN99-4		160°C/2d	780/2h	90.8±3.0	1-50	21.57±0.92	Chu basin	0.30

[a]Sample preparation and measurements at the Desert Research Institute, Reno, Nevada.
[b]Polymineralic, non-carbonate, detrital 4-11 μm diameter size fraction was used. Luminescence was detected at the 420±20 nm spectral region (bandpass 390-470 nm at 1% cut). Laboratory sample-preparation procedures follow Berger (1990).
[c]Effective dose rate, D_R, is derived from independent measurements of U, Th, K and water concentration. D_R is calculated with the conversion factors and equations given by Berger (1988), and includes a cosmic ray component varying from 0.03 to 0.17 with estimated average depth, from the data of Prescott and Hutton (1988).
[d]The chosen pre-readout heating and duration (days) (to empty laboratory-filled electron traps). Pre-heating was applied after bleaching.
[e]Bleaching protocol (FSL = full solar spectrum at Reno; 400 = laboratory Hg-vapor lamp with 400-750 nm passed; 780 = > 780 nm solar spectrum passed), and duration (hours or days)
[f]Weighted mean equivalent dose plus average error over time/temperature interval in the next column. A weighted-saturating-exponential regression and error model (Berger et al., 1987) was employed. For some IRSL samples, inter-aliquot scatter was minimized by short-shine normalization (to natural signals) (Ollerhead et al., 1994). The difference in equivalent dose suggests that the higher pretreatment temperature is more stable, and the corresponding equivalent dose is used in the age calculation.
[g]The readout (LED-on) time interval for which equivalent dose is calculated.
[h]Luminescence age t = Equivalent dose / Dose rate.

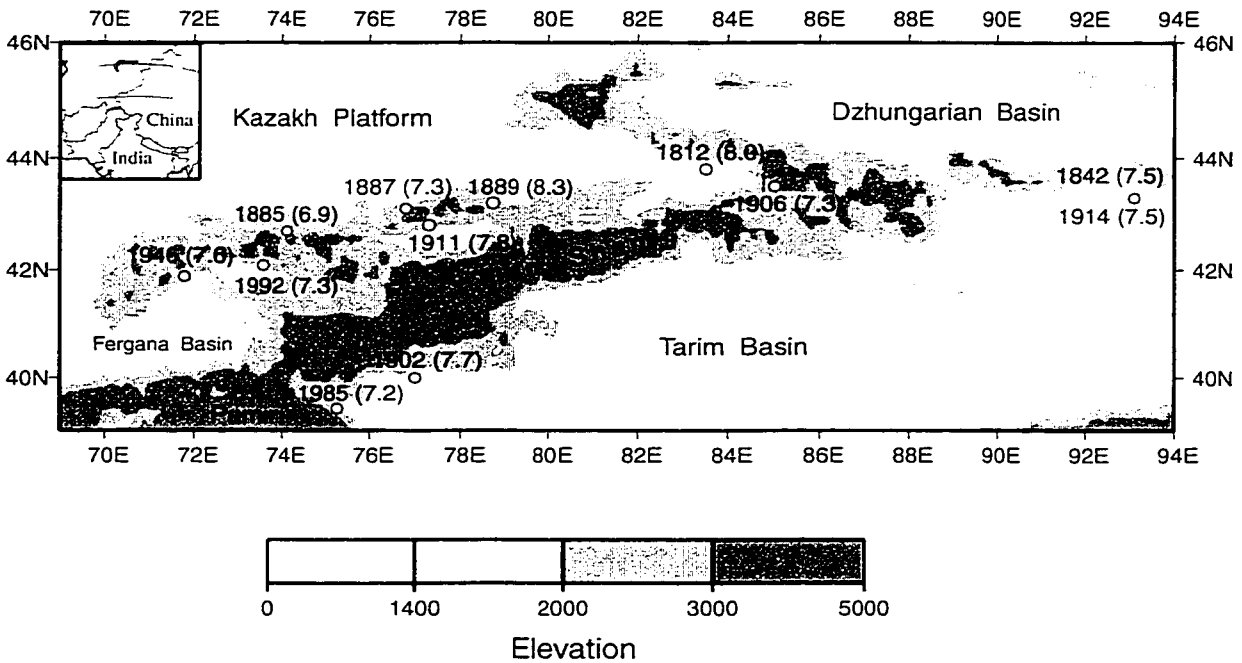

Figure 6.1: Major historic earthquakes in the Tien Shan (Modified from Molnar and Ghose, 2000). The year and estimated moment magnitudes are shown next to the locations, which are indicated by white circles.

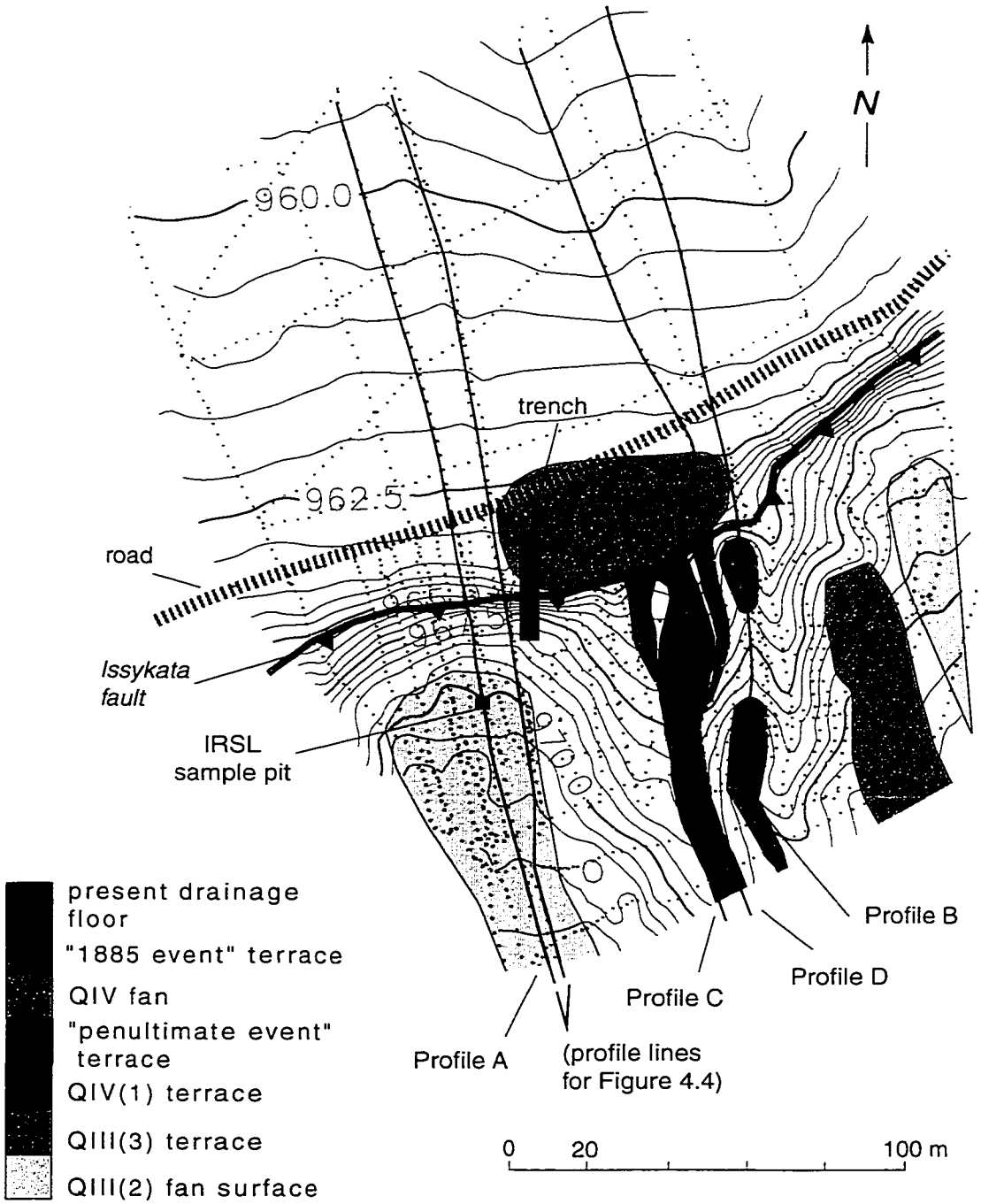

Figure 6.2: Topographic map of the Sokuluk River paleoseismic site on the Issykata fault. Location of the site is indicated in Figure 4.1. The map shows the trench, profile lines, IRSL sample pit, and terraces within the internal drainage of the QIII(2) fan. Profiles A-D appear in Figure 6.3. Grey dots indicate surveyed points using kinematic differential GPS. Contour interval is 0.5 m.

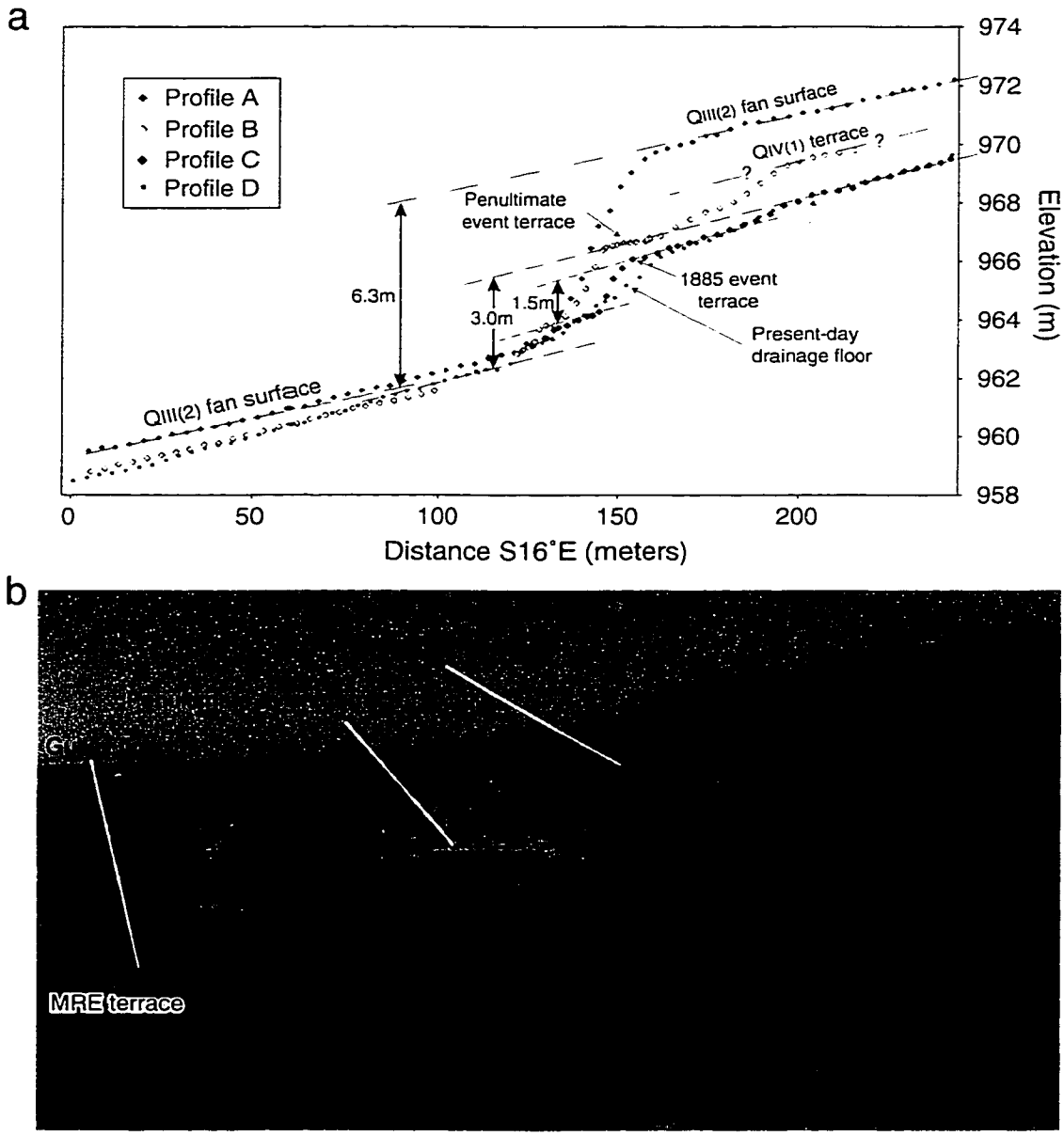

Figure 6.3: Profiles and photo of the terraces within the small drainage. (a) Profiles of terrace surfaces (locations of profiles are shown in Figure 6.2). The 1.5 m-high scarp across the youngest inset terrace was produced by the 1885 earthquake. A higher inset terrace preserved close to the scarp is offset by 3.0 m above the QIII(2) fan surface; this terrace projects to the floor of the drainage ~50 m south of the scarp, indicating a possible paleo– drainage floor prior to the penultimate event. Total vertical separation of 6.3 m of the QIII(2) fan was perhaps caused by four "1885-type" events that produced 1.5 m-high scarps. (b) Photo looking east across the internal drainage in the QIII(2) fan. Person holding GPS antenna is at the top of the fault scarp on the "penultimate event" terrace.

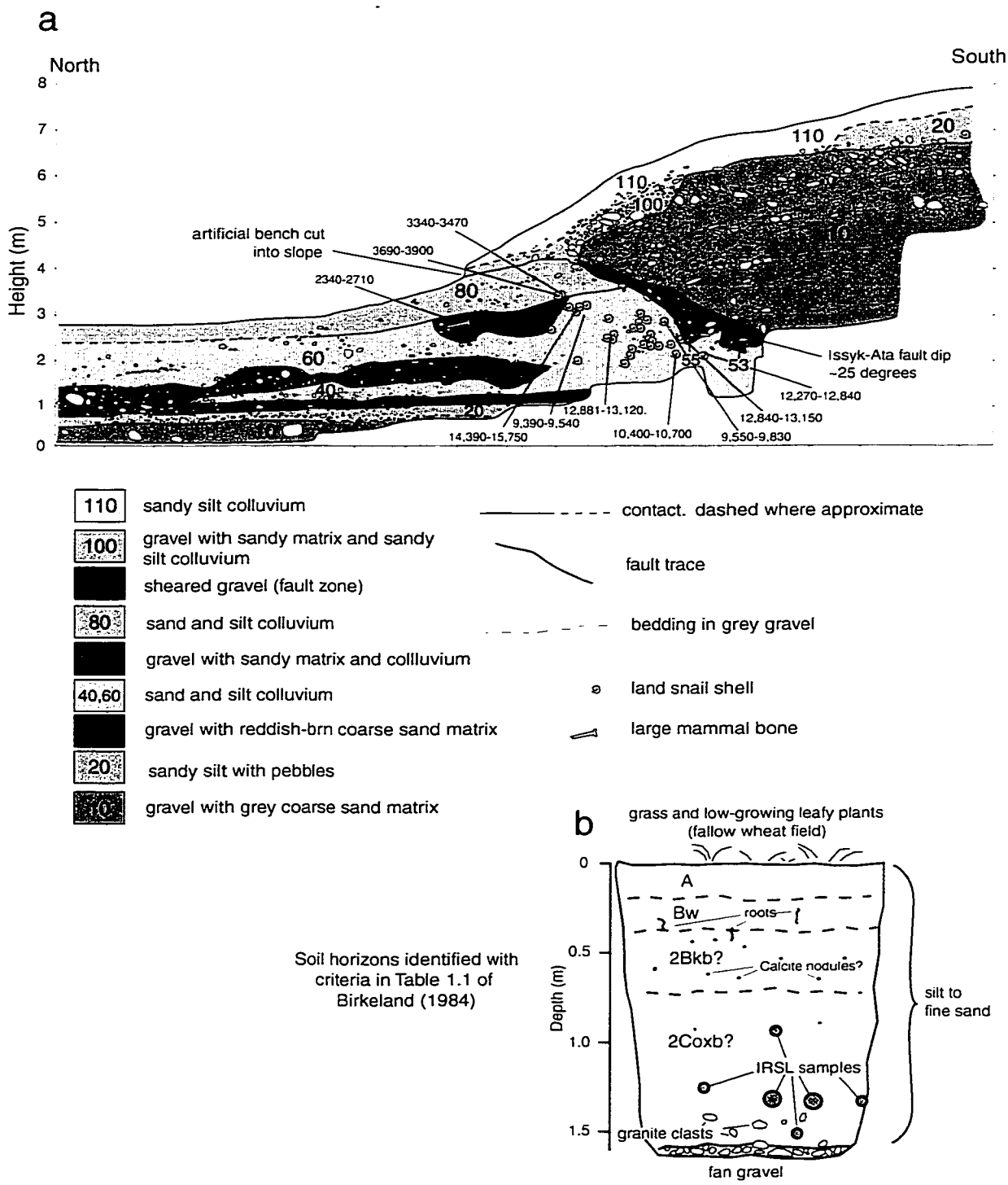

Figure 6.4: Trench and soil-pit logs at the Sokuluk River site. (a) Generalized map of the east wall, Sokuluk trench, showing the Issyk-Ata fault, key stratigraphic units, and calibrated radiocarbon ages. Scale is shown in meters, with no vertical exaggeration. Calibrated age ranges represent the 95% confidence interval, in cal yr B.P. (b) Log of pit on the QIII(2) fan, 20 m southwest of the trench (Figure 6.2). Soil profile interpretation and the location of the IRSL samples shown.

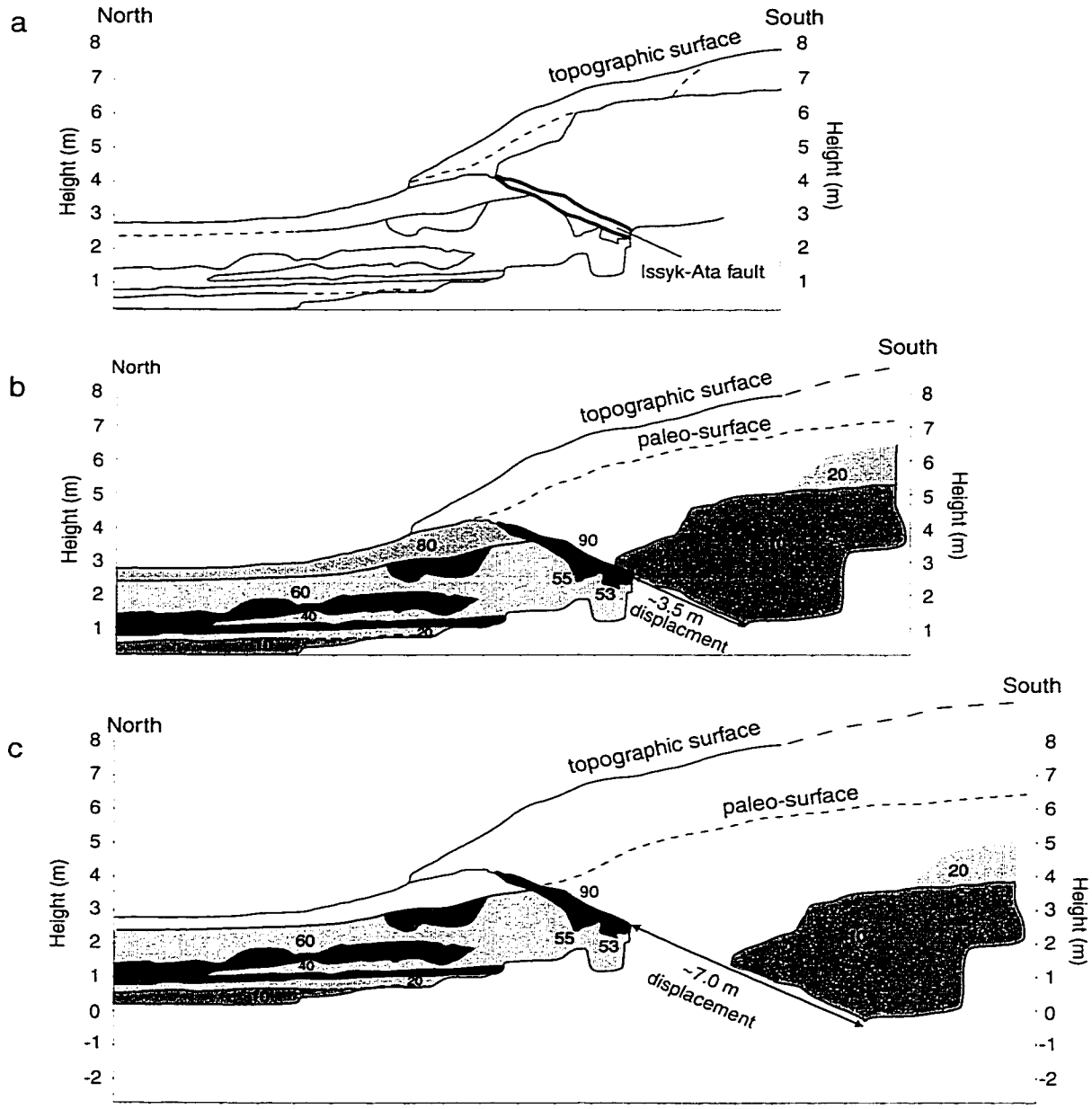

Figure 6.5: Restorations of the Sokuluk trench. (a) Trench wall outline, stratigraphic contacts, and the Issyk-Ata fault. (b) Restoration of slip and inferred location of the paleo-surface prior to the 1885 earthquake. The restoration is based on the 1.5 m-high scarp shown in Figure 6.3 and the 25° fault dip. (c) Restoration of the penultimate event and inferred location of the paleo-surface. The restoration is based on the 3.0 m-high scarp shown in Figure 6.3 and the fault dip. Horizontal scale is in meters, with no vertical exaggeration. Stratigraphic units are the same as in Figure 6.4.

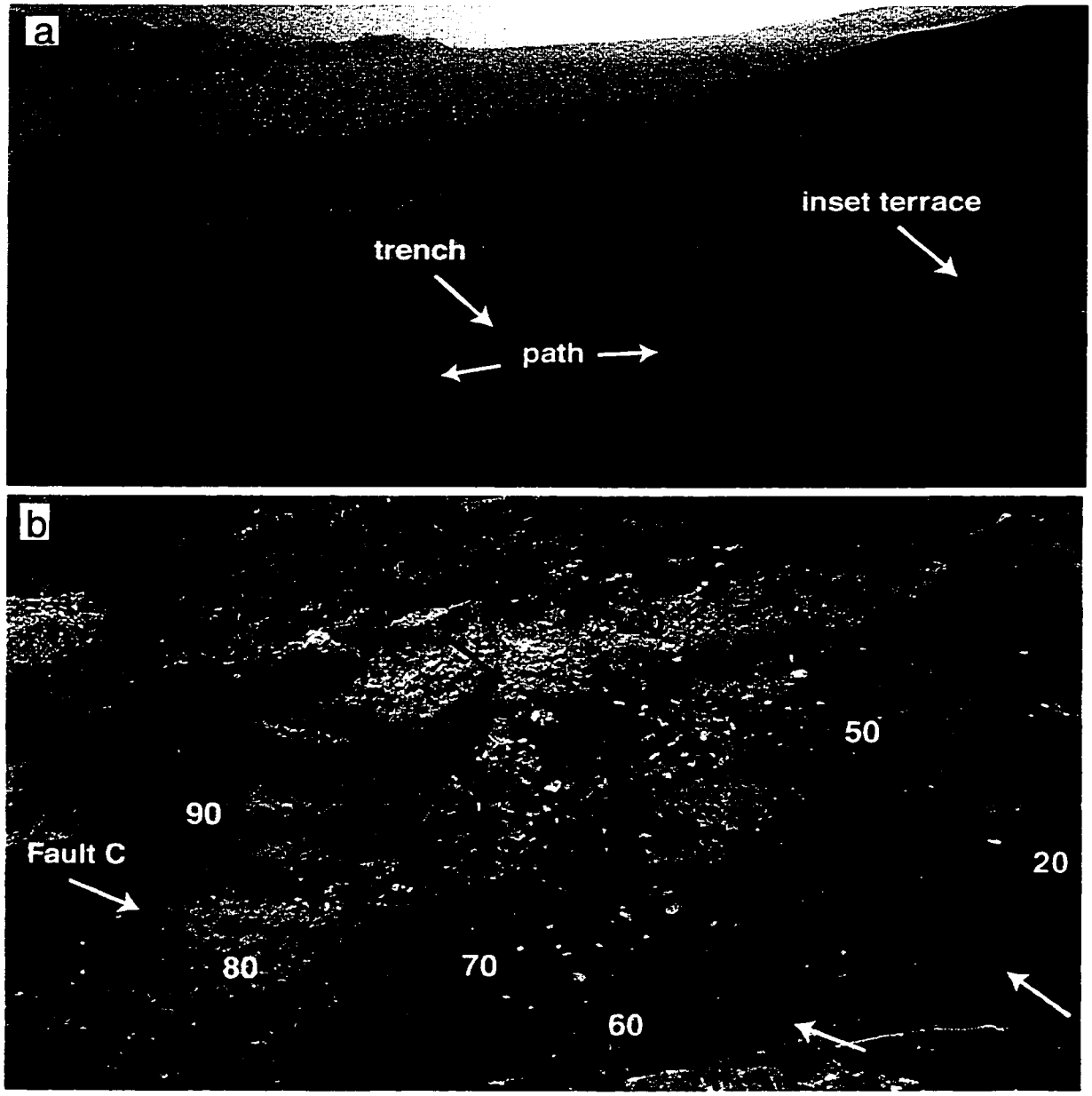

Figure 6.6: Photos of the Oinak-Djar fault trench. (a) View to the west along the Oinak-Djar fault scarp. Inset terrace in the hanging wall above the trench and the path adjacent to the trench are labeled. The spoil pile is about 2m high. The mounds on the fan surface in the middle left and the mound on the terrace in the upper right of the photo are cultural sites of unknown purpose. (b) Photo of the upper-north part of the west wall of the trench, showing part of the fault zone. Faults C and D, and selected units are labeled (see Figures 6.7 and 6.8). Colluvial units are reddish brown in the photo; coarse sand and gravel alluvium units are grey. Small pink flags on the trench wall mark fault traces.

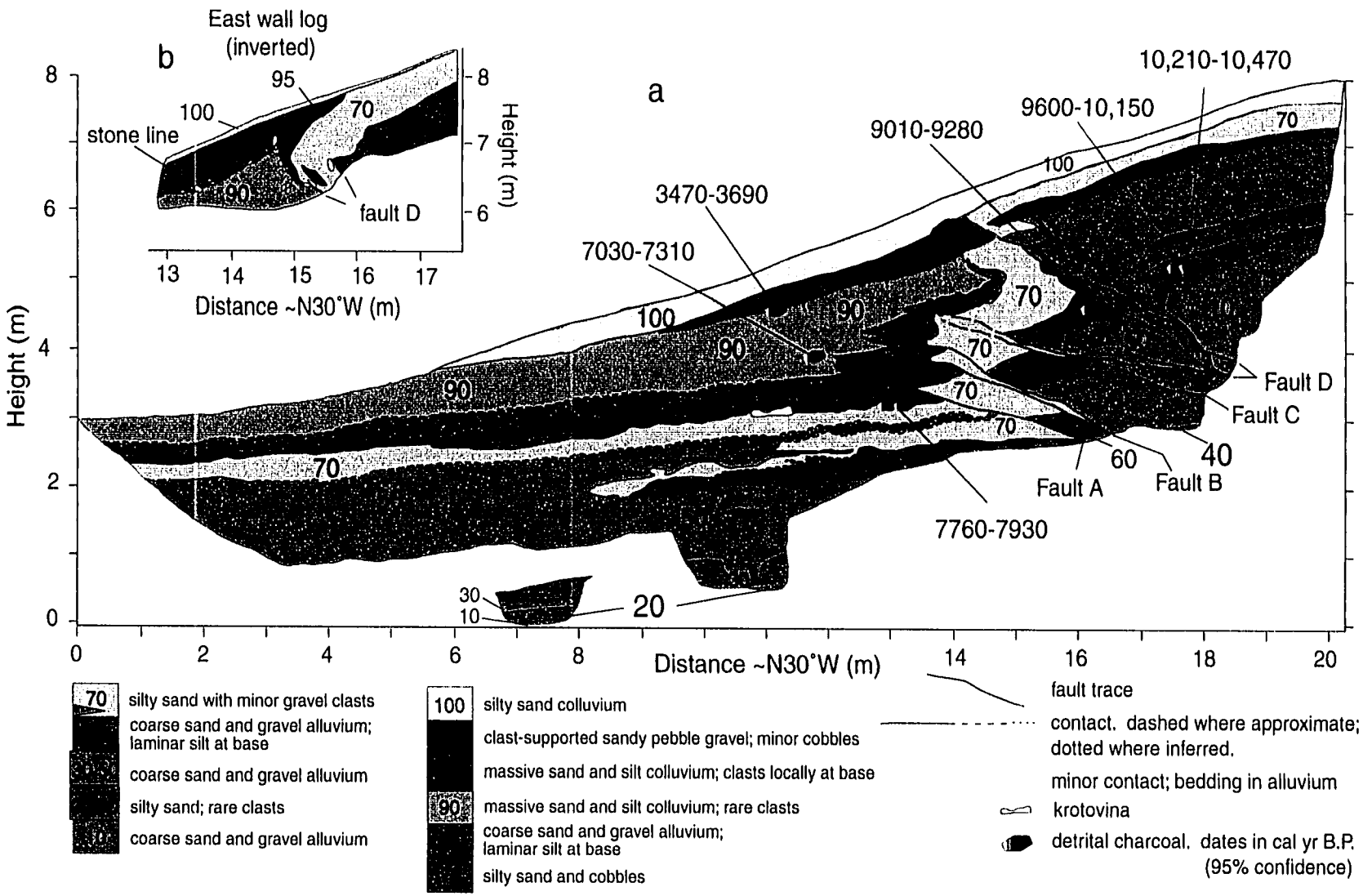

Figure 6.7: Log of the Oinak-Djar fault trench. (a) Map of the west wall showing stratigraphic units offset by faults A-D (faults B-D contain multiple strands). Pit at meter 7-8 was excavated beneath the east wall and is projected to the west wall. (b) Log of east wall across fault D within the upper units, showing injection feature (unit 95) and stone line in unit 90. The log is reflected so that it matches the orientation of (a).

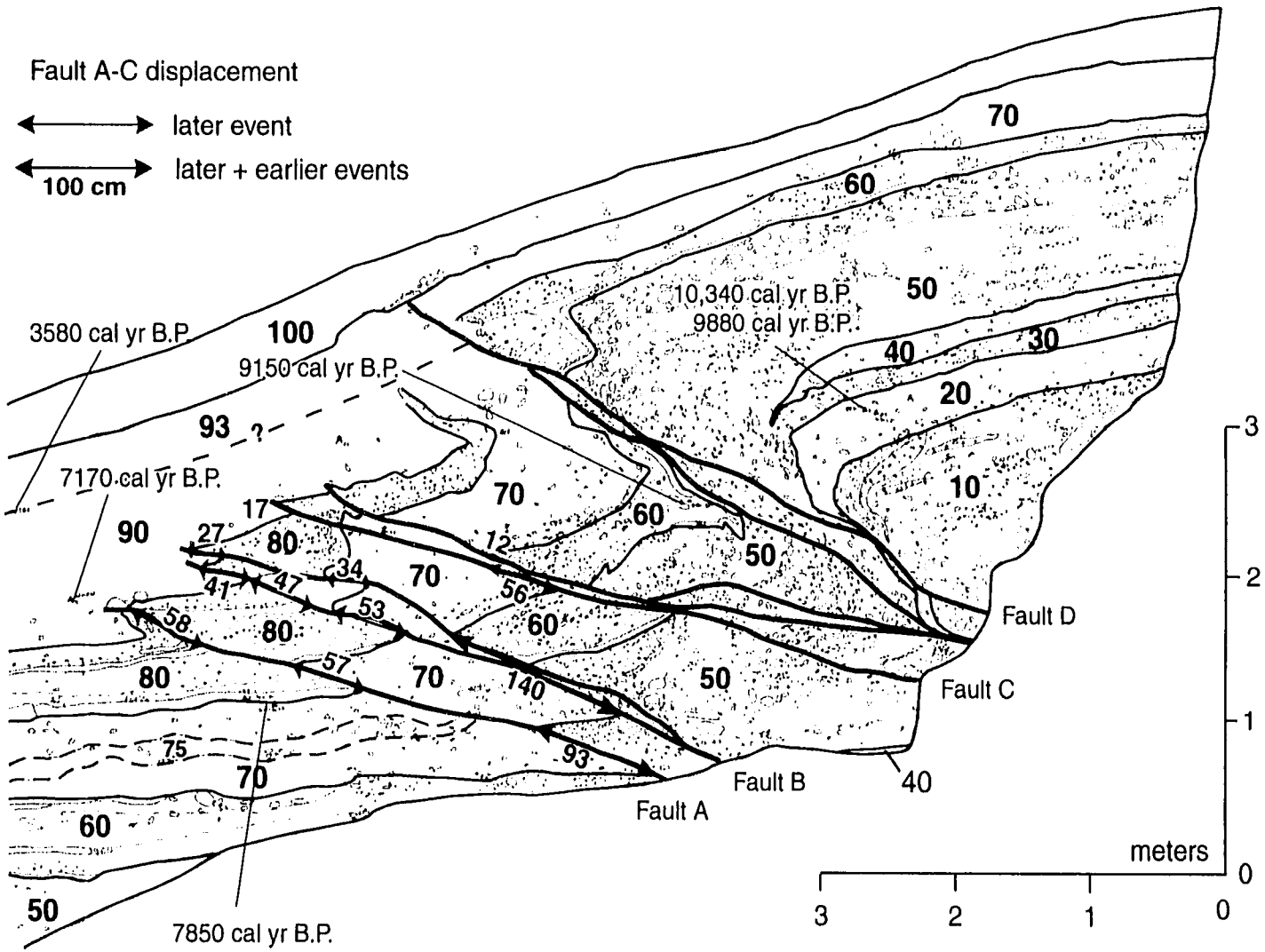

Figure 6.8: Detailed log of the west trench wall, showing fault zone and displacements of unit contacts across faults A-C. The calibrated radiocarbon ages shown are the midpoints of the 95% confidence limits.

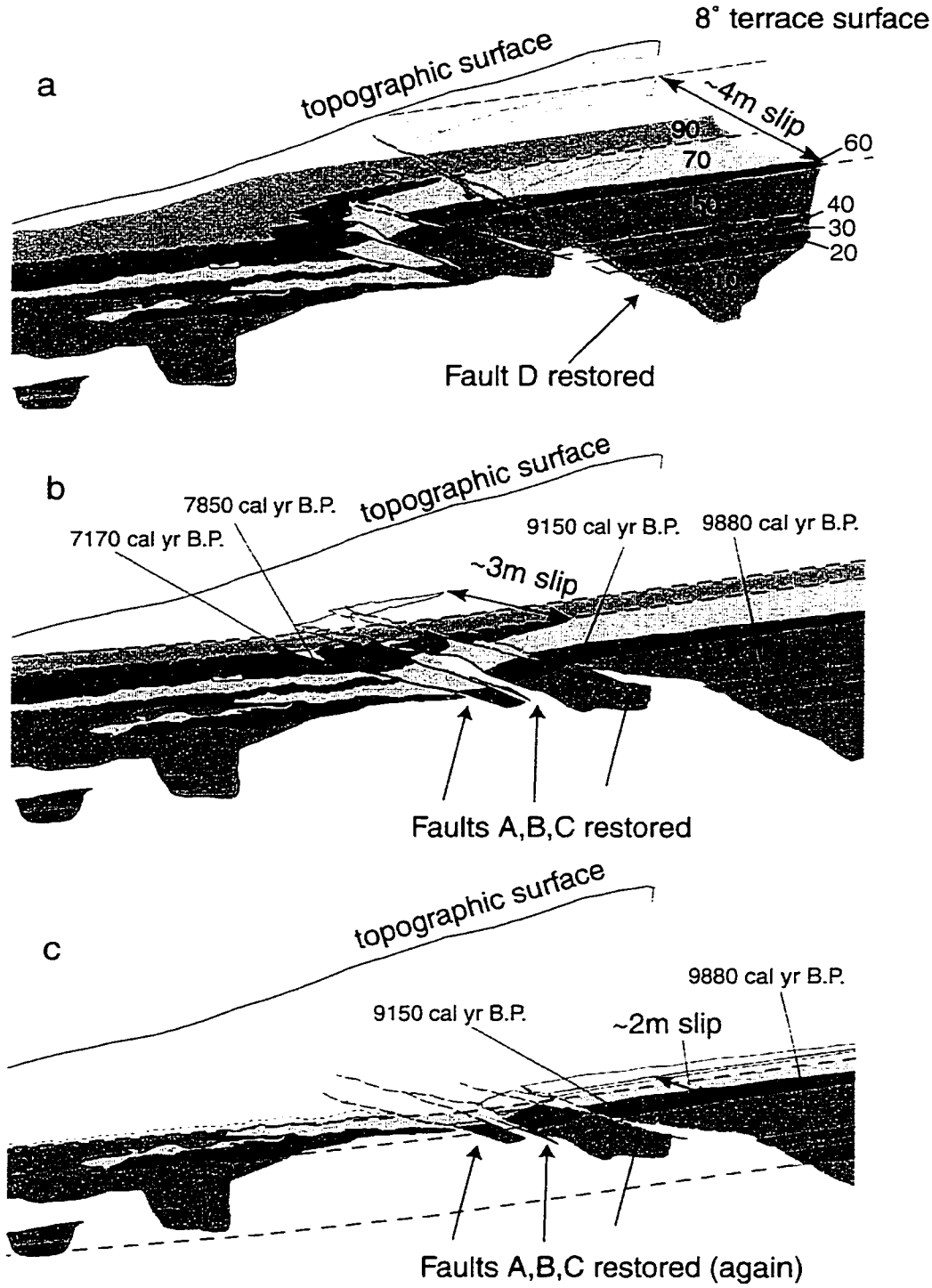

Figure 6.9: Restoration of slip for the Oinak-Djar fault trench. a) Restoration of slip on fault D. Restoration involves translation and rotation of hanging wall units so they have a gradient similar to the adjacent terrace tread. The amount of displacement is indicated by the black arrow. b) Second restoration involves translation of blocks along faults A, B, and C so that the top of unit 80 has a a gradient similar to the presumed original depositional slope (shown by the black dashed lines). Note the thickening of units 70 and 80 smoothing out the inferred paleo scarp. c) Third restoration involves translation of blocks along faults A, B, and C so that the laminar silt at the base of unit 60 has an smooth profile.

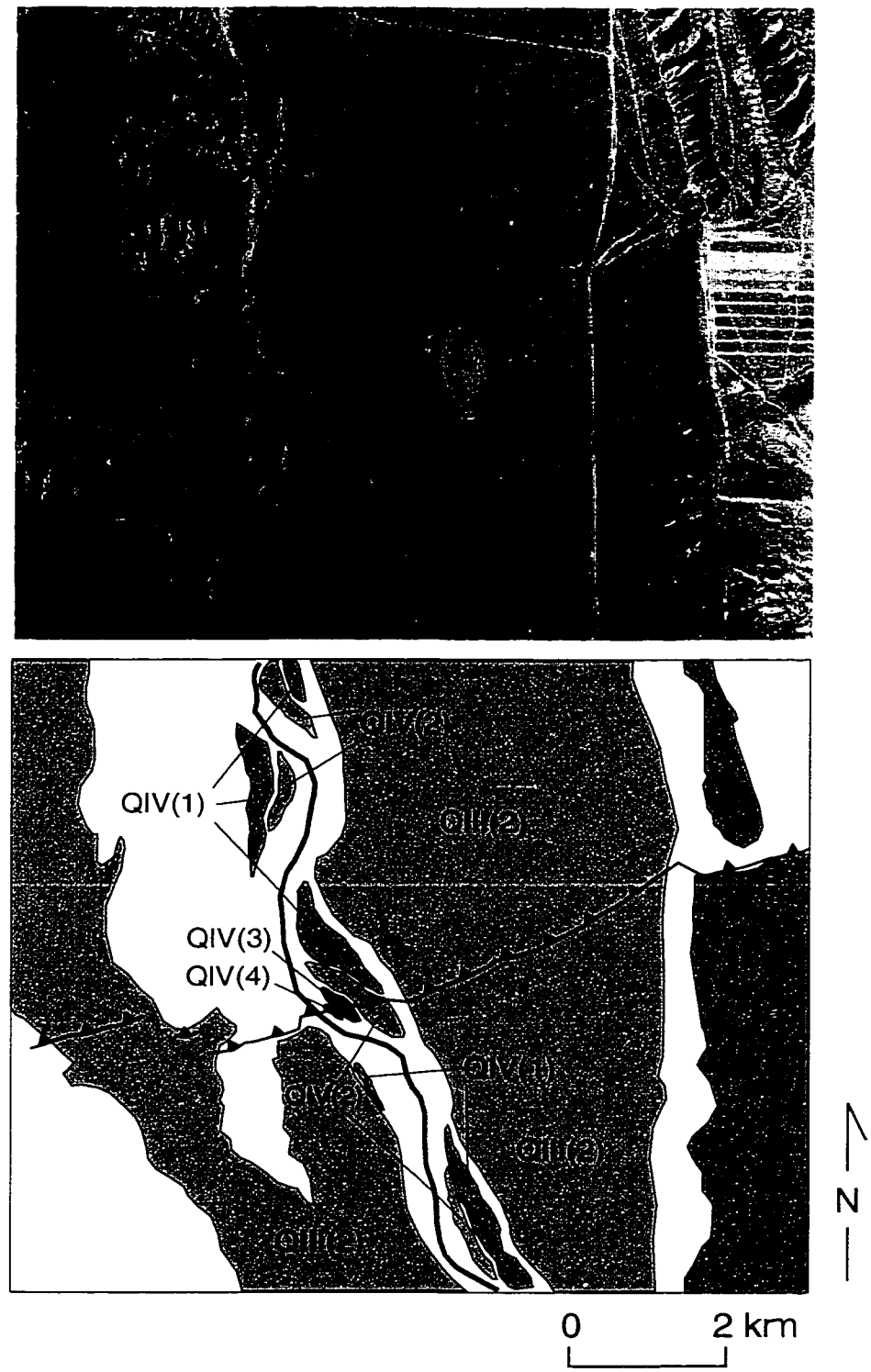

Figure 6.10: Kadjerty River terraces near the Kadjerty fault. Airphoto (above) and interpretation (below). White is Neogene, and Figure 4.9(c) shows strikes and dips of strata along the Kadjerty River.

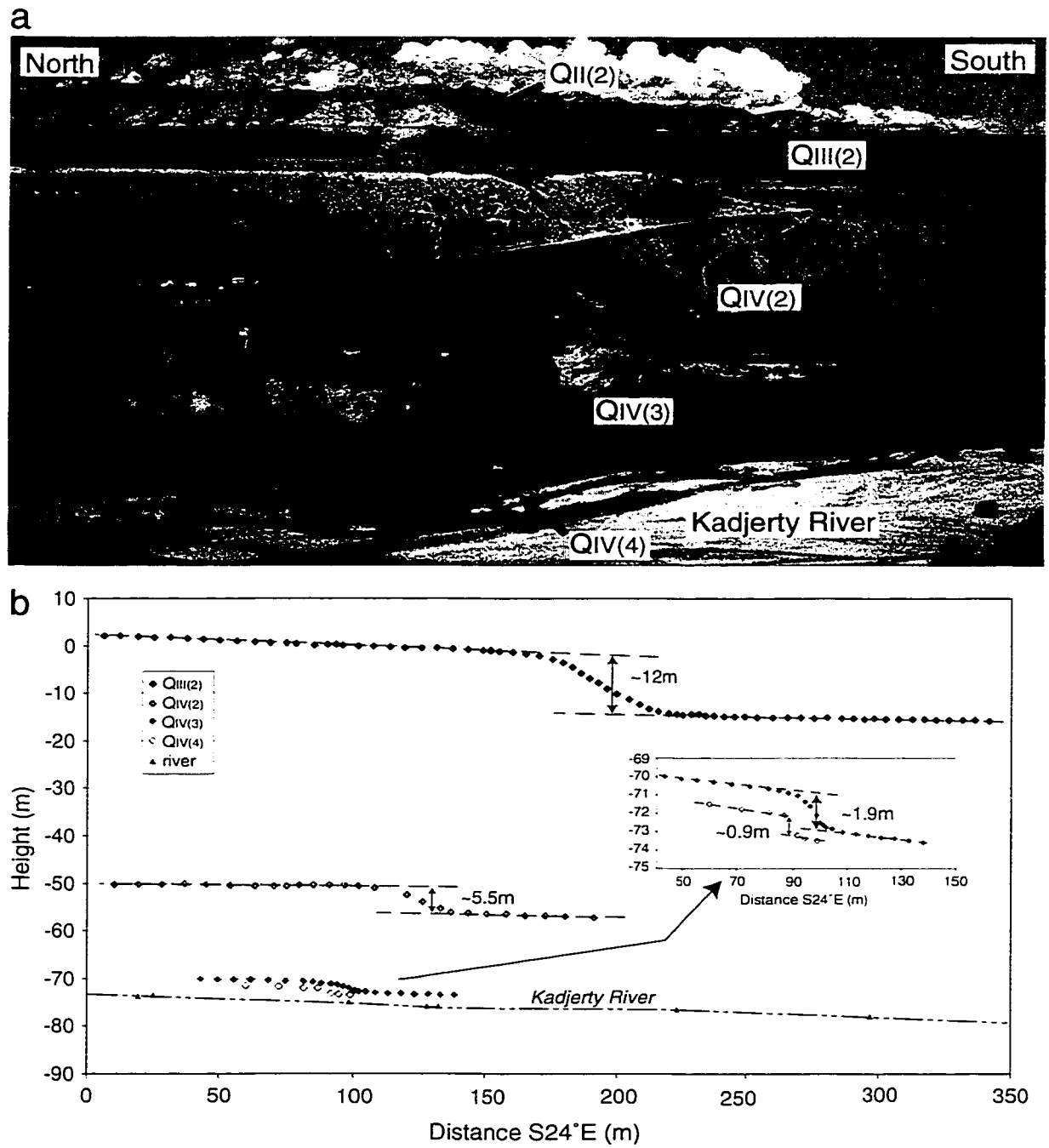

Figure 6.11: Nested terraces progressively offset by the Kadjerty fault, Kadjerty River. (a) View east across the Kadjerty River at the offset QII(2), QIII(2), QIV(2), QIV(3), and QIV(4) terraces. Arrows point to the inferred fault scarps. The QII(2) fault scarp has a vertical separation of 65-90 m. (b) Profiles of the offset QIII(2) and younger terraces, projected on a vertical plane normal to fault strike. The scarp across the youngest inset terrace, labeled QIV(4), may have been formed or modified by fluvial processes.

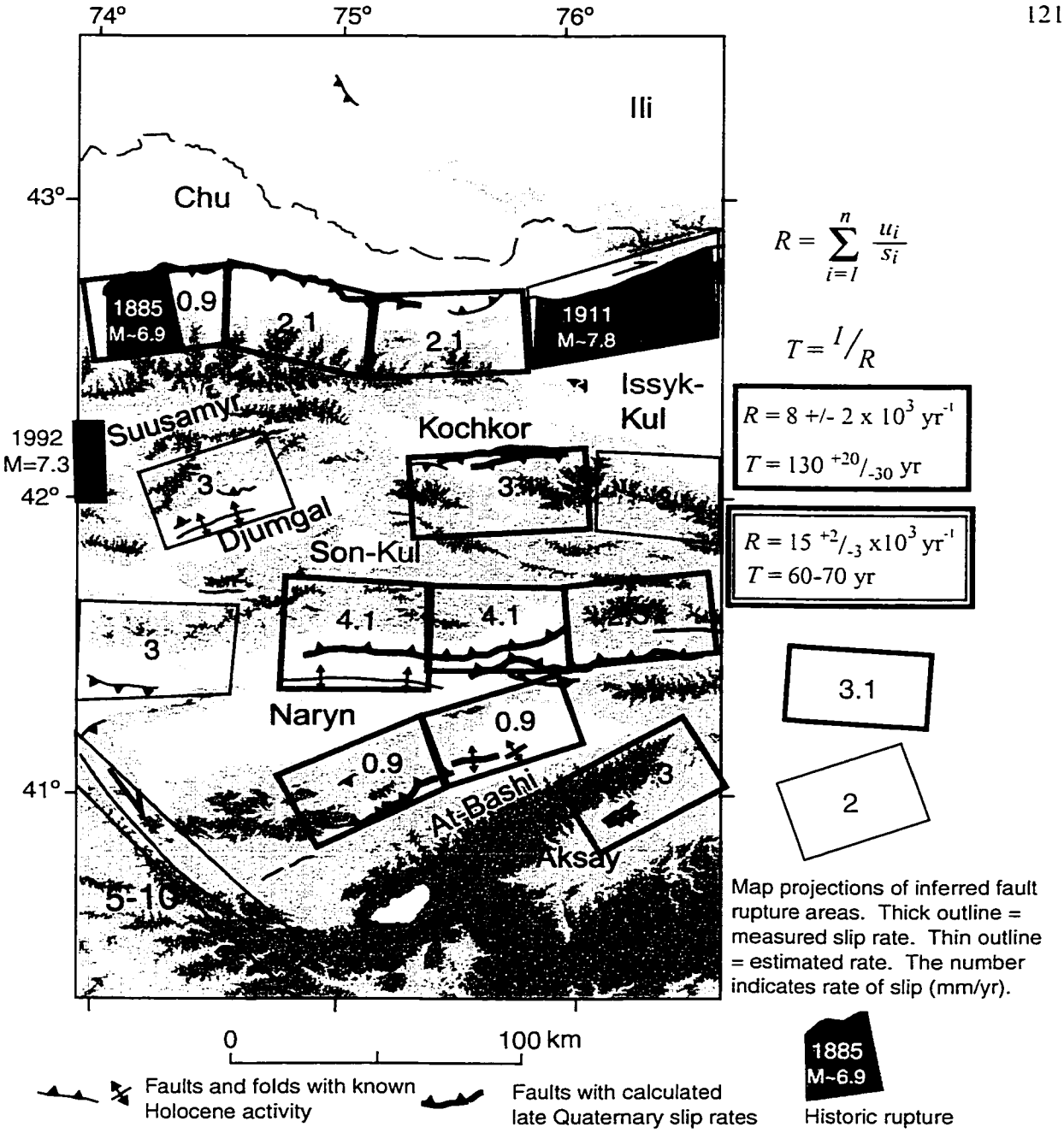

Figure 6.12: Preliminary source map for Holocene faults in the study area. The boxes indicate map projections of fault areas that would hypothetically rupture during large earthquakes (see text for further explanation). Boxes with thick outlines mark rupture sources of faults examined in this study. The numbers inside the boxes show values of slip rate, u; whole numbers in boxes with thin outlines indicate estimated slip rates on faults we have not studied in this project. The 5-10 mm/yr rate on a section of the Talas-Ferghana fault is based on geologic estimates of Trifonov et al. (1992) and Burtman et al. (1996). Earthquakes on each fault section are assumed to produce a displacement, d, of 2-4 m. The sum of the ratios u/d for each rupture source provides an estimate of recurrence rate, R, of large earthquakes in the region. The inferred rupture areas and magnitudes of the 1885, 1911, and 1992 earthquakes that lie within this map are indicted by grey rectangles. The analysis predicts a recurrence interval, T = 100-150 yr for faults measured in this study (thick lines) and T = 60-70 yr for all of the sources shown on the map.

Chapter 7

Discussion and Conclusions

This thesis provides a quantitative description of deformation across a contractional intracontinental mountain belt—the Tien Shan. Such mountain belts are common features on Earth (Rodgers, 1987), and an understanding of the forces and processes that cause intracontinental deformation is fundamental to plate tectonic theory (Molnar, 1988). A kinematic description of mountain building across the central Tien Shan places constraints on the properties of, and the processes operating on, the deforming lithosphere. This chapter summarizes my results that pertain to the geometry and kinematics of late Quaternary deformation in the upper crust across the northern 2/3 of the central Tien Shan. I will also present a brief discussion of end-member forces that may drive continental deformation here, and how my results place limits (however few) on deeper processes of deformation.

7.1 Kinematics

7.1.1 Style, distribution, and geometry of active faulting

Active north- and south-dipping thrust and reverse faults underlie virtually every intermontane basin across the central Tien Shan (Figure 1.3). Although strike-slip components are apparent on some of the east-west- to east-northeast-trending faults, the components likely accommodate north-south shortening: the active faulting does not suggest a major transpressive component (cf. Cobbold et al., 1994). The slip rates estimated on individual faults demonstrate that deformation is distributed across several faults that span the mountain belt, and that the faults underlying the basins have higher slip rates than faults that mark adjacent range-basin boundaries (Figure 4.18).

Faulting and fault-related folding of river terraces within the late Cenozoic intermontane basins indicate that faults dip ~20–40° at the surface, and dip ~5–15° towards the basin margins

at shallow crustal depths, within Tertiary basin strata (Figures 4.7 and 5.1). The patterns of folded terraces and underlying strata suggest that fault-related folding within the basins occurs by kink-band migration, as predicted by fault-bend fold theory (Suppe, 1983) (Figures 3.3–3.5 and 4.7). The high slip-rate faults within the basins are probably splays that intersect with moderately-dipping (30–50°), crustal-scale thrust ramps that underlie the mountain ranges. Although most papers by Russian and Kyrgyz authors suggest that steeply dipping faults penetrate the upper crust (e.g., Chediya, 1986; Sadybakasov, 1990), subsurface data across several range fronts of the Laramide orogeny—perhaps an analogous thick-skinned mountain belt—show shallow to moderate fault dips within the crystalline basement (Gries, 1983; Stone, 1993).

The inferred migration of active faulting from moderately dipping faults at the range fronts to shallow flat-and-ramp faulting in the basins appears prevalent in the Tien Shan (Avouac et al., 1993; Burchfiel et al., 1999), and likely occurred, at least locally, during the 1992 Suusamyr earthquake (Ghose et al., 1997). Although this style of deformation has been documented in other areas of thick-skinned deformation (Ikeda, 1983), it does not appear prevalent in the Sierras Pampeanas, where most Holocene faults lie at the range fronts (Costa and Vita-Finzi, 1996), and underthrusting of syntectonic sediment does not appear widespread during the Laramide orogeny (Gries, 1983; Erslev, 1986; Stone, 1993).

The fault geometry underlying the range-basin margins has several implications. First, the geometry predicts that slip on a ramp beneath the mountain ranges can contribute to further crustal thickening there, while most of the active shortening seen at the surface is expressed by a narrow row of hills within the basin interior. Second, knowledge of the fault geometry is required to convert fault slip rates to crustal shortening rates (Figure 5.2). If geodetic shortening measures interseismic strain accumulation across the locked portion of a fault, adequate prediction of interseismic strain must consider the location of the locked zone of the fault in the upper crust as well as the location of the fault at the surface. Third, separate faults at the surface within an intermontane basin may share a deeper crustal ramp, and therefore have a common seismic source. Areas of high shaking intensity may be offset from zones of surface rupture

hazard. Future work on subsurface fault geometry would greatly improve estimates of late Quaternary shortening rate, and total late Cenozoic shortening across range-basin margins.

7.1.2 Strain partitioning in the upper crust

Estimated rates of late Quaternary north-south shortening across major thrust and reverse fault zones are consistent with the pattern and rates of geodetic shortening, and indicate that deformation is distributed across a relatively few faults in the upper crust (Figure 5.3). The upper crust of the Kyrgyz central Tien Shan can be described as a series of ~30–70 km wide, fault-bounded blocks, with little internal deformation. Late Cenozoic faults and folds within the range blocks likely accommodate the movement of hanging-wall material across deeper fault bends, similar to the pattern inferred for the Laramide Rocky Mountain foreland (Narr and Suppe, 1994).

The slip rates and geodetic shortening rates indicate lower rates of near-surface deformation in the southern region, which has the highest topography and thickest crust (Figures 4.18 and 5.3) (S. Roecker, written communication, 2001). One possible explanation for this is that the crust continues to thicken beneath the high region in the south, by either ductile flow or faulting at depth. If the lack of horizontal shortening also indicates a similar slowing of crustal thickening, the southern region may be forming a nascent plateau. To further thicken already-thick crust requires more work than to thicken areas of lower mean topography, thinner crust, and lesser gravitational potential energy (e.g., Molnar and Lyon-Caen, 1988). Alternatively, a layered crustal rheology with a low viscosity lower layer may also limit crustal thickening (Royden, 1996).

The wide (~30–70 km wavelength) basin-and-range topography through our transect stands in contrast to the more narrow (~15–30 km wavelength) and higher elevation valleys to the east (Figures 1.2 and 1.3). It is unclear how well the pattern of distributed shortening across our transect (~75–76° longitude) describes deformation along a transect through Issyk-Kul basin (~77° longitude). It is possible that deformation there is more localized across the Issyk-Kul

basin and the northern and southern margins, if higher mean elevations coincide with lesser rates of shortening. The narrower ranges may indicate a closing of formerly broad basins by greater amounts of shortening, or this part of the belt may consist of more narrowly spaced fault-bounded blocks.

The pattern of distributed shortening across the Kyrgyz central Tien Shan stands in contrast to the shortening documented across the central portion of southern Tibet and the Himalaya. There, GPS measurements of interseismic strain accumulation are consistent with ~20 mm/yr slip rate on the gently dipping Main Himalaya thrust (Bilham et al., 1997). A Holocene slip rate of ~21 mm/yr is estimated for the Main Frontal thrust—the southernmost splay of the Main Himalaya thrust—indicating that almost all of the strain accumulating beneath the Himalaya is released at the southern deformation front (Lavé and Avouac, 2000). Shortening across the rest of the Tibetan plateau, however, appears distributed (Bendick et al., 2000). It is possible that the central Tien Shan is analogous to the central Himalaya and Tibetan Plateau, although on a smaller scale. While deformation across the northern 2/3 of the Tien Shan is distributed, shortening across the southern margin of the Tien Shan may be localized on one or two high slip-rate faults that define the southern deformational front (Rubin et al., 2000; Scharer et al., 2000; Dang et al., 2001). Possible underthrusting of the rigid Tarim block (Mattauer, 1986) may act in a similar manner as underthrusting of the India subcontinent.

7.1.3 Coseismic deformation

Paleoseismic evidence from three faults across the central Tien Shan show evidence for 2-4 m displacements at the surface. The paleoseismic data include evidence for 3.5 m of displacement during the 1885 $M \approx 6.9$ Byelovoda earthquake and appear similar to displacement during the 1992 $M_s = 7.3$ Suusamyr earthquake. Earthquakes of $M \approx 6.9$–7.4 probably occurred on faults across the Kyrgyz central Tien Shan. Although the data do not prove "characteristic" behavior at any site, a simple analysis that assumes recurring 2–4 m events along 50–65 km-long rupture sources predicts a 60-70 year recurrence interval for earthquakes of this size across the study area.

7.2 Dynamics

The degree to which mountain belts deform by localized or distributed strain ought to be predicted by mechanical and dynamic descriptions of mountain building processes. For mountain belts at plate margins, and for most "thin-skinned" fold-thrust belts, a gently-dipping fault underlying the belt provides a clear boundary condition that is appropriate for the use of the basal-traction driven critical-wedge model (e.g., Davis et al., 1983). In basement-involved mountain belts distant from plate boundaries, however, appropriate boundary conditions for deformation are less clear. Horizontal forces applied from afar may push lithospheric blocks together, causing either pure shear thickening (England and McKenzie, 1982; Houseman and England, 1986) or lithospheric buckling (Martinod and Davy, 1992, 1994). Alternatively, local mantle processes may cause subduction of continental mantle lithosphere, which could apply a basal traction, or shear stress, to the overlying crust (Willett et al., 1993; Royden, 1996). The anticipated patterns of deformation from modeling studies depend largely on the prescribed strength profile of continental lithosphere (e.g., Molnar, 1988; Willett, 1999). I briefly discuss two forces that may act on the Tien Shan lithosphere to drive deformation—horizontal forces and basal traction forces—and state the predicted strain-rate field based on different model parameterizations.

7.2.2 Horizontal forces at the margins

Horizontal forces applied to the margins of the Tien Shan may be manifested in at least two ways: pure-shear thickening of the lithosphere, or folding. Most of the literature exploring pure-shear thickening of continental lithosphere uses the thin viscous sheet approximation (e.g., England and McKenzie, 1982; Houseman and England, 1986). Although the thin-sheet approximation—which applies to regions that are many times wider than the thickness of the sheet— is not well suited at the scale of the Tien Shan, other numerical simulations of pure-shear thickening of a layered continental lithosphere predict distributed deformation (L. Royden and S. Willett, personal communication, 2001).

Horizontal forces may also result in folding of the lithosphere (Martinod and Davy, 1992; Burov et al., 1993; Martinod and Davy, 1994). The regular spacing of major crustal blocks seen

in the Tien Shan (mentioned above, and explored by Burov et al., 1993) and in other thick-skinned belts (Jordan and Allmendinger, 1986; Erslev and Rogers, 1993) is perhaps explained by folding instabilities within a brittle upper crust. Folding of the lithosphere also predicts distributed crustal deformation (Martinod and Davy, 1994).

7.2.1 Basal traction

Local mantle processes beneath the Tien Shan may apply a shear stress to the base of the crust. Critical-wedge theory has advanced the understanding of mountain building processes for conditions in which deformation by simple shear characterizes a basal boundary condition (Chapple, 1978; Dahlen, 1984). The characteristic polarity of many belts in contractional settings, with a vergence and propagation of new faults in the direction of the underthrust plate [Bally, 1966 #258; Boyer, 1982 #260; Dahlstrom, 1970 #259, has been replicated in laboratory experiments employing basal traction boundary conditions (e.g., Liu et al., 1992). In analog (Koyi et al., 2000) and numerical (Willett, 1999) simulations of the critical wedge, basal boundary conditions with high friction or high viscosity décollement lead to both a localization of high strain rate at the leading edge of deformation and a dominant polarity to the belt. Deformation above décollement with lower values of friction or viscosity results in a similar unidirectional propagation of new structures, but shortening and strain rate are partitioned over a broader area (compare figures 10 and 13 in Willett, 1999). If a basal traction drives the central Tien Shan, the zone of lithospheric décollement, assumed to be in the lower crust, must be weak compared to the strength of the upper crust.

7.3 Concluding remarks

The central Tien Shan offers an exceptional opportunity to explore the active kinematics of intracontinental mountain building. The work presented in this thesis represents only a preliminary effort to characterize the styles and rates of late Quaternary faulting along a narrow transect that crosses the northern 2/3 of the belt. This research contributes a more quantitative measure of the distributed shortening that has been observed and documented by previous workers for over half a century (Schulz, 1948).

References

Abdrakhmatov, K. Ye., Thompson, S., Weldon, R., Delvaux, D., and Klerkx, J., 2001, Active faults of Tien-Shan (in Russian): Science and New Technology (Nauka i novye tehnologyi), v. 2, p. 22-28.

Abdrakhmatov, K. Ye., 1988, Quaternary tectonics of the Chu basin (in Russian): Frunze, Kyrgyzstan, Ilim, 120 p.

Abdrakhmatov, K. Ye., Aldazhanov, S. A., Hager, B. H., Hamburger, M. W., Herring, T. A., Kalabaev, K. B., Makarov, V. I., Molnar, P., Panasyuk, S. V., Prilepin, M. T., Reilinger, R. E., Sadybakasov, I. S., Souter, B. J., Trapeznikov, Y. A., Tsurkov, V. Y., and Zubovich, A. V., 1996, Relatively recent construction of the Tien Shan inferred from GPS measurements of present-day crustal deformation rates: Nature, v. 384, no. 6608, p. 450-453.

Aitken, M. J., 1985, Thermoluminescence dating: London, Academic Press, 359 p.

Aitken, M. J., 1998, Introduction to Optical Dating: Oxford, Oxford University Press, 256 p.

An, Z., Kukla, G. J., Porter, S. C., and Xiao, J., 1991, Magnetic susceptibility evidence of monsoon variation on the Loess Plateau of central China during the last 130,000 years: Quaternary Research, v. 36, p. 29-36.

Arrowsmith, J. R., and Strecker, M. R., 1999, Seismotectonic range-front segmentation and mountain-belt growth in the Pamir-Alai region, Kyrgyzstan (India-Eurasia collision zone): Geological Society of America Bulletin, v. 111, no. 11, p. 1665-1683.

Avouac, J. P., Tapponnier, P., Bai, M., You, H., and Wang, G., 1993, Active thrusting and folding along the northern Tien Shan and late Cenozoic rotation of the Tarim relative to Dzungaria and Kazakhstan: Journal of Geophysical Research, v. 98, p. 6755-6804.

Bally, A. W., Burbi, L., Cooper, C., and Ghelardoni, R., 1986, Balanced sections and seismic reflection profiles across the central Apennines: Mem. Soc. Geol. It., v. 35, p. 257-310.

Beanland, S., and Barrow-Hurlbert, S. A., 1988, The Nevis-Cardrona fault system, central Otago, New Zealad; late Quaternary tectonics and structural development: New Zealand Journal of Geology and Geophysics, v. 31, p. 337-352.

Bendick, R., Bilham, R., Freymueller, J., Larson, K., and Yin, G., 2000, Geodetic evidence for a low slip rate in the Altyn Tagh fault system: Nature, v. 404, p. 69-72.

Benedetti, L., Tapponnier, P., King, G. C. P., Meyer, B., and Manighetti, I., 2000, Growth folding and active thrusting in the Montello region, Veneto, northern Italy: Journal of Geophysical Research, v. 105, p. 739-766.

Berger, G. W., 1988, Dating Quaternary events by luminescence, *in* Easterbrook, D. J., ed., Dating Quaternary Sediments: Special Paper 227: Boulder, Geological Society of America, p. 13-50.

Berger, G. W., 1990, Effectiveness of natural zeroing of the thermoluminescence in sediments: Journal of Geophysical Research, v. 95, p. 12,375-12,397.

Berger, G. W., Lockhart, R. A., and Kuo, J., 1987, Regression and error analysis applied to the dose-response curves in thermoluminescence dating: Nuclear Tracks and Radiation Measurements, v. 13, p. 177-184.

Biasi, G. P., and Weldon, R. J., 1994, Quantitative refinement of calibrated 14C distributions: Quaternary Research, v. 41, p. 1-18.

Bilham, R., Larson, K. M., Freymueller, J. T., Jouanne, F., Le, F. P., Leturmy, P., Mugnier, J. L., Gamond, J. F., Glot, J. P., Martinod, J., Chaudury, N. L., Chitrakar, G. R., Gautam, U. P., Koirala, B. P., Pandey, M. R., Ranabhat, R., Sapkota, S. N., Shrestha, P. L., Thakuri, M. C., Timilsina, U. R., Tiwari, D. R., Vidal, G., Vigny, C., Galy, A., and de, V. B., 1997, GPS measurements of present-day convergence across the Nepal Himalaya: Nature, v. 386, p. 61-64.

Birkeland, P. W., 1984, Soils and Geomorphology: New York, Oxford University Press, 372 p.

Bogdanovitch, K. I., Kark, I. M., Korolkov, B. Y., and Mushketov, D. I., 1914, The Earthquake in the Northern Districts of the Tien Shan, 22 December 1910 (4 January 1911) (in Russian): St. Petersburg, Commission of the Geology Committee.

Bonilla, M. G., and Lienkaemper, J. J., 1990, Visibility of fault strands in exploratory trenches and timing of rupture events: Geology, v. 18, no. 2, p. 153-156.

Boyer, S. E., 1992, Geometric evidence for synchronous thrusting in the southern Alberta and northwest Montana thrust belts, *in* McClay, K. R., ed., Thrust Tectonics: London, Chapman & Hall, p. 377-390.

Boyer, S. E., and Elliott, D., 1982, Thrust Systems: American Association of Petroleum Geologists, v. 66, p. 1196-1230.

Broecker, W. S., Oppo, D., Peng, T. H., Curry, W., Andree, M., Wolfli, W., and Bonani, G., 1988, Radiocarbon-based chronology for the 18O/16O record for the last deglaciation: Paleoceanography, v. 3, p. 509-515.

Brown, E. T., Bourles, D. L., Burchfiel, B. C., Deng, Q., Li, J., Molnar, P., Raisbeck, G. M., and Yiou, F., 1998, Estimation of slip rates in the southern Tien Shan using cosmic ray

exposure dates of abandoned alluvial fans: Geological Society of America Bulletin, v. 110, no. 3, p. 377-386.

Brown, T. A., Nelson, D. E., Vogel, J. S., and Southon, J. R., 1988, Improved collagen extraction by modified Longin method: Radiocarbon, v. 30, no. 2, p. 171-177.

Bull, W. B., 1991, Geomorphic Response to Climate Change: New York, Oxford University Press, 326 p.

Bullen, M., Burbank, D., Garver, J., and Abdrakhmatov, K. Y., in press, Late Cenozoic tectonic evolution of the northwestern Tien Shan: new age estimates for the initiation of mountain building: Geological Society of America Bulletin.

Burbank, D. W., McLean, J. K., Bullen, M., Abdrakhmatov, K. Y., and Miller, M. M., 1999, Partitioning of intermontane basins by thrust-related folding, Tien Shan, Kyrgyzstan: Basin Research, v. 11, p. 75-92.

Burchfiel, B. C., Brown, E. T., Qidong, D., Xianyue, F., Jun, L., Molnar, P., Jianbang, S., Zhangming, W., and Huichuan, Y., 1999, Crustal shortening on the margins of the Tien Shan, Xinjiang, China: International Geology Review, v. 41, p. 665-700.

Burov, E. B., Lobkovsky, L. I., Cloetingh, S., and Nikishin, A. M., 1993, Continental lithosphere folding in Central Asia (Part II): constraints from gravity and topography: Tectonophysics, v. 226, p. 73-87.

Burtman, V. S., 1964, The Talaso-Ferghana strike-slip rault (in Russian), Trudy Geol. Inst., Akad. Nauk, USSR: Moscow, Nauka, 143 p.

Burtman, V. S., 1975, Structural geology of Variscan Tien Shan, USSR: American Journal of Science, v. 275-a, p. 157-186.

Burtman, V. S., Skobelev, S. F., and Molnar, P., 1996, Late Cenozoic slip on the Talas-Ferghana Fault, the Tien Shan, Central Asia: Geological Society of America Bulletin, v. 108, no. 8, p. 1004-1021.

Butler, R. W. H., 1986, Thrust tectonics, deep structure and crustal subduction in the Alps and Himalayas: Journal of the Geological Society of London, v. 143, no. 6, p. 857-873.

Carver, G. A., and McCalpin, J. P., 1996, Paleoseismology of compressional tectonic environments, *in* McCalpin, J. P., ed., Paleoseismology: New York-London-Toronto, Academic Press, p. 183-270.

Chapple, W. M., 1978, Mechanics of thin-skinned fold-and-thrust belts: Geological Society of America Bulletin, v. 89, no. 8, p. 1189-1198.

Chediya, O. K., 1986, Morphology and neotectonics of the Tien Shan (in Russian): Frunze (Bishkek), Ilim, 313 p.

Chediya, O. K., Udalov, N. F., Grigina, O. M., Utkina, N. G., Fortuna, A. B., and Yazovskiy, V. M., 1976, Geology of Cenozoic of Chu basin and surrounding mountains (in Russian): Leningrad, Nauka.

Cobbold, P. R., Sadybakasov, E., and Thomas, J. C., 1994, Cenozoic transpression and basin development, Kyrghyz Tien Shan, Central Asia, *in* F. Roure, N. E., V.S. Shein, I. Skvortsov, ed., Geodynamic Evolution of Sedimentary Basins, International Symposium: Paris, Technip, p. 181-202.

Cook, F. A., Albaugh, D. S., Brown, L. D., Kaufman, S., Oliver, J. E., and Hatcher, R. D. J., 1979, Thin-skinned tectonics in the crystalline southern Appalachians; COCORP seismic-reflection profiling of the Blue Ridge and Piedmont: Geology, v. 7, no. 12, p. 563-567.

Costa, C. H., and Vita-Finzi, C., 1996, Late Holocene faulting in the Southeast Sierras Pampeanas of Argentina: Geology, v. 24, no. 12, p. 1127-1130.

Crowley, T. J., and North, G. R., 1991, Paleoclimatology: New York, Oxford University Press, 339 p.

Dahlen, F. A., 1984, Noncohesive critical Coulomb wedges: An exact solution: Journal of Geophysical Research, v. 89, p. 10125-10133.

Dahlstrom, C. D. A., 1970, Structural geology in the eastern margin of the Canadian Rocky Mountains: Bulletin of Canadian Petroleum Geology, v. 18, p. 332-406.

Dang, Y., Herring, T. A., Hager, B. H., Chen, J., Zhang, Y., and Jiang, Z., 2001, Global Positioning System measurements of contemporary crustal motion in southern Tien Shan, China: Eos Trans. AGU, Spring Meet. Suppl., v. 82, no. 20, p. S422.

Davis, D., Suppe, J., and Dahlen, F. A., 1983, Mechanics of fold-and-thrust belts and accretionary wedges: Journal of Geophysical Research, v. 88, p. 1153-1172.

DeMets, C., Gordon, R. G., Argus, D. F., and Stein, S., 1994, Effect of recent revisions to the geomagnetic reversal time scale on estimates of current plate motions: Geophysical Research Letters, v. 21, no. 20, p. 2191-2194.

England, P. C., and McKenzie, D. P., 1982, A thin viscous sheet model for continental deformation: Geophysical Journal of the Royal Astronomical Society, v. 70, p. 295-321.

Erslev, E. A., 1986, Basement balancing of Rocky Mountain foreland uplifts: Geology, v. 14, no. 3, p. 259-262.

Erslev, E. A., and Rogers, J. L., 1993, Basement-cover geometry of Laramide fault-propagation folds, *in* Schmidt, C. J., Chase, R. B., and Erslev, E. A., eds., Laramide basement

deformation in the Rocky Mountain foreland of the Western United States: Special Paper 280: Boulder, Geological Society of America, p. 125-146.

Fairbanks, R. G., 1989, A 17,000 year glacio-eustatic sea level record: influence of glacial melting rates on the Younger Dryas event and deep-ocean circulation: Nature, v. 345, p. 637-642.

Fedorovich, B. A., 1935, Data of Geology and Geochemistry of the Tien Shan (in Russian), Transactions of Kyrgyz Complex Expedition of 1932-1933., 243 p.

Ghose, S., Hamburger, M. W., and Ammon, C., 1998, Source parameters of moderate-size earthquakes in the Tien Shan, Central Asia from regional movement tensor inversion: Geophysical Research Letters, v. 25, no. 16, p. 3181-3184.

Ghose, S., Mellors, R. J., Korjenkov, A. M., Hamburger, M. W., Pavlis, T. L., Pavlis, G. L., Omuraliev, M., Mamyrov, E., and Muraliev, A. R., 1997, The M (sub s) = 7.3 1992 Suusamyr, Kyrgyzstan, earthquake in the Tien Shan; 2, Aftershock focal mechanisms and surface deformation: Bulletin of the Seismological Society of America, v. 87, no. 1, p. 23-38.

Gillespie, A. R., and Molnar, P., 1995, Asynchronous maximum advances of mountain and continental glaciers: Reviews of Geophysics, v. 33, no. 3, p. 311-364.

Goodfriend, G. A., 1987, Radiocarbon age anomalies in shell carbonate of land snails from semi-arid areas: Radiocarbon, v. 29, no. 2, p. 159-167.

Gould, M. M., Weberling, K., Weldon, R. J. I., Miller, M. M., Abdrakhmatov, K., and August, M. S., 2000, Neogene magnetostratigraphy in the At-Bashi basin: constraints on late Cenozoic deformation in the central Tien Shan, Kyrgyzstan: Geological Society of America Abstracts with Programs, v. 32.

Gries, R. R., 1983, Oil and gas prospecting beneath Precambrian of foreland thrust plates in Rocky Mountains: American Association of Petroleum Geologists Bulletin, v. 67, no. 1, p. 1-28.

Grigina, O. M., and Fortuna, A. B., 1981, Paleogeography of the Cenozoic of the Northern Tien Shan (in Russian): Frunze (Bishkek), Ilim, 150 p.

Grigorienko, P. G., 1961, About stratigraphy and history of formation of Quaternary deposits of northern Kyrgyzstan (in Russian), In: Reports of meeting about studying of Quaternary Period: Tashkent, SAIGAMC.

Grigorienko, P. G., 1970, The main features of geological development of Krygyz Tien Shan during the Quaternary Period (in Russian), Materials about Cenozoic Geology and the Newest tectonic of the Tien Shan: Frunze, Ilim.

Guiot, J., Pons, A., de Beaulieu, J. L., and Reille, M., 1989, A 140,000-year continental climate reconstruction from two European pollen records: Nature, v. 338, p. 309-313.

Hager, B. H., Burbank, D., Frey, F. A., Herring, T., McNutt, M. K., Miller, M. M., Molnar, P., Park, S., Pavlis, G., Roecker, S. W., Rubin, C. M., Weldon, R. J. I., and Vernon, F., 1996, Collaborative Research: Geodynamics of intracontinental mountain building in the Tien Shan, Central Asia: proposal submitted to the Continental Dynamics Program, NSF.

Hager, B. H., Lyzenga, G. A., Donnellan, A., and Danan, D., 1999, Reconciling rapid strain accumulation with deep seismogenic fault planes in the Ventura basin, California: Journal of Geophysical Research, v. 104, p. 25,207-25,219.

Hemphill-Haley, M. A., and Weldon, R. J. I., 1999, Estimating prehistoric earthquake magnitude from point measurements of surface rupture: Bulletin of the Seismological Society of America, v. 89, no. 5, p. 1264-1279.

Henderson, G. M., and Slowey, N. C., 2000, Evidence from U-Th dating against Northern Hemisphere forcing of the penultimate deglaciation: Nature, v. 404, p. 61-66.

Hendrix, M. S., Dumitru, T. A., and Graham, S. A., 1994, Late Oligocene-early Miocene unroofing in the Chinese Tian Shan; an early effect of the India-Asia collision: Geology, v. 22, no. 6, p. 487-490.

Holt, W. E., Chamot, R. N., Le-Pichon, X., Haines, A. J., Shen, T. B., and Ren, J., 2000, Velocity field in Asia inferred from Quaternary fault slip rates and Global Positioning System observations: Journal of Geophysical Research, v. 105, p. 19,185-19,209.

Houseman, G. A., and England, P. C., 1986, Finite strain calculations of continental deformation; 1. Method and general results for convergent zones: Journal of Geophysical Research, v. 91, p. 3651-3663.

Humphreys, E. D., and Weldon, R. J. I., 1994, Deformation across the western United States; a local estimate of Pacific-North America transform deformation: Journal of Geophysical Research, v. 99, p. 19975-20010.

Ignatiev, I. V., 1886, Earthquakes in Tokmak district in 1885 (in Russian): Isviestia, Russian Geographical Society, v. 22, no. 2.

Ikeda, Y., 1983, Thrust-front migration and its mechanism; evolution of intraplate thrust fault system: Bulletin of the Department of Geography, University of Tokyo, v. 15, p. 125-159.

Imbrie, J., Hays, J. D., Martinson, D. G., McIntyre, A., Mix, A. C., Morley, J. J., Pisias, N. G., Prell, W. L., and Shackleton, N. J., 1984, The orbital of Pleistocene climate: Support from a revised chronology of the marine 18-O record, *in* Berger, A. L. et al., ed., Milankovitch and Climate: Reidel, Dordrecht, p. 269-305.

Jordan, T. E., and Allmendinger, R. W., 1986, The Sierras Pampeanas of Argentina; a modern analogue of Rocky Mountain foreland deformation: American Journal of Science, v. 286, no. 10, p. 737-764.

Kadirov, S. A., 1968, Quaternary deposits of Alabuga-Naryn and Togus-Toro basins (in Russian) [Ph.D. thesis]: Academy of Science, Uzbek SSR, 22 p.

Kalmurzaev, K. Ye. (editor), 1979, The map of seismic zoning of Kyrgyzia (in Russian): Frunze, Ilim.

Knauf, V. I., 1976, Tectonic zoning of Northern Kyrgyzia (in Russian): Geotectonica, v. 5.

Kondorskaya, N. V., and Shebalin, N. V., 1977, New Catalog of Strong Earthquakes in the Territory of the USSR (in Russian): Moscow, Nauka, p. 535.

Koyi, H. A., Hessami, K., and Teixell, A., 2000, Epicenter distribution and magnitude of earthquakes in fold-thrust belts: insights from sandbox models: Geophysical Research Letters, v. 27, no. 2, p. 273-276.

Kuchai, V. K., 1969, Results of repeated examination of the remaining deformation in the pleistoseist of the Kebin earthquake (in Russian): Geologia y Geofizika, p. 101-108.

Kutzbach, J. E., Guetter P. J., Behling P. J., and Selin R., 1993, Simulated climatic changes; results of the COHMAP climate-model experiments, *in* Wright, H.E. Jr. et al., eds., Global climates since the last glacial maximum: Minneapolis, University of Minnesota Press, p. 24-93.

Lajoie, K. R., Kern, J. P., Wehmiller, J. F., Kennedy, G. L., Mathieson, S. A., Sarna-Wojcicki, A. M., Yerkes, R. F., and McCrory, P. F., 1979, Quaternary marine shorelines and crustal deformation, San Diego to Santa Barbara, California, *in* Abbott, P. L., ed., Geological Excursions in the Southern California Area: San Diego, San Diego State University, California, p. 3-15.

Lavé, J., and Avouac, J. P., 2000, Active folding of fluvial terraces across the Siwaliks Hills, Himalayas of central Nepal: Journal of Geophysical Research, v. 105, p. 5735-5770.

Le Fort, P., 1975, Himalayas: the collided range. Present knowledge of the continental arc.: American Journal of Science, v. 275-A, p. 1-44.

Little, T. A., Grapes, R., and Berger, G. W., 1998, Late Quaternary strike slip on the eastern part of the Awatere Fault, South Island, New Zealand: Geological Society of America Bulletin, v. 110, no. 2, p. 127-148.

Liu, H., McClay, K. R., and Powell, D., 1992, Physical models of thrust wedges, *in* McClay, K. R., ed., Thrust tectonics: London, United Kingdom, Chapman & Hall, p. 71-81.

Lozek, V., 1990, Molluscs in loess, their paleoecological significance and role in geochronology - principles and methods: Quaternary International, v. 7-8, p. 71-79.

Makarov, V. I., 1977, New tectonic structures of the Central Tien Shan (in Russian): Moscow, Order of the Red Banner Geology Institute, Akad. Sci., 171 p.

Martinod, J., and Davy, P., 1992, Periodic instabilities during compression or extension of the lithosphere 1. Deformation modes from an analytical perturbation method: Journal of Geophysical Research, v. 97, p. 1999-2014.

Martinod, J., and Davy, P., 1994, Periodic instabilities during compression or extension of the lithosphere, 2. Analog experiments: Journal of Geophysical Research, v. 99, p. 12057-12069.

Mattauer, M., 1975, Sur le mécanisme de formation de la schistocité dans l'Himalaya: Earth and Planetary Science Letters, v. 28, p. 144-154.

Mattauer, M., 1986, Intracontinental subduction, crust-mantle decollement and crustal-stacking wedge in the Himalayas and other collision belts, *in* Coward, M. P., and Ries, A. C., eds., Collision Tectonics: London, Geological Society of London, p. 37-50.

McCalpin, J. P., 1996, Application of Paleoseismic Data to Seismic Hazard Assessment and Neotectonic Research, *in* McCalpin, J. P., ed., Paleoseismology: San Diego, Academic Press, p. 439-493.

McGill, S. F., and Rubin, C. M., 1999, Surficial slip distribution on the central Emerson fault during the June 28, 1992, Landers earthquake, California: Journal of Geophysical Research, v. 104, p. 4811-4833.

Medvedev, S. V., 1976, Seismic zoning of the USSR / edited by S. V. Medvedev; translated from Russian [by Rita Teteruk-Schneider]: Jerusalem, Israel Program for Scientific Translations, p. 533.

Meghraoui, M., Philip, H., Albarede, F., and Cisternas, A., 1988, Trench investigations through the trace of the 1980 El Asnam thrust fault: evidence for paleoseismicity: Bulletin of the Seismological Society of America, v. 78, no. 2, p. 979-999.

Mellors, R. J., Vernon, F. L., Pavlis, G. L., Abers, G. A., Hamburger, M. W., Ghose, S., and Iliasov, B., 1997, The M (sub s) = 7.3 1992 Suusamyr, Kyrgyzstan, earthquake: 1. Constraints on fault geometry and source parameters based on aftershocks and body-wave modeling: Bulletin of the Seismological Society of America, v. 87, no. 1, p. 11-22.

Merritts, D. J., Vincent, K. R., and Wohl, E. E., 1994, Long river profiles, tectonism, and eustasy: A guide to interpreting fluvial terraces: Journal of Geophysical Research, v. 99, p. 14,031-14,050.

Molnar, P., 1988, Continental tectonics in the aftermath of plate tectonics: Nature, v. 335, p. 131-137.

Molnar, P., Brown, E. T., Burchfiel, B. C., Deng, Q., Feng, X., Li, J., Raisbeck, G. M., Shi, J., Wu, Z., Yiou, F., and You, H., 1994, Quaternary climate change and the formation of river terraces across growing anticlines on the north flank of the Tien Shan, China: Journal of Geology, v. 102, no. 5, p. 583-602.

Molnar, P., and Ghose, S., 2000, Seismic Moments of Major Earthquakes and the Rate of Shortening across the Tien Shan: Geophysical Research Letters, v. 27, no. 16, p. 2377-2380.

Molnar, P., and Lyon-Caen, H., 1988, Some simple physical aspects of the support, structure, and evolution of mountain belts, *in* Clark, S. P., Jr., Burchfiel, B. C., and Suppe, J., eds., Processes in continental lithospheric deformation.: Special Paper 218: Boulder, Geological Society of America, p. 179-207.

Molnar, P., and Tapponnier, P., 1975, Cenozoic tectonics of Asia; effects of a continental collision: Science, v. 189, p. 419-426.

Mugnier, J. L., Guellec, S., Menard, G., Roure, F., Tardy, M., and Viallon, P., 1990, A crustal scale balanced cross-section through the external Alps deduced from the ECORS profile, *in* Roure, F., Heitzmann, P., and Polino, R., eds., Deep structure of the Alps: Memoires de la Societe Geologique de France, Nouvelle Serie: Paris, Societe Geologique de France, p. 203-216.

Narr, W., and Suppe, J., 1994, Kinematics of basement-involved compressive structures: American Journal of Science, v. 294, no. 7, p. 802-860.

Nelson, K. D., and others, a., 1996, Partially molten middle crust beneath southern Tibet; synthesis of Project INDEPTH results.: Science, v. 274, p. 1684-1688.

Nelson, M. R., McCaffrey, R., and Molnar, P., 1987, Source parameters for 11 earthquakes in the Tien Shan, Central Asia, determined by P and SH waveform inversion: Journal of Geophysical Research, v. 92, p. 12,629-12,648.

Ni, J., 1978, Contemporary tectonics in the Tien Shan region: Earth and Planetary Science Letters, v. 41, no. 3, p. 347-354.

Ollerhead, J., Huntley, D. J., and Berger, G. W., 1994, Luminescence dating of the Buctouche Spit, New Brunswick: Canadian Journal of Earth Sciences, v. 31, p. 523-531.

Peixoto, J. P., and Oort, A. H., 1992, Physics of Climate: New York, American Institute of Physics, 520 p.

Peltzer, G., Tapponnier, P., and Armijo, R., 1989, Magnitude of late Quaternary left-lateral displacements along the north edge of Tibet: Science, v. 246, p. 1285-1289.

Pinter, N., Johns, B., Little, B., and Vestal, W. D., 2001, Fault-Related folding in California's Northern Channel Islands Documented by Rapid-Static GPS Positioning: GSA Today, v. 11, no. 5, p. 4-9.

Porter, S. C., and An, Z., 1995, Correlation between climate events in the North Atlantic and China during the last glaciation: Nature, v. 375, p. 305-308.

Porter, S. C., An, Z., and Zheng, H., 1992, Cyclic Quaternary Alluviation and Terracing in a Nonglaciated Drainage Basin on the North Flank of the Qinling Shan, Central China: Quaternary Research, v. 38, p. 157-169.

Prescott, J. R., and Hutton, J. T., 1988, Cosmic ray and gamma ray dosimetry for TL and ESR: Nuclear Tracks and Radiation Measurements, v. 14, p. 223-227.

Ramsey, C. B., 1998, Probability and dating: Radiocarbon, v. 40, no. 1, p. 461-474.

Rockwell, T. K., Keller, E. A., and Dembroff, G. R., 1988, Quaternary rate of folding of the Ventura Avenue Anticline, western Transverse Ranges, Southern California: Geological Society of America Bulletin, v. 100, no. 6, p. 850-858.

Rodgers, J., 1987, Chains of basement uplifts within cratons marginal to orogenic belts: American Journal of Science, v. 287, no. 7, p. 661-692.

Royden, L., 1996, Coupling and decoupling of crust and mantle in convergent orogens; implications for strain partitioning in the crust: Journal of Geophysical Research, v. 101, p. 17,679-17,705.

Royse, F. J., Warner, M. A., and Reese, D. L., 1975, Thrust belt structural geometry and related stratigraphic problems: Wyoming, Idaho, northern Utah, Symposium on Deep Drilling Frontiers in Central Rocky Mountains: Denver, Rocky Mountain Association of Geologists, p. 41-54.

Rubin, C. M., 1996, Systematic underestimation of earthquake magnitudes from large intracontinental reverse faults; historical ruptures break across segment boundaries: Geology, v. 24, no. 11, p. 989-992.

Rubin, C. M., Lindvall, S. C., and Rockwell, T. K., 1998, Evidence for Large Earthquakes in Metropolitan Los Angeles: Science, v. 281, p. 398-402.

Rubin, C. M., Scharer, K. M., Chen, J., Burbank, D., and Zhao, R., 2000, Late Cenozoic deformation along the western Kashi-Aksu thrust belt, southern Tien Shan, Xinjiang, China: Geological Society of America Annual Meeting, Abstracts with Programs, v. 32, no. 7.

Ruhe, R. V., 1959, Stone lines in soils: Soil Science, v. 87, p. 223-231.

Sadybakasov, I., 1972, Neotectonics of the central Tien Shan (in Russian): Frunze (Bishkek), Ilim, 117 p.

Sadybakasov, I., 1990, Neotectonics of High Asia (in Russian): Moscow, Nauka, 176 p.

Scharer, K., Burbank, D., Chen, J., Rubin, C. M., and Zhao, R., 2000, Quaternary folding of Cenozoic strata along the southwestern margin of the Tien Shan, China: Geological Society of America Annual Meeting, Abstracts with Programs, v. 32, no. 7.

Schulz, S. S., 1948, Analysis of the neotectonics and relief of the Tien Shan (in Russian): Moscow, Geografgiz, 222 p.

Schwartz, D. P., and Coppersmith, K. J., 1984, Fault behavior and characteristic earthquakes: examples from the Wasatch and San Andreas fault zones: Journal of Geophysical Research, v. 89, p. 5681-5698.

Severinghaus, J. P., and Brook, E. J., 1999, Abrupt Climate Change at the End of the Last Glacial Period Inferred from Trapped Air in Polar Ice: Science, v. 286, p. 930-934.

Shackleton, N. J., 2000, The 100,000-Year Ice-Age Cycle Identified and Found to Lag Temperature, Carbon Dioxide, and Orbital Eccentricity: Science, v. 289, p. 1897-1902.

Shirokova, Y. I., 1974, A detailed study of the stresses and faults at earthquake foci of Central Asia: Physics of the Solid Earth, v. 11, p. 707-717.

Sieh, K. E., and Jahns, R. H., 1984, Holocene activity of the San Andreas fault at Wallace Creek, California: Geological Society of America Bulletin, v. 95, p. 883-896.

Sobel, E. R., and Dumitru, T. A., 1997, Thrusting and exhumation around the margins of the western Tarim Basin during the India-Asia collision: Journal of Geophysical Research, v. 102, p. 5043-5063.

Stone, D. S., 1993, Basement-involved thrust-generated folds as seismically imaged in the subsurface of the central Rocky Mountain foreland, *in* Schmidt, C. J., Chase, R. B., and Erslev, E. A., eds., Laramide basement deformation in the Rocky Mountain foreland of the Western United States: Special Paper 280: Boulder, Geological Society of America, p. 271-318.

Stuiver, M., and Polach, H. A., 1977, Discussion; reporting of C-14 data: Radiocarbon, v. 19, no. 3, p. 355-363.

Stuiver, M., and Reimer, P. J., 1986, A computer program for radiocarbon age calibration: Radiocarbon, v. 28, p. 1022-1030.

Stuiver, M., and Reimer, P. J., 1993, Extended 14C database and revised CALIB radiocarbon calibration program: Radiocarbon, v. 35, p. 215-230.

Stuiver, M., Reimer, P. J., Bard, E., Beck, J. W., Burr, G. S., Hughen, K. A., Kromer, B., McCormac, G., van, d. P. J., and Spurk, M., 1998, INTCAL98 radiocarbon age calibration, 24,000-0 cal BP: Radiocarbon, v. 40, no. 3, p. 1041-1083.

Suppe, J., 1983, Geometry and kinematics of fault-bend folding: American Journal of Science, v. 283, no. 7, p. 684-721.

Suppe, J., Chou, G. T., and Hook, S. C., 1992, Rates of folding and faulting determined from growth strata, *in* McClay, K. R., ed., Thrust Tectonics: London, United Kingdom, Chapman & Hall, p. 105-121.

Suppe, J., and Medwedeff, D. A., 1990, Geometry and kinematics of fault-propagation folding: Eclogae Geologicae Helvetiae, v. 83, p. 409-454.

Suppe, J., Sabat, F., Munoz, J. A., Poblet, J., Roca, E., and Verges, J., 1997, Bed-by-bed fold growth by kink-band migration; Sant Llorenc de Morunys, eastern Pyrenees: Journal of Structural Geology, v. 19, p. 443-461.

Tapponnier, P., and Molnar, P., 1979, Active faulting and Cenozoic tectonics of the Tien Shan, Mongolia, and Baykal regions: Journal of Geophysical Research, v. 84, p. 3425-3459.

Tarasov, S. A., 1970, Cenozoic Geology and Neotectonics of the Tien Shan (in Russian): Frunze (Bishkek), Ilim, 211. p.

Trifonov, V. G., Makarov, V. I., and Skobelev, S. F., 1992, The Talas-Fergana active right-lateral fault: Annales Tectonicae, v. 6, p. 224-237.

Turbin, L. E., Sabduchev, S. S., Cherepanov, A. A., and Yanuchevich, U. D., 1966, Anthropogen (Quaternary Period) of Kyrgyz Tien Shan, Stratigraphy of Cenozoic and some questions of the newest tectonics of northern Kyrgyzstan (in Russian): Frunze, Ilim.

Ward, G. K., and Wilson, S. R., 1978, Procedures for comparing and combining radiocarbon age determinations: a critique: Archaeometry, v. 20, no. 1, p. 19-31.

Weberling, K. D., Beck, M., Weldon, R. J. I., Turner, H., and Thompson, S., 2000, The Naryn basin paleomagnetic section: a constraint on the onset of late Cenozoic deformation in the central Tien Shan, Kyrgyzstan: Geological Society of America Abstracts with Programs, v. 32, no. 7.

Weldon, R. J., 1986, Late Cenozoic geology of Cajon Pass: Implications for tectonics and sedimentation along the San Andreas fault [Ph.D. thesis]: California Institute of Technology, 400 p.

Weldon, R. J. I., and Sieh, K. E., 1985, Holocene rate of slip and tentative recurrence interval for large earthquakes on the San Andreas Fault, Cajon Pass, Southern California.: Geological Society of America Bulletin, v. 96, no. 6, p. 793-812.

Wells, D. L., and Coppersmith, K. J., 1994, New Empirical Relationships among Magnitude, Rupture Length, Rupture Width, Rupture Area, and Surface Displacement: Bulletin of the Seismological Society of America, v. 84, no. 4, p. 974-1002.

Wesnousky, S. G., 1994, The Gutenberg-Richter or Characteristic Earthquake Distribution, Which is it?: Bulletin of the Seismological Society of America, v. 84, no. 6, p. 1940-1959.

Willett, S., Beaumont, C., and Fullsack, P., 1993, Mechanical model for the tectonics of doubly vergent compressional orogens: Geology, v. 21, no. 4, p. 371-374.

Willett, S. D., 1999, Rheological dependence of extension in wedge models of convergent orogens: Tectonophysics, v. 305, no. 4, p. 419-435.

Yeats, R. S., and Lillie, R. J., 1991, Contemporary tectonics of the Himalayan frontal fault system; folds, blind thrusts and the 1905 Kangra earthquake: Journal of Structural Geology, v. 13, p. 215-225.

Yin, A., Nie, S., Craig, P., Harrison, T. M., Ryerson, F. J., Qian, X., and Yang, G., 1998, Late Cenozoic tectonic evolution of the southern Chinese Tien Shan: Tectonics, v. 17, p. 1-27.

Zhou, W. H., M.J.; Wang, Fubao; Donahue, D.J.; Jull, A.J.T., 1999, The reliability of AMS radiocarbon dating of shells from China.: Radiocarbon, v. 41, no. 1, p. 17-24.

Zonenshain, L. P., and Savostin, L. A., 1979, Introduction in geodynamics (in Russian): Moscow, Nedra, 312 p.

Vita

Stephen C. Thompson

- 1992 A.B. Dartmouth College, Hanover, NH
- 1996 M.S. University of Washington, Seattle, WA
- 2001 Ph.D. University of Washington, Seattle, WA